UNIVERSITY OF SOUTHAMPTON

FACULTY OF PHYSICAL SCIENCES AND ENGINEERING
School of Physics and Astronomy

Schottky Enhanced Photo-Dember Terahertz Emitters

by

Paul C. Gow

Thesis for the degree of Doctor of Philosophy

July 2016

UNIVERSITY OF SOUTHAMPTON

ABSTRACT

FACULTY OF PHYSICAL SCIENCES AND ENGINEERING
School of Physics and Astronomy

Doctor of Philosophy

SCHOTTKY ENHANCED PHOTO-DEMBER TERAHERTZ EMITTERS

by Paul C. Gow

The unique properties of terahertz (THz) radiation make it useful for application in the field of imaging. The use of THz time-domain spectroscopy (THz-TDS) systems for the identification and characterisation of various materials is becoming more widespread, with this technology being applied in industry, security and scientific research. The common method for generating THz in commercial TDS systems is through the use of photoconductive antennas (PCA's). These are semiconductor-based devices capable of generating several μW of power. PCA's require an external bias to generate a strong electric field across a small electrode gap. However, the high fields generated cause electromigration of the electrode metals and can result in damage to the antenna.

This thesis investigates the lateral photo-Dember (LPD) effect; a method of generating THz radiation from a semiconductor without the need for an applied electrical bias. The LPD effect relies on the difference in mobilities between electrons and holes to create opposing dipoles parallel to the semiconductor surface. The selective suppression of dipoles formed underneath a metal mask due to reflection then introduces the asymmetry required for observable THz radiation.

In this thesis the generation mechanism behind the LPD effect is investigated using 1D and 2D models, as well as the effect of the presence of a metal mask to suppress dipoles. The output from LPD emitters is enhanced through multiplexing and two different designs are investigated and fully characterised. The novel double-metal multiplexed emitters are then used to demonstrate THz beam shaping and focusing through control of the optical pump beam and a lensless THz-TDS system is proposed.

Contents

List of Figures

List of Tables

Declaration of Authorship

I, Paul C. Gow, declare that the thesis entitled *Schottky Enhanced Photo-Dember Terahertz Emitters* and the work presented in the thesis are both my own, and have been generated by me as the result of my own original research. I confirm that:

- this work was done wholly or mainly while in candidature for a research degree at this University;
- where any part of this thesis has previously been submitted for a degree or any other qualification at this University or any other institution, this has been clearly stated;
- where I have consulted the published work of others, this is always clearly attributed;
- where I have quoted from the work of others, the source is always given. With the exception of such quotations, this thesis is entirely my own work;
- I have acknowledged all main sources of help;
- where the thesis is based on work done by myself jointly with others, I have made clear exactly what was done by others and what I have contributed myself;
- parts of this work have been published as: Appendix A

Signed:..

Date:...

Acknowledgements

Firstly, I would like to thank my supervisor Dr. Vasilis Apostolopoulos for all his help, guidance, support and advice throughout my PhD and beyond. I would also like to thank Prof. Anne Tropper, Dr. Keith Wilcox and Dr. Adrian Quarterman for their help and encouragement during my undergraduate summer project, as it was this that convinced me to do a PhD. I also want to thank my A-level physics teachers, Paul Evans and Kimi Berkeley, who convinced me to stick at physics after my GCSE's.

I would like to thank Dr. Mark Barnes and Dr. Duncan McBryde who welcomed me to the THz group, showed me the ropes and became good friends. I want to thank Dr. Sam Berry for his help and guidance at the start of my PhD, as well as various sing-a-longs in the lab and car journeys to our collaborators in Cambridge. I also would like to thank the other members of the THz group; Armen Aghajani, Geoff Daniell, Joanna Carthy, Lewis Maple and Elena Mavrona, for many talks, jokes, shared experiments and experiences (Shakespeares!). Many thanks also go to; Joe Spencer, Chris Baker, Olly Morris, Isaac Jones, Andrew Turnbull, Alex Jantzen, Matt Proctor, Theo Chen Sverre, Robin Head, Jamie Vovrosh and many, many more. The plethora of chats, coffees, nights out, advice, sports and laughs we have shared are much appreciated and have helped keep me sane for the last few years! I also want to thank all of the people I have worked with in demonstrating and outreach, as well as the QLM summer school, as these were a welcome retreat from my PhD and some fantastic experiences. All the people I have encountered during my university life I now count as good friends.

Of course I would like to thank my family, especially my Mum, Nan, Grandad and Auntie Sue for their support throughout my education and PhD, even though they have no idea what I've been doing! Finally – and most importantly – I would like to thank my amazing wife, Carly Gow, for her unwavering love and support in everything I do.

Life isn't about waiting for the storm to pass...
...it's about learning to dance in the rain.

Vivian Greene

Chapter 1

Introduction

The motivation for the work presented here is to study the mechanism of generating high signal-to-noise (SNR), single cycle, broadband terahertz (THz) emission from superposition of multiple THz wavefronts generated in a partially masked semiconductor. In this thesis the generation mechanism is explored theoretically through computation. Modelling shows superposition of multiple wavefronts to provide enhanced emission. Multiplex emitters based on my simulations are fabricated and characterised. These devices are developed further to enhance their THz output and improve alignment parameters, and are fully characterised and shown to be comparable to commercial emitters in both bandwidth and SNR whilst being more durable and easier to fabricate. Devices fabricated on graphene monolayers are tested and compared to semiconductor based emitters. Finally the possibility of beam steering with these devices has been characterised by THz wavefront manipulation through control of the optical pump beam. Circular emitter structures designed to produce radial THz polarisation profiles were also explored.

In this chapter I give a brief discussion of THz science and technology and its applications. I explore the different methods for the generation and detection of THz radiation, with detailed focus given to the THz time-domain spectrometer (THz-TDS), its function and uses. This chapter also contains a history and explanation of the lateral photo-Dember (LPD) mechanism for the generation of THz, the primary mechanism used for all of the work presented here, and the contributions of my research group to discover the underlying mechanism behind this effect. Finally, I outline the contents of this thesis.

1.1 The terahertz gap

The THz gap refers to a region of the electromagnetic spectrum which is sandwiched between the far-infrared and microwaves (figure 1.1). It gains its title from the frequencies

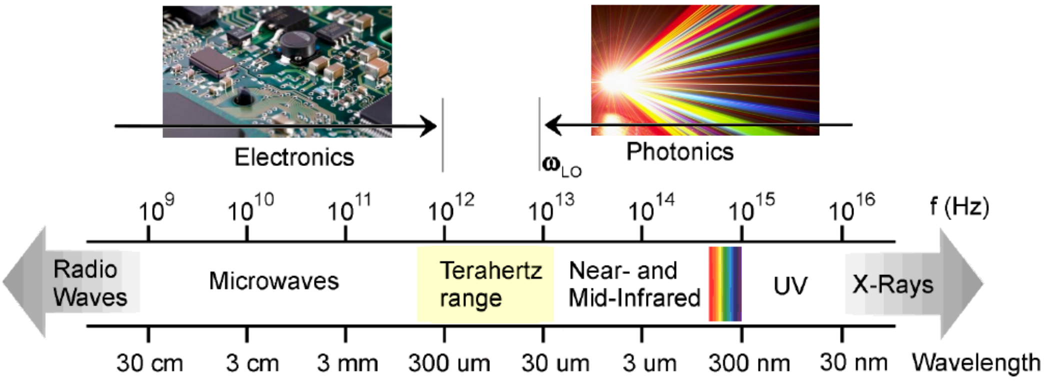

Figure 1.1: diagram showing the location of the THz region in the electromagnetic spectrum.

that it spans (typically 0.1 to 30 THz) and the fact that, for many years, it remained largely unexplored. The THz spectrum encompasses wavelengths from 30 µm to 3 mm and energies in the range of 40 meV to 0.4 meV. Any thermal source emits incoherent THz radiation. Insight into the formation and decay of stars can be gained through studying THz emission from interstellar dust, the origin of most of the THz radiation in the universe [1]. Before the 1970's THz radiation proved a largely inaccessible region bridging the gap between electronic and photonic technologies. Conventional electonic oscillator devices could not function efficiently above ∼300 GHz as the devices become unresponsive due to transistor performance above the cutoff frequency [2]. Semiconductor based optical devices also struggle to function efficiently as the energy band gap for THz is small (below 10 meV) compared to the phonon energy of the lattice, and electronic transitions at room temperature cannot be defined [3]. The difficulties in reaching this region of the EM spectrum led scientists to coin the term 'Terahertz Gap'.

Though difficult to access, the THz region holds a great deal of interest for scientific research and other practical applications. The vibrational and rotational modes of many atoms exist within this region and many chemical species have strong, unique absorption lines [4]. This is most evident in gasses – for example water vapour and carbon monoxide – which have narrow absorption lines in the far-infrared. As many carrier dynamics occur over picosecond time frames, THz radiation can be used to study the movement of charges within devices [5]. In recent decades many THz generation techniques have been explored and developed, increasing our understanding and use of these frequencies and gradually bridging the THz gap between optics and electronics.

1.2 History

Before the invention of ultrafast optical lasers broadband THz was primarily generated through thermal sources. These sources produce THz radiation as part of their black

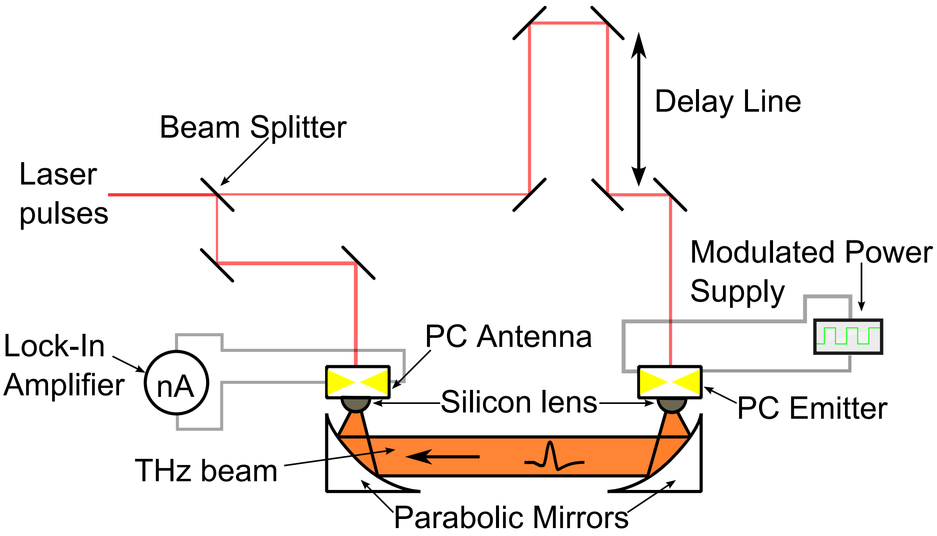

Figure 1.2: THz-TDS setup incorporating PC antennas for both emitter and detector. A femtosecond laser beam is split into pump and probe beams. The pump beam travels via an optical delay line before exciting THz radiation in the emitter. In this example the emitter is electrically modulated by an external power supply. The THz field is collimated by a parabolic mirror before being focussed onto the detector by a second parabolic mirror. The probe beam excites carriers within the detector which are accelerated by the instantaneous THz field. The current generated by this is detected by a lock-in amplifier.

body spectrum, however, this emission is incoherent and suffers from a low signal-to-noise ratio (SNR) [6]. Other sources used for accessing the far-infrared spectrum included gyrotrons, klystrons and synchrotrons, which were capable of producing megawatts of power up to 300 GHz [7]. The use of molecular vapour lasers allowed access to coherent THz sources [8]. Detection was limited to devices such as bolometers and Golay cells, which are still used for the detection of CW THz. Fourier transform spectrometers were also used, however they were found to function best for frequencies above 5 THz [9].

With developments in nonlinear optics and semiconductors in the 1960's due to the invention of the laser, new fields of photonics and optoelectronics were born. Shorter optical pulses were created by investigating new mode-locking mechanisms, and the modelocked Nd:glass laser was invented. It was this laser that was used by Auston [10] and Lee [11] in the mid 1970's for optically pumping photoconductive switches on Si and semi-insulating gallium arsenide (SI-GaAs). Around the same time two other groups were conducting research towards generating far-infrared pulses from nonlinear crystals [12, 13]. As laser pulses grew shorter photoconductive switches could be activated faster, leading to the generation of 1.6 ps THz pulses by Auston *et al.*, in 1984 [14]. The pulses generated were then detected by another photoconductive 'Auston' switch on the opposite side of a dielectric slab, thus giving birth to modern THz science. In the same year Auston investigated nonlinear rectification for generating THz [14] and soon after demonstrated its use for spectroscopy [15].

During the late 1980's and early 1990's many advances in the field of THz science were made. DeFonzo demonstrated single cycle THz pulses propagating through air before detection [16]. Shortly afterwards van Exter *et al.* demonstrated a system for pump-probe spectroscopy which would become the typical standard for THz spectrometer design [17]. The system, based on a synchronous emission and detection scheme, was similar to that shown in figure 1.2. The pulses from an ultrafast laser were split into a pump and probe beam. The pump beam was focussed between two electrodes separated by 5 µm fabricated on the surface of a semiconductor, acting as an 'emitter'. An applied bias was used to accelerate the carriers generated by the pump pulse, creating a dipole parallel to the material surface which radiates on a picosecond time scale [18]. The THz pulse generated is focussed by a sapphire lens onto a collimating parabolic mirror. The pulse is then focussed onto a second, unbiased 'detector' antenna by another parabolic mirror and sapphire lens. The probe pulse from the laser is directed onto the 'detector' antenna in the same manner as the pump pulse is aligned onto the 'emitter' antenna. The carriers produced by the probe pulse are accelerated by the THz field present at that moment. As the laser pulses and carrier lifetimes are much shorter than the THz pulse the carriers in the detector antenna see the THz as a DC field. By measuring the current produced in the detector antenna it is possible to deduce the strength of the THz field at that time. Delaying the optical pulse which excites the THz pulse by way of a mechanical delay line allows the THz field variation with time to be measured. Electrically gating the emitter allows for a lock-in amplifier to be used to enable detection of these small signals. Later that year van Exter *et al.* used pulsed THz from photoconductive switches to perform time-domain spectroscopy on water vapour and measure its spectrum [17]. The MBE growth of low temperature gallium arsenide (LT-GaAs) led to the improvement of photoconductive switches, with large mobilities for fast carrier lifetimes tailored by the growth process. The invention of the self modelocked Ti:sapphire laser in 1991 [19] (which could produce pulses below 100 fs) helped the spread of THz research. Research continued towards increasing the detectable bandwidth range, with Wu *et al.* demonstrating detection with a flat frequency response over an ultrawide bandwidth with nonlinear crystals [20].

In the succeeding years THz science and technology has developed and matured. The work accomplished in these early years led to the development of the terahertz time-domain spectrometer, a system still commonly used for research and commercial purposes. These systems offer a high SNR and, as the electric field of the THz pulse is directly measured, can also provide phase information which gives THz-TDS a major advantage for spectroscopy. Today THz technology is employed in a wide and varied range of fields.

1.3 Applications

The unique properties of THz allow it to find uses in applications ranging from security and spectroscopy, to art conservation and research [21]. At these wavelengths many materials such as ceramics, plastics and clothing exhibit low absorption, allowing THz technology to be used for security and quality control. With many materials exhibiting a unique THz absorption spectrum, integrating this technology with time-domain spectroscopy (TDS) has provided an accurate detection method for illicit materials as well as a useful tool for scientific research. The THz spectrum spans energies in the region of 1 to 100 meV, meaning that THz radiation negates the ionisation risks that more energetic rays pose. Coupled with high absorption by water and the fact that these energies are close to the vibrational modes of organic molecules, THz finds applications within biological, medical and pharmaceutical sciences.

1.3.1 Medical applications

There is a vast amount of existing imaging techniques in medicine, including; magnetic resonance imaging (MRI), optical tomography and X-ray imaging. However, many of these systems have shortcomings such as running costs, resolution limitations or safety issues. The non-ionising properties of THz radiation mean that it is safe and can be used for a multitude of biological applications [22]. Though THz is strongly absorbed by water it can penetrate up to several millimeters of biological tissue if there is low water content or little fat tissue present. THz imaging has been used for the *in–vivo* study of human skin tissue, obtaining tomographic information and mapping the hydration content of the samples [23]. Reflection scans of human skin have shown it is possible to differentiate between scar tissue, healthy and diseased skin, allowing detection of the spread of skin cancers [24]. The use of THz in 3D dental imaging has also been studied [25]. This allows the measurement of enamel thickness on teeth and the identification of subsurface features. This method is non-destructive and negates the need for invasive drilling or the health risks associated with dental X-rays.

Many chemical and organic species also have intermolecular vibrations within the THz range which can be observed [26]. THz spectroscopy can also identify different chemicals and polymorphic structures – different crystalline structures of the same chemical – which can have very different physical and chemical properties. Classification of these polymorphs is important for health and pharmaceuticals. Most techniques involve X-ray diffraction or Raman spectroscopy for measurements. These processes usually require large crystalline structures or can, in the case of Raman spectroscopy, induce phase changes during the measurement. As THz is non-destructive and does not induce phase changes it is a valuable tool, and has developed for the analysis of pharmaceutical tablets. On the surface the quality and thickness of pill coatings can be monitored [27], not only for quality control purposes, but for tailoring the dissolution of the pills surface for drug delivery [28]. THz systems are also able to generate 3D images and gather spectroscopic information for the identification of chemical structures.

1.3.2 Security

Materials such as paper, plastic, ceramics and clothing exhibit low absorption to THz, making it ideal for security applications. THz radiation can be safely used in airports and public spaces for scanning due to its non-ionising nature. There are now mm-wave full body scanners installed in some airports for detecting weapons and illicit materials, but these devices have raised concerns about privacy [29]. The unique absorption spectra attained from different materials through THz spectroscopy allow for the identification of many compounds which may appear similar at visible frequencies. This technology is now used for the detection and identification of drugs and explosives for matters of security. Companies such as Fraunhofer IPM have released THz products which can scan mail to identify the contents of a package or envelope without opening to determine if it is safe [30].

1.3.3 Quality control

The transparency of certain materials at THz frequencies have also allowed applications in non-destructive testing and quality control. These technologies have been employed in industry to monitor production processes from pipe extrusion to the quality of coatings on medicines. THz imaging has been used to inspect the foam insulation used on space shuttles for defects and is now part of the routine checks carried out [31]. Probing carrier dynamics with THz has proved useful for inspecting devices such as solar cells, nanomaterials and films, as well as determining the doping levels of various semiconductors [32–35]. With the production of large scale graphene sheets, THz is proving a useful tool for exploring carrier properties such as mobility, density and scattering time in CVD grown graphene, as well as finding the DC sheet conductance [36]. THz is exceptionally good at characterising multiple thin films and has been demonstrated as a useful tool for the quality control of thickness and drying in paint deposition [37].

1.3.4 Information and communication technologies

Current wireless technologies tend to operate in the region of 2.5 to 5.9 GHz. To cope with the growing data requirements of the 21^{st} century driven by the smartphone market, technology must keep pace [38]. The high carrier frequencies of the THz range make it an ideal candidate for supporting telecommunication growth in the future as it would allow for faster data transfer rates. The major hurdle to overcome is the high absorption of THz by water. The combination of using powerful THz sources to combat losses caused by water vapour in the air and operating away from the absorption lines could provide efficient and reliable wireless data transfer. Recent developments have demonstrating wireless data communication at a rate of 100 Gbit s^{-1} over a range of 20 m [39]. Fibre linked wireless systems have achieved speeds above 400 Gbits s^{-1} with world record setting bandwidths [40].

1.3.5 Other applications

THz has proved a useful tool for studying the cosmos, as most thermal sources emit in this region as part of their black body radiation. Results from the NASA Cosmic Background Explorer (COBE) Diffuse Infrared Background Experiment (DIRBE) indicated that 98% of photons emitted since the Big Bang fall into the submillimeter and THz region of the EM spectrum [41]. Further astronomical study has used the detection of cosmic THz radiation to investigate interstellar dust as well as the atmospheres of planets and small-bodies such as asteroids, moons and comets [6].

The scope for application of THz technology in medicine, security and quality control is vast. However, standard spectroscopy setups have limitations in their functionality for everyday use. In 1995 Hu *et al.* demonstrated the first THz imaging system [42] where full spectral information for each image pixel is possible. Over the last two decades advances have been made in developing stand-off THz cameras for non-invasive, short range imaging. Many of these devices involved the use of a quantum cascade laser (QCL) as the THz source to provide high power emission and a detector such as a bolometer to read the signal [30]. Current systems are capable of producing real-time, 3D images [43] and have been developed to a point where they are compatible with modern CMOS based detectors [44].

In the art world THz can be a useful tool during the process of restoration. Over time paintings must be restored and preserved to prevent their deterioration. During this process it is important to make an analysis of the original materials and techniques used in the painting to retain the authenticity and any previous restoration work must be identified. Many tools such as X-ray fluorescence, IR spectroscopy and photographic examinations have been used to study paintings but either prove to be limited in detail or potentially damaging [45]. THz radiation has been demonstrated as a non-destructive method [46], able to reveal details about the paint layers, materials and can even be used for tomography of the painting through raster scannning. As canvas was expensive artists would often paint over previous or unfinished work to save money. Hidden paintings can be revealed by THz scanning techniques, as well as damage and forgeries [47].

1.4 Generating terahertz

There are now many methods for generating radiation within the THz region. Some of the more common and widely used methods of THz generation are explored in this section, with a strong focus on sources for use in THz-TDS. Typically such sources emit below the background level present due to thermal sources, however synchronous detection allows for high SNR in spectroscopic applications.

1.4.1 Photoconductive antenna

The most common THz generation technique for TDS comes by way of the photoconductive antenna (PCA) [48–50], a type of Auston switch [14]. These antennas typically consist of a grown semiconductor material with metallic electrodes separated by a few microns deposited on the surface, illustrated in figure 1.3. To generate THz emission a potential difference is applied to the electrodes to establish a strong electric field across the antenna gap. An ultrafast laser is used to excite carriers within this gap, which are then accelerated by the applied electric field. The carriers are quickly recaptured by defect trap sites and through recombination. This process of generation, acceleration and recombination of charge carriers occurs over the time range of a few picoseconds, leading to the emission of broadband THz radiation spanning the range of 100 GHz to 3–4 THz. The semiconductor substrate and the laser used are codependent, as the photon energy of the laser must be above the band gap of the semiconductor to sufficiently generate carriers. Most commonly gallium arsenide (GaAs) substrates are used alongside a Ti:sapphire laser operating around 800 nm wavelength, though sometimes InAs based substrates are used in conjunction with 1.5 µm laser systems as this material has a lower energy band gap [51]. There has been a great deal of research dedicated towards creating the most efficient electrode design, including dipole, bow-tie

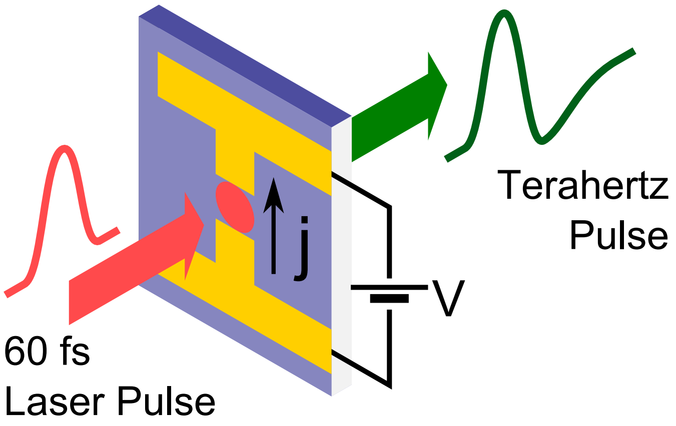

Figure 1.3: Photoconductive antenna. The incident laser pulse excites carriers which are accelerated by the potential V. The resulting charge separation causes dipole emission of THz frequencies.

and strip line designs [18]. Some recent designs to emerge have involved interdigitated arrays capable of producing high power THz radiation [52, 53], as well as electrodes enhanced by plasmonic structures [54]. Signal-to-noise ratio (SNR) is a measure of the ratio between the power of the signal being measured and that of the background noise. Due to the high SNRs achievable, this technology has seen much transfer from research to the real world, with companies such as Teraview, Gigaoptics and Menlo developing and manufacturing commercial PCAs and using them in their systems. These antennas are commonly used in systems such as THz-TDS due their generation of synchronous THz pulses and ability to be used as emitters or receivers.

1.4.2 Quantum cascade lasers

Since its introduction in 1994 [55] the Quantum Cascade Laser (QCL) has seen many advances in waveguide design and lattice structure, allowing higher operation powers and temperatures especially in the THz range [56]. A QCL is a semiconductor super-lattice structure consisting of repeating periods of coupled quantum wells (QWs) which are grown, or deposited, on the surface of a semiconductor substrate. Unlike conventional semiconductor lasers, QCLs typically do not involve a transition of electrons from conduction band to valence band. Instead they rely on intersubband transitions; transitions between quantised energy states within one energy band. This means that emission can be easily tailored by controlling the width of the QWs. Instead of electrons being pumped into a higher state in order to decay, electrons propagate down a ‘potential staircase’. An example of this staircase gain structure can be viewed in figure 1.4. The electron transitions from the upper radiative state (3) to the lower radiative state (2), emitting a photon. It then quickly transitions to the upper, ‘collector’ miniband state (1) before undergoing intra-miniband scattering, allowing the electron to relax to the bottom of the minibands making it readily available for injection into the next active region. With transition lifetime $\tau_{32} > \tau_{21}$, this creates the population inversion necessary for lasing. As a result of this method of transport, the gain recovery time relies heavily on the transport delay between active regions as electrons transition through the injector regions [57]. This has no analogue with conventional semiconductor lasers. Coupled with other effects, such as tunneling and phonon assisted scattering, the gain recovery time is incredibly fast and of the order of a few picoseconds. This is typically an order of magnitude less than the cavity round-trip time [58].

Another important aspect of QCL design is the waveguide. The semi-insulating surface plasmon (SI-SP) waveguide design involves the growth of a thin, heavily doped layer between the active region and the semi-insulating substrate. This results in a surface Plasmon mode which is bound to the top contact and the lower n$^+$ layer. The mode does extend into the substrate, but free carrier loss is minimal due to the small overlap with the doped region. In order to almost completely confine the mode, a metal layer can be

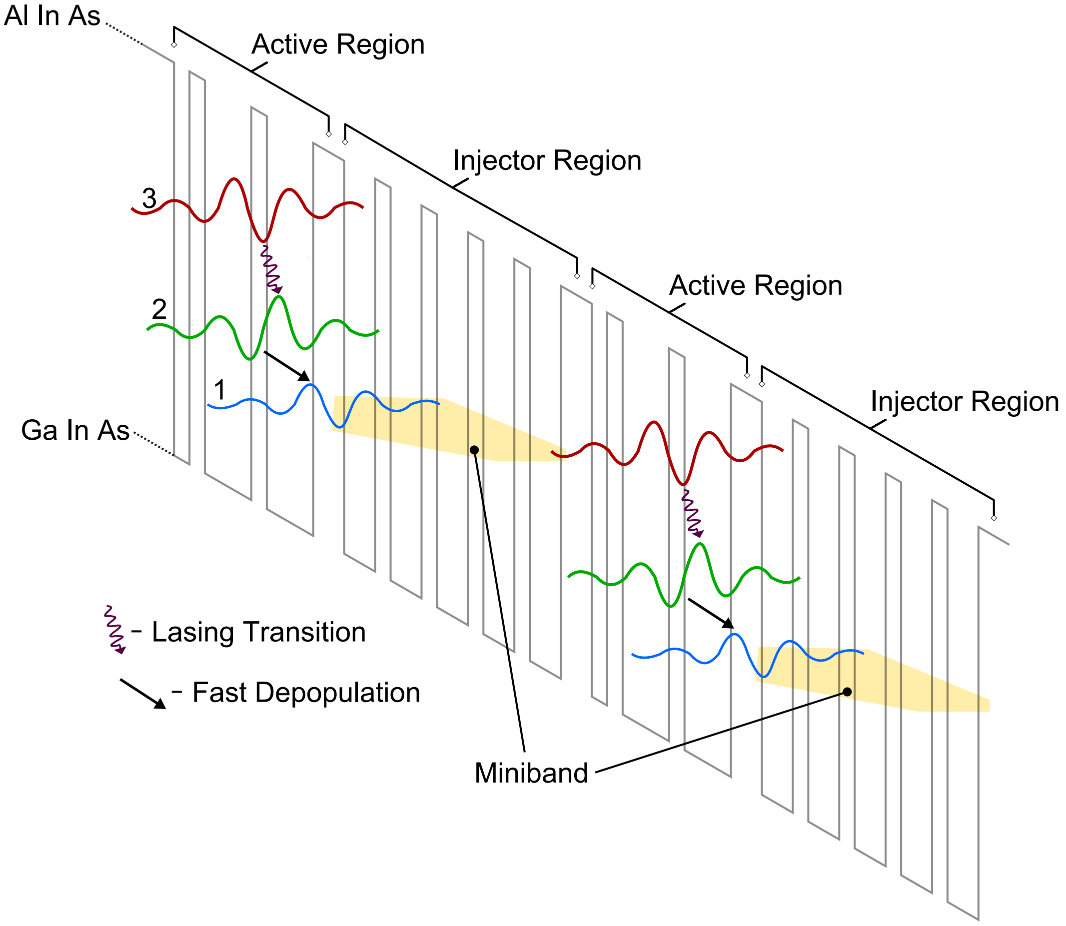

Figure 1.4: An example of the staircase band structure of a QCL with a potential applied to it. Transition 3→2 is the optical transition. Transition 2→1 is the fast depopulation to the miniband in order to create population inversion.

placed directly below the active region. This forms the metal-metal (MM) waveguide where strong mode confinement can allow for smaller dimensions, reducing the size of the structure to sub-wavelength proportions. The MM waveguide QCLs also exhibit higher operating temperatures than SI-SP designs [59]. However, these devices suffer from impedance matching between the waveguide modes and free propagating modes, leading to enhanced facet reflectivities and smaller threshold current densities. As such, MM QCLs show fairly low output powers (a few mW compared to a few 100 mW) and poor beam patterns with the output beam diffracting almost omnidirectionally from the facet, though techniques such as plasmonic structures [60] and coupling into waveguides [61] have sought to eliminate this problem. QCLs exhibit high output powers in the THz region, with recent endeavours leading to powers of over 1 W [62]. These sources are typically CW or have very high repetition rates. Time-domain spectroscopy (TDS) requires synchronous THz sources and current research has leaned towards using QCLs as amplifiers for photoconductive sources to achieve this [63, 64].

1.4.3 Optical rectification

The optical rectification of a sub-picosecond laser pulse by a nonlinear crystal is another popular choice for THz emission. Yang *et al.*, first observed far-infrared radiation from $LiNbO_3$ which was generated by picosecond pulses from an Nd:glass laser [13]. THz generation in electro-optic materials when excited by femtosecond optical pulses allowed the use of Ti:sapphire lasers and could produce large amplitude, coherent emission [65]. Optical rectification is analagous to electrical rectification, where an AC current is converted to a DC bias, and stems from the materials second order susceptibility $\chi^{(2)}$. For nonlinear crystals to produce observable THz emission their crystal orientation and length must be taken into account. Due to refractive index differences the generated THz and the optical pulse will experience a group-phase velocity mismatch and seperate spatially as they propagate through the crystal. Certain crystal lengths must be used to prevent destructive interference of the THz. Due to this thin crystals allow for larger bandwidths than thicker crystals, though have a lower output power. Optical rectification has also been observed in metals, where ultrathin percolated Au films on glass produced enhanced THz emission [66]. The pulsed nature of the THz emitted from these devices coupled with a bandwidth often larger than that from PC antennas makes these ideal for synchronous and frequency sensitive applications such as spectroscopy.

1.4.4 Difference frequency generation

CW or pulsed THz emission can be generated through the photomixing of optical sources. CW-THz was first reported by Brown *et al.* who used a photoconductive emitter illuminated by two CW, frequency offset lasers [67, 68]. This technique, coined as ‘optical heterodyne’, offers the advantage of wide tunability determined by the difference frequencies of the two lasers used. It is even possible to cause photomixing with dual and multimode lasers [69]. The priciple behind this method relies on the interaction of two optical sources operating at different frequencies to create a beat frequency of intensity. If the resulting optical beat is incident on a material that can respond to the average optical intensity then emission at this difference frequency will be observed. By controlling the frequency separation of the sources the beat frequency can be tuned to the THz range. Recent work in developing a bimodal semiconductor laser for pumping has allowed CW-THz emission from a plasmonic photoconductive antenna to be tuned from 0.15 to 3 THz [70]. Difference frequency generation has been applied within QCLs for THz generation, where the laser was engineered to support two wavelengths and difference frequency generation was performed intracavity [71]. The disadvantage to this technique is the low conversion efficiency of the pump laser powers to THz power. Pulsed emission from this technique allows for synchronous detection and spectroscopy applications, whereas the CW emission can be used for imaging.

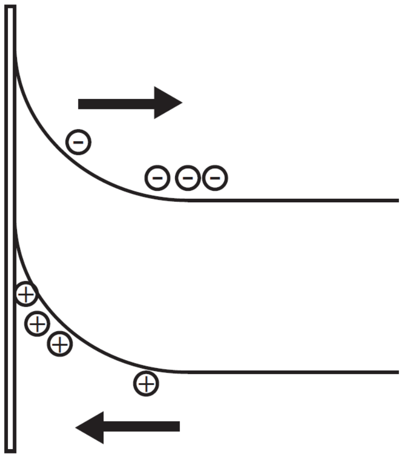

Figure 1.5: An example of the band bending which occurs near the surface of a semiconductor. Photogenerated carriers are accelerated within the depletion region by the built in electric field.

1.4.5 Surface emitters

Broadband THz pulses can be generated from semiconductors after ultrafast excitation of carriers close to the surface. The carriers produce surge currents on the timescale of picoseconds. There are primarily two different mechanisms responsible for suface emission, surface field emission and the photo-Dember effect [72, 73]. The first, surface field emission, is where carriers are accelerated by a surface field created through band bending (figure 1.5). In a semiconductor the electrostatic potential is homogeneous throughout but changes near to the surface. Impurities formed during growth can allow surface charges to form, and a depletion region is created within the semiconductor to neutralise the surface charge. This space-charge region causes a band bending effect near to the semiconductor surface resulting in an intrinsic electric field. When carriers are generated in this region after photo-excitation they are accelerated by the intrinsic field. The ultrafast surge current generated by the formation, acceleration and recombination of photo-excited carriers perpendicular to the material surface generates THz emission. The polarity of the emitted THz can be controlled by changing the doping of the semiconductor, and therefore the direction of the surface field [74].

For excitation photon energies which exceed the material bandgap the photo-Dember (PD) effect dominates over surface field effects [75, 76]. The PD effect is the emission of radiation resulting from the diffusion of carriers within a semiconductor without the need for an external bias [77–79]. When the semiconductor is illuminated with electromagnetic radiation of energy above that of the band gap, carriers are excited beneath the surface and then diffuse into the material. In materials such as GaAs the diffusion coefficient of the electrons is typically in the range of an order of magnitude larger than that of the holes so that they diffuse faster, creating a charge separation [80]. The electrons cannot diffuse past the semiconductor surface, thus the charge separation formed is

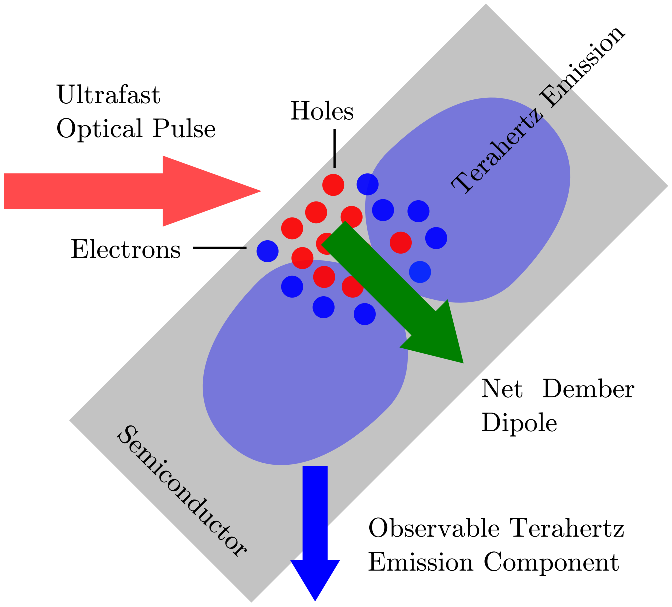

Figure 1.6: Diagram of THz generation from the photo-Dember effect. An ultrafast laser pulse generates carriers near the semiconductor surface. Electrons diffuse into the material faster than holes due to their higher mobility, creating a dipole perpendicular to the material surface (shown as a green arrow). The transient dipole radiates at 90° to its direction creating observable THz at 45° to the semiconductor surface.

asymmetrical and produces a dipole perpendicular to the material surface (figure 1.6). The time scale of the radiation is determined by material properties, such as the electron and hole recapture lifetimes and recombination lifetime. For GaAs and similar substrates this is in the region of a few ps, thus producing THz frequency radiation [81]. Doping concentration and screening effects also play a role in the strength of THz emission observed [82]. THz generated by surface effects are limited in power in relation to that of a PC antenna. Another issue is that surface effects generate dipole emission parallel to the semiconductor surface which can pose outcoupling problems. This can be partially addressed by positioning the semiconductor surface normal at an angle with the incident beam, allowing some emission parallel to the direction of the beam [50, 83]. This emission can also be enhanced by rotating the dipole with external magnetic fields, though the magnetic field required to do so exceeds several Tesla and so can prove impractical in most situations [72]. The THz pulses produced by these emitters can be used with synchronous detection schemes, however it is also possible to produce CW THz from these devices using photomixing.

1.4.6 Other techniques

There are other exotic techniques for generating THz, including emission from gold nanospheres [84], ferromagnetic films [85], nanorod arrays [86] and emission through ambient air-plasma generation [6, 38].

1.5 Detecting terahertz

1.5.1 Photoconductive antenna

As well as providing emission, PCAs can also be used for synchronous detection of THz radiation in TDS. Detection works on the reverse principle of the emission mechanism except without an applied electrical bias [87]. Upon illumination from an ultrafast pulse, carriers are generated within the material. If a THz field is incident on the material then it can accelerate the photo-generated carriers. As the laser pulse and carrier lifetime are much shorter than the length of the THz pulse the carriers see the THz field as a DC electric field. The current generated by the movement of the carriers is directly proportional to the THz field and can be measured across the antenna gap. By varying the delay between the THz and optical pulses the variation of the THz field can be mapped out in time. The resulting pulse is the convolution of the THz electric field and the time dependent conductivity of the PCA detector.

1.5.2 Electo-optic detection

THz can also be detected through the use of nonlinear crystals. Detection is based on the linear electro-optic, or 'Pockels' effect. This is where an external DC electric field induces a birefringence in a crystal. Figure 1.7 shows an example of an electro-optic detection scheme for THz. When THz radiation is incident on a nonlinear crystal it induces a birefringence which varies linearly with electric field. If a probe laser pulse propagates colinearly with the THz in the crystal then the induced birefringence can change the polarisation state of the probe pulse. Propagating the probe pulse through a quarter wave plate and polarising beam splitter before directing it onto a pair of balanced photodiodes allows the change in polarisation to be measured. The polarisation change is related directly to the change in birefringence, which is related linearly to the THz field. Due to the length of the THz pulse in comparison to the optical probe pulse,

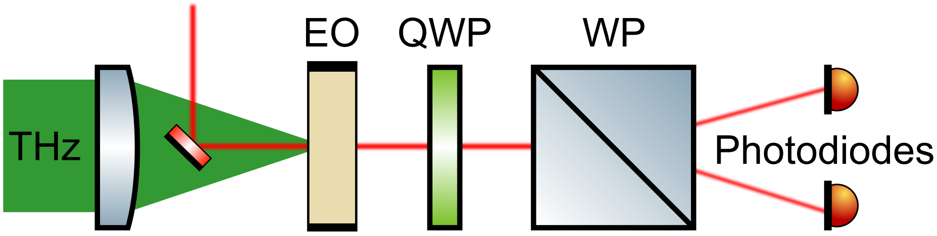

Figure 1.7: Nonlinear electro-optic detection technique for mapping THz pulses. THz beam and IR pump beam are incident on an electro-optic crystal (EO). The quarter waveplate (QWP) and Wollaston prism (WP) analyse the rotation of the pump beam polarisation caused by the THz in the EO crystal. A pair of balanced photodiodes measure this change in polarisation.

the THz field can be viewed as a DC field giving rise to a change in birefringence. By changing the delay of the THz pulse the electric field can be mapped out [88, 89]. This and the previous scheme using PCAs are the most common techniques used for detection of synchronous THz pulses in spectroscopy.

1.5.3 Thermal detectors

Bolometers are highly sensitive devices for radiation detection. These devices consist of an absorbing element connected by a thermal link to a low temperature reservoir. Any change in temperature caused by radiation incident on the absorber changes the electrical resistance of the absorber. This change in resistance can be measured and is directly proportional to change in temperature, and therefore the amount of power incident on the absorber. By applying appropriate filters to their input aperture it is possible to use them for the detection of THz. Due to their sensitivity, bolometers usually require liquid helium temperatures for operation as at higher temperature thermal noise overpowers any signal [90, 91]. These devices are large, bulky objects which limit their usefulness in a laboratory environment where space is usually at a premium. There are smaller, uncooled bolometers available – the Microbolometer – but these suffer from thermal noise and lack the sensitivity and response of their cooled predecessors [92].

Golay cells are very practical thermal detectors that compete with bolometers for detection of far-infrared/THz radiation because they are compact and operate at room temperature. A Golay cell is based on a gas chamber with an IR absorber that expands under irradiation from IR light. The detection is performed by using an optical read out system usually based on photodiodes to detect deflection of an optical beam from

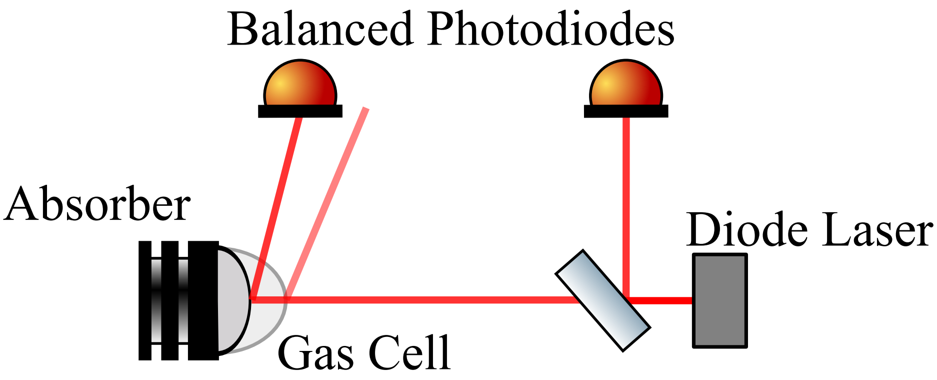

Figure 1.8: Diagram displaying the basic function of a Golay cell. A laser is reflected from the surface of a flexible membrane gas cell onto a photodiode. A reference beam is fixed incident on a second diode. THz radiation incident on the absorber causes gas within the cell to expand, flexing the membrane. This shifts the reflected laser beam away from the center of the first photodiode. As the pair of photodiodes are balanced a change in voltage is measured proportional to the expansion of the membrane.

the expanding membrane [93, 94]. A schematic of the Golay cell function is shown in figure 1.8. As the membrane expands due to heating the optical beam reflected from its surface is deflected. This deflection of the beam is registered by a balanced photodiode and displays a signal. Various filters can also be applied to the input aperture to ensure detection of the target signal. These devices are limited in their range, as the photodiode area will only allow for limited deflection of the optical beam, and noise also scales with photodiode area.

Another thermal device frequently used for detection of THz is the pyroelectric detector. In this case radiation heats a crystal, modifying its structure and generating a voltage across the crystal. The voltage response is proportional to the radiation intensity and can be used for measurements. These devices are considerably smaller and cheaper than Bolometers and Golay cells, have excellent response time and operate at room temperature. However, pyroelectric detectors are not as sensitive as alternate techniques and response quickly drops off with decreasing frequency, with poor responsivity to radiation below 0.1 THz.

1.6 Terahertz time-domain spectroscopy

After demonstrations of the generation, free space propagation and detection of broadband single cycle pulses with PCAs the field of THz time-domain spectroscopy (THz-TDS) was born [14]. THz-TDS utilises a pump-probe setup for synchronous detection of THz pulses. These systems offer a high SNR and, as the electric field of the THz pulse is directly measured, can also provide phase information which gives THz-TDS a major advantage for spectroscopy. An example of a typical THz-TDS setup is shown in figure 1.9. Here a modelocked laser input is split into a pump and probe beam. The pump beam is used to generate a THz pulse. The THz pulse is then collimated by a parabolic mirror. Such a system can utilise many parabolic mirrors or focussing lenses to cause the THz beam to come to a focus. For spectroscopy this allows materials to be placed within the focus of the THz beam, or anywhere within the collimated parts for characterisation. The pulse is then focussed onto the THz detector by another parabolic mirror and silicon lens. After passing a delay line the optical probe beam is used to gate the detector so that the instantaneous electric field of the THz pulse can be measured. The emitter is either electrically or optically modulated allowing the detection through a lock-in amplifier. The distance the probe beam pulse has to travel to the detector must be equal to the distance the pump beam pulse and generated THz must travel to reach the detector, to ensure overlap of the pulses for detection. By scanning the delay line it is possible to build an image of the electric field of the THz pulse in time. Instead of splitting the output of a single laser into pump and probe beams it is possible to use two modelocked sources and vary the pulse delay of one source with respect to the other [89, 95]. Such spectroscopy systems can also be fiber coupled, and it is common to find many THz

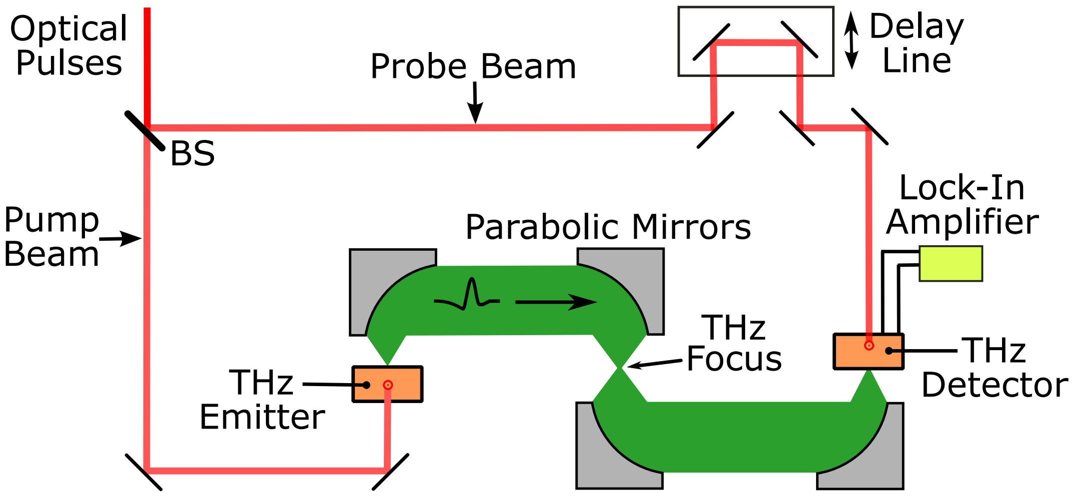

Figure 1.9: THz-TDS setup incorporating four parabolic mirrors. A laser beam is split into pump and probe beams. The pump beam excites THz radiation in the emitter. The THz field is collimated by a parabolic mirror before being brought to a focus by a second parabolic where a sample can be placed for spectroscopy. The THz is then re-collimated by a third parabolic mirror and then focussed onto the detector by a fourth parabolic mirror. The probe beam travels by an optical delay line before being directed on to the THz detector. By modulating the emitter either electronically or optically a lock-in amplifier can be used for detection, and moving the delay line varies the time at which the THz pulse coincides with the optical probe beam pulse at the detector. The center parabolics can be replaced by THz lenses. The single optical source can be replaced by two modelocked lasers with variable phase difference between their pulses to eliminate the mechanical delay line.

spectometers located within boxes for nitrogen purging to diminish the effects of water vapour absorption on the resulting spectra.

THz-TDS allows for the identification and characterisation of different materials. Organic molecules have distinct absorption spectra in the THz range, allowing for the identification of various compounds such as explosives [96] and pharamceuticals [26]. By placing a sample in the THz beam and performing TDS scans various spectrographic properties can be identified. Comparing the results with a reference scan it is possible to see how the sample has altered the THz pulse shape through absorption and reflection from the sample boundaries. By computing a Fourier transform of the THz pulse any absorption lines from the sample become evident. Further comparisons with a reference scan allow the refractive index and absorption of the sample to be computed [5, 97].

THz-TDS has become a valuable tool for the study of ultrafast carrier dynamics [98, 99] especially in; bulk semiconductors [100], quantum wells and dots [101, 102], nanoparticles [103], and even in complete devices such as photovoltaic solar cells [32]. It has been used for scanning mail and for determining pigments in paintings for art conservation purposes [46]. Many companies such as Teraview, Terasense, Menlo Systems and Toptica have released complete commercial THz spectroscopy systems and they have successfully been employed in industry for quality control. THz-TDS has also found use in the detection and characterisation of multiple thin films, especially for quality control of paint [37].

1.7 The lateral photo-Dember effect

Surface emitters operating on mechanisms such as the PD effect can be advantageous to spectroscopy systems as they do not require a bias, allowing for reduction in electrical noise and simplification of setups. Electromigration in PCAs also limits their lifetime whereas a passive component would not experience these problems [104]. The issue with these devices is the difficulty in outcoupling the THz emission due to the direction of the dipoles formed within the material. Emission is primarily in directions perpendicular to that of the exciting pump beam requiring the emitters to be angled with respect to the pump beam, thus limiting efficiency. It is due to these reasons that the high power PCA's became the emitter of choice for most spectroscopy setups.

Over time it was realised that a small amount of THz was continuing to be emitted from some PCAs when there was no electrical bias. Many attributed this to alignment and some outcoupling of the PD effect at oblique angles. However, researchers from the

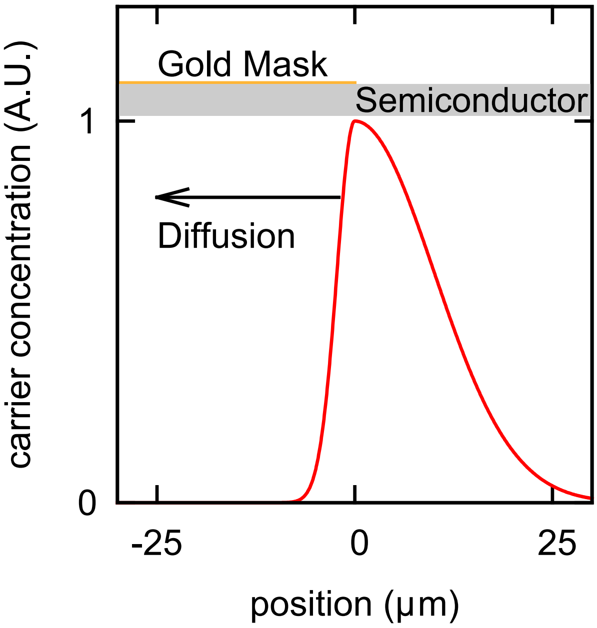

Figure 1.10: A diagram showing the initial carrier distribution near to a metal boundary in a single LPD emitter and illustrating the theory of Klatt *et al.*, 2010. The metal masks the Gaussian pump beam to create an asymmetrical distribution of photo-generated carriers. Klatt states that the increased gradient in the carrier distribution around $x < 0$ results in net diffusion of carriers under the metal mask, shown here as an arrow.

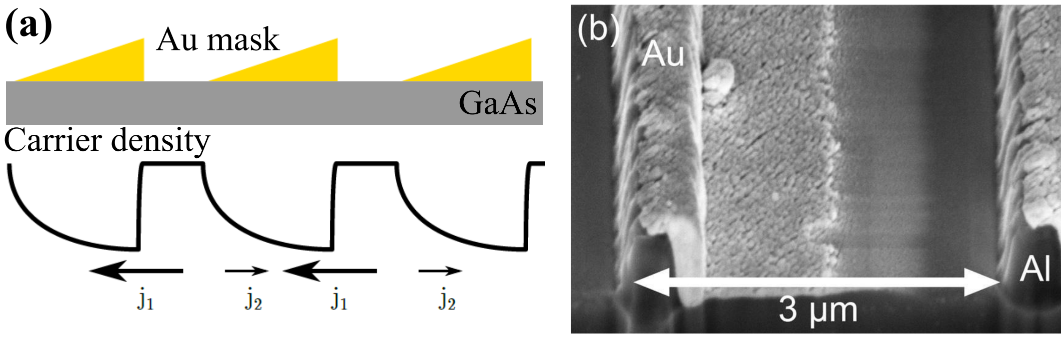

Figure 1.11: (a) shows the intended wedge pattern and resulting carrier density described by Klatt. (b) shows a SEM image showing the multiplexed emitters fabricated by Klatt *et al.* Thin walls of Al (later photoresist) are deposited on the GaAs surface. Au is evaporated at an angle to create a set of thin wedges. The gold does not show linear variation of thickness and also exhibits signs of percolation. Image used from [106].

University of Konstanz in Germany discovered that the emitted THz varied in response to the pump beam location relative to the metallic PCA electrodes. In 2010 Klatt *et al.* published work which explained that by applying a metal to partially mask the semiconductor surface and aligning the pump beam spot at the interface between the metal and semiconductor, THz emission propagating in the same direction as the pump beam can be observed [79, 105]. The emission was attributed to the formation of lateral photo-Dember currents forming due to the masking effect of the metal. In the PD effect carriers cannot diffuse past the surface, causing an asymmetric charge distribution perpendicular to the surface and resulting in THz emission. The presence of the metal mask was believed to create an asymmetric carrier concentration parallel to the surface of the semiconductor. Figure 1.10 shows the carrier concentration generated by applying a metal mask. Klatt *et al.* proposed that the lateral diffusion currents generated would be proportional to the carrier gradient. Carriers would then diffuse underneath the metal mask producing a dipole parallel to the surface which would radiate in the same direction as the exciting pump beam. This became known as the lateral Photo-Dember (LPD) effect.

A greater bandwidth is achieved by the LPD effect as well as greater power output when compared to the regular PD effect, though still only reaching one tenth the THz field strengths PC emitters are capable of supplying. This issue can be addressed by patterning different gold structures on to the surface of the emitter in order to generate multiple THz wavefronts and produce higher output powers. Based on the carrier gradient explanation, Klatt *et al.* multiplexed an LPD emitter by developing a series of three dimensional wedge shaped gold ridges on the surface of a semiconductor as illustrated in figure 1.11(a) [106]. This was done by first evaporating a periodic pattern of Al strips before repositioning the semiconductor at an angle for evaporation of Au. The goal was to produce periodic wedge shapes which would cause a steeper carrier gradient to form at the thicker edge compared to the thinner edge, leading to a net dipole and

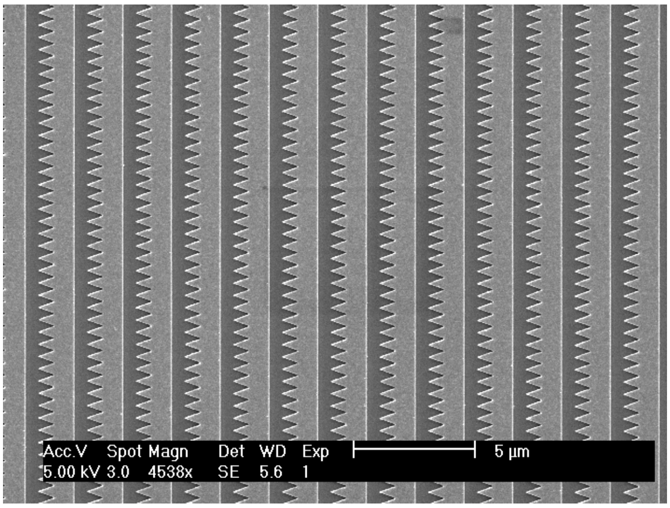

Figure 1.12: An image of the two dimensional emitters designed by Duncan McBryde and fabricated by Anthony Brewer by electron beam lithography. The emitters were designed based on Klatt's interpretation of the LPD mechanism. The failure of these emitters to produce observable THz led to the formation of a new LPD theory based on the suppression of dipoles due to the presence of a metal mask.

THz emission. The multiplexed emitters enhanced the observed THz emission but such structures can prove difficult to manufacture. Figure 1.11(b) shows a SEM image of the fabricated emitters. The intended wedge shapes were not fully formed, leading to a more step-like pattern. Other techniques have since developed in order to ease fabrication of these structures, such as forming a series of photoresist ridges on a semiconductor and evaporating gold onto the surface with the sample placed at an angle to reduce the photolithography steps from two to one [107].

1.7.1 Southampton work

Based on the LPD mechanism proposed by Klatt, Duncan McBryde modelled a design of two dimensional triangular emitters to simplify the fabrication of multiplex devices [108]. The design of the device (shown in figure 1.12) consisted of periodic metal strips with a staight edge along one side and triangular structure along the opposite side to break the symmetry of the system and create an asymmetrical carrier distribution. However, modelling of the electrode pattern showed that the currents formed at each metal edge were still equal and opposite and so would only generate THz emission in the presence of an applied electric field. The device was fabricated and tested and found to not produce observable THz emission. The discrepency between the theory and evidence led Mark Barnes to develop an alternate theory for the LPD effect [109]. Through further modelling of the drift and diffusion of carriers within a semiconductor it was shown that carrier diffusion and recombination could not alone be responsible for a net current and THz generation. Comparisons with a PCA showed that the THz field from an LPD emitter is produced by a current direction away from the metal mask, opposite to that proposed by Klatt, who stated the radiative dipole is created due to the difference in the carrier distribution $\frac{\partial N}{\partial x}$ forming a current direction towards and underneath the metal. For a finite distribution of carriers (N) the net current (J), and therefore the net dipole due to diffusion, must always be equal to zero.

$$J = \int_{-\infty}^{\infty} j\,\mathrm{d}x \propto \int_{-\infty}^{\infty} \frac{\mathrm{d}N}{\mathrm{d}x}\mathrm{d}x = [N]_{-\infty}^{\infty} = 0. \tag{1.1}$$

With no net current no lateral net dipole can form and no THz can be generated. This was demonstrated experimentally in our group by imaging a knife edge shadow on the surface of a semiconductor to produce an asymmetrical pump spot illumination [110]. If Klatt's theory was true this asymmetrical illumination would produce an asymmetrical carrier distribution and the diffusion of carriers would produce THz. The experiment resulted in no net THz generation and led to the formation of a new hypothesis for the

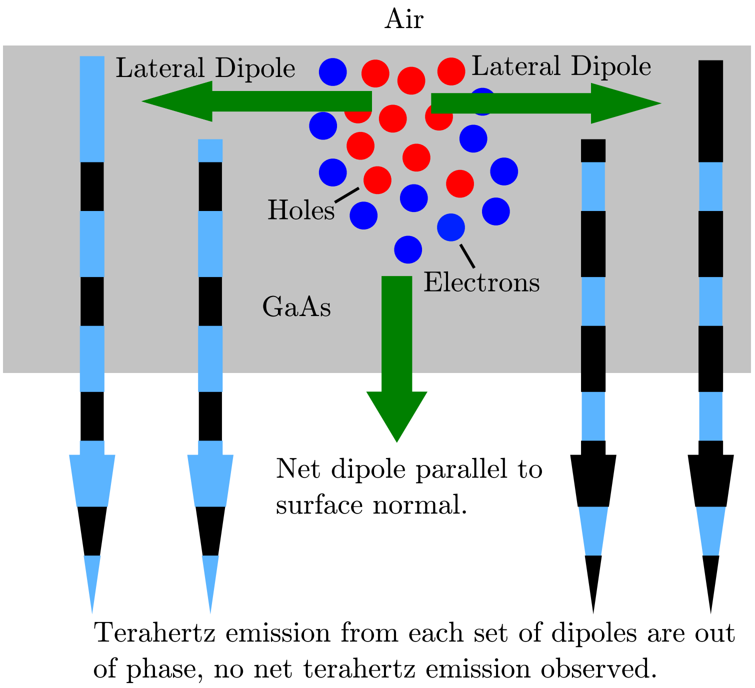

Figure 1.13: A diagram showing the dipoles formed in an unmasked semiconductor. THz emission is represented by blue arrows with black markers representing relative phase. Green arrows represent dipoles and their direction. Photo-generated carriers diffusing perpendicularly into the material create an asymmetric distribution due to the constraint of the surface. This generates a typical PD dipole perpendicular to the surface. Carriers diffusing laterally do so in opposite directions, creating opposing dipoles. THz emission from these opposing lateral dipoles has a π phase difference, leading to destructive interference and no THz emission perpendicular to the material surface.

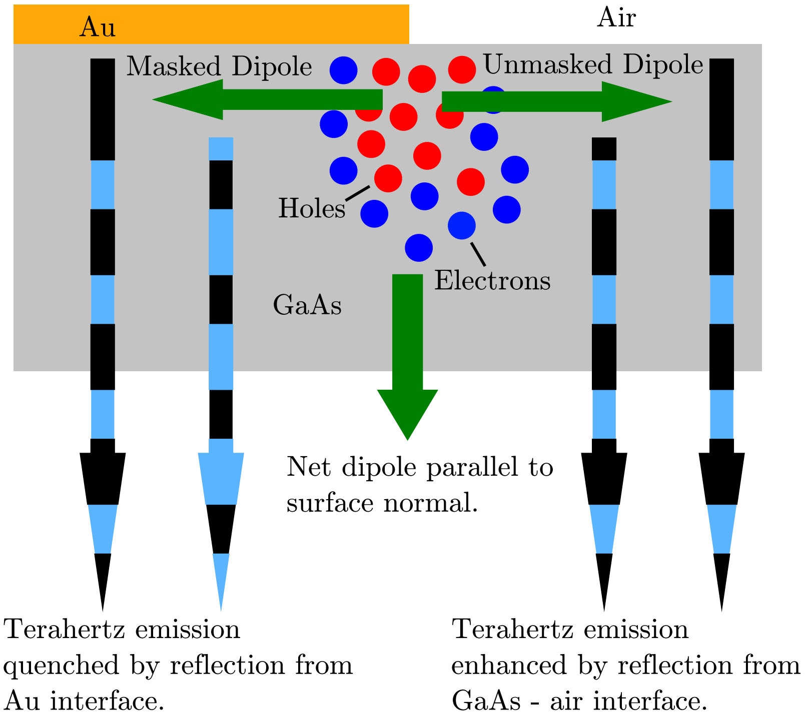

Figure 1.14: A diagram showing the dipoles formed in a masked semiconductor and the mechanism of the LPD effect. THz emission is represented by blue arrows with black markers representing relative phase. Green arrows represent dipoles and their direction. As for the unmasked emitter in figure 1.13 a dipole forms perpendicular to the surface. Carriers are generated close to the metal mask and diffuse both away from the metal and underneath it, creating opposing dipoles. The dipole formed below the metal mask can radiate but the reflection from the metal gains a π phase shift and so interferes with the unreflected radiation from this dipole, suppressing emission. The uncovered dipole is free to radiate unsuppressed, as reflection from the semiconductor surface alone does not result in a π phase shift.

generation of THz from the LPD effect based on the inhibition of dipoles due to the presence of the metal mask.

For a pump beam aligned on a bare semiconductor (figure 1.13), carriers generated are free to diffuse in all directions. The surface of the semiconductor introduces a boundary that carriers cannot cross, so an asymmetrical carrier distribution is formed perpendicular to the surface allowing THz emission parallel to the semiconductor surface. This is the typical situation of the PD effect. Lateral dipoles also form parallel to the semiconductor surface, however, they are equal and opposite so any THz emission produced by these dipoles will cancel out in the far field. For an unmasked semiconductor with the surface perpendicular to the pump beam there is no net lateral diffusion current and no THz emission in the same direction as the exciting beam.

In the case of the lateral photo-Dember effect a pump beam aligned along the interface between a metal mask on a semiconductor will generate carriers in this region. The carriers generated by the half-masked laser spot diffuse into the semiconductor material both away from and underneath the metal edge. The steep gradient caused by the metal mask creates an asymmetric carrier distribution, shown in figure 1.10. This creates two equal, opposing dipoles forming close to the metal edge as shown in figure 1.14, resulting in a zero net diffusion current. Both dipoles can radiate, however the dipole formed underneath the mask experiences a reflection from the metal. For a wave of amplitude, E_i, incident upon a surface the reflected amplitude (E_r) can be calculated with the relation;

$$E_r = \frac{n_1 - n_2}{n_1 + n_2} E_i \tag{1.2}$$

Where n_1 is the refractive index of the initial material and n_2 is the refractive index of the material from which the wave is reflected. In the case where $\mathrm{n}_1 = \mathrm{n}_2$ no reflection is experienced. When $\mathrm{n}_1 > \mathrm{n}_2$, E_r and E_i have the same sign and the reflection experiences no phase shift. For cases where $\mathrm{n}_1 < \mathrm{n}_2$, E_r and E_i have opposite signs and the reflected wave gains a π phase shift relative to the incident wave. For THz frequencies the real parts of the refractive indexes of GaAs and Au are typically 3.4 and ∼500, respectively [111]. For the dipole below the mask its radiation is reflected by the metal surface and acquires a π phase shift due to the refractive index change between the semiconductor and metal. If the distance of the radiating dipole from the metal is less than the emission wavelength then the dipole is suppressed [112]. The surface reflection of the uncovered dipole does not experience this phase shift and so is allowed to radiate freely and emits a THz pulse perpendicular to the surface (figure 1.14). It is this suppression due to the presence of a metal mask which allows a net dipole to radiate, and thus is the driving mechanism behind the LPD effect.

For further computational support I encorporated the drift-diffusion model with a COMSOL multiphysics model of a LPD emitter both with and without a metal mask present. This work is presented in *Chapter 2* and published in [110]. My model supports the dipole suppression due to reflection hypothesis, as well as showing that emission in the direction of the exciting beam can only occur with a metal mask present. Without the metal mask present a quadrupole emission pattern is observed which does not propagate perpendicular to the pump beam. A comprehensive computational study of the carrier dynamics in a semiconductor which lead to THz emission was also produced, employing both 1D numerical and Monte-Carlo simulations. The results of this showed that, despite the pump spot size and shape, there will always be no net carrier diffusion and THz will only be observed in cases were a metal mask is present to asymmetrically inhibit dipoles [113].

Further experimental work was also carried out. A LPD emitter was fabricated consisting of two metal masks; one deposited directly onto the semiconductor and one with an insulating Polyimide (PI) layer deposited between the metal and semiconductor to eliminate any contact effects (schematic shown in figure 1.15 (a)). The pump beam was aligned on each opposing metal edge in turn and the resulting TDS scans are shown in figure 1.15 (b). This shows equal and opposing TDS traces, revealing that there are no contact effects between the metal and semiconductor strongly influencing THz emission, offering further support for the dipole suppression interpretation of the LPD effect. The dipole suppression theory was then used to design a multiplexed emitter comprised of periodic Au strips fabricated on the surface of a semiconductor. Aligned with a cylindrical lens array so that the pump beam was focused on correlated Au edges, the device showed over five times improvement in the signal obtained when compared with a single LPD emitter. These devices were characterised and the results are shown in *Chapter 3* and are published in [114].

An in-depth investigation of the effects of pump beam fluence and polarisation on the THz produced from SI-GaAs and both annealed and unannealed LT-GaAs was carried

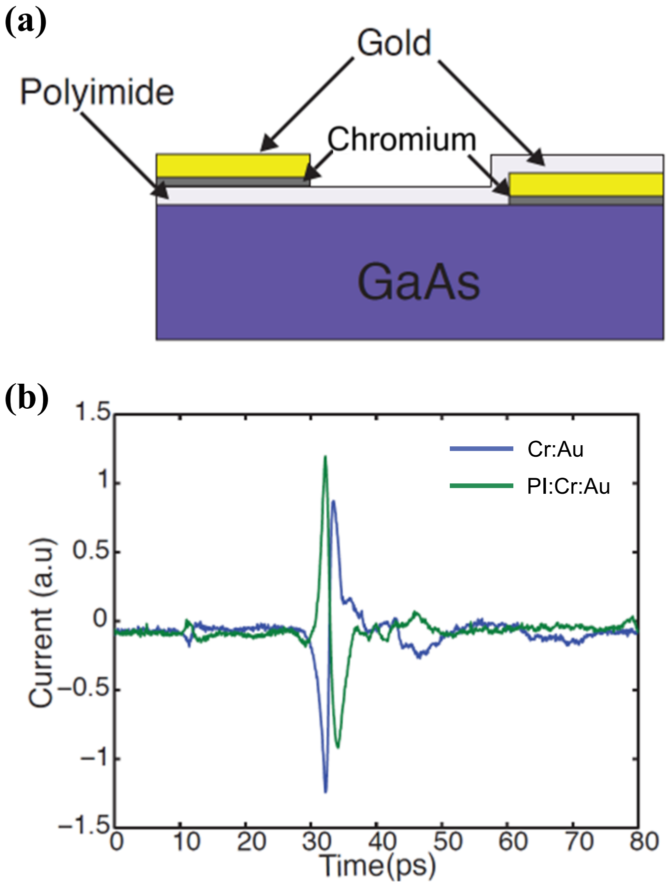

Figure 1.15: Figure (a) shows a schematic of the partially-insulated emitter. The right-hand metal mask is fabricated directly onto the semiconductor surface. The left-hand metal mask is fabricated with a PI layer between the metal and semiconductor to eliminate any surface effects. Figure (b) shows the THz-TDS traces for LPD emission from each of the metal edges. Both are equal with reversed polarity due to illuminating opposing metal edges, showing that it is just the LPD effect contributing to THz emission with no surface effects involved.

out, with results published in [115]. The results showed that LT-GaAs exhibits a higher saturation fluence (and therefore higher THz emission) than SI-GaAs, with unannealed LT-GaAs showing the highest saturation fluence. It was also noted that at high fluences SI-GaAs based emitters exhibited a flip in signal polarity, which was attributed to the effects of the metal contact with the semiconductor. This led to the work discussed in *Chapter 4* where the effects of the Schottky barrier between metal and semiconductor were explored and used to enhance the emission of LPD emitters. A multiplexed emitter with overlapping double-metal strips was designed to utilise both these Schottky effects and the LPD effect to produce net THz emission without the need for focusing elements. This work has also been published in [116, 117].

With no external bias required, LPD emitters are easy to fabricate, demonstrate improved lifetime and can be integrated with other elements and into existing set ups with ease.

1.8 Thesis outline

The work presented in this thesis lends support to the theory of dipole suppression in the LPD effect and describes through simulations and experimental evidence ways of increasing the THz emission of LPD emitters through multiplexing, as well as exploring ways to manipulate the emitted radiation.
In *chapter 2* numerical and finite element analysis models are used to investigate the origins of the LPD effect. These models demonstrate the importance of the metal mask to the THz emission, supporting the theory of dipole suppression beneath the metal. The results from these simulations have been published in *Optics Express* [110] and the *Journal of Infrared, Millimeter and Terahertz Waves* [113]. Models are also used to investigate the effect of dipole distance from the metal mask on emission.
In *chapter 3* multiplexed LPD emitters are investigated computationally and experimentally. The multiplexed geometry is modelled using the method discussed in *chapter 2*. The use of a cylindrical lens instead of an achromatic doublet lens for focussing onto a single edge LPD emitter is investigated to quantify the difference. Multiplexed LPD emitters are fabricated and aligned with a micro-lens array to produce a net emission of THz. These emitters are characterised and found to have similar performance in bandwidth and SNR to commercial PC antennas whilst boasting over five times the amplitude of a single edge LPD device. They are durable and easy to fabricate and the results discussed in this chapter have been published in *Applied Physics Letters* [114].
In *chapter 4* multiplexed emitters consisting of double-metal elements which do not require alignment with lens arrays are explored. The theory behind their function is described, exploring both contributions from Schottky effects and the LPD effect, and the fabricated emitters are fully characterised. The results from the initial fabrication and characterisation are published in *Applied Physics Letters* [116]. Different metal

pairings are compared and their performances at low temperatures are measured. The results of these studies show these devices to exhibit good THz emission under various conditions, including at low teperatures and low ambient pressures. These results have been published in *Electronics Letters* [117]. The alignment of these emitters is non-critical, allowing them to act as a drop-in component in any existing THz setup. They remain easy to fabricate, do not require a bias and offer similar performance to PC antennas.

Chapter 5 explores the beam steering and focussing characteristics of the emitters described in chapter 4. By controlling and manipulating the IR pump beam it is possible to control the emission of THz, directing or focussing the beam as desired. This is useful in coupling THz directly into waveguides or for building robust, compact spectrometer systems where no THz beam optics are required. Alternate double-metal structures are also shown to produce different polarisation profiles of the emitted THz. These results are currently unpublished.

Finally, in *chapter 6* is a summary and conclusion of the work presented in this thesis, with an outlook towards the future of THz technologies.

Chapter 2

Modelling the lateral photo-Dember effect

In this chapter the lateral photo-Dember (LPD) effect is investigated using numerical modelling and finite element analysis techniques. A numerical method is used to model the generation of carriers within a semiconductor and their movement due to diffusion and drift. The results from this are then incorporated into a finite element analysis program (COMSOL multiphysics) to model fully the effect of the metal mask in the LPD effect. Results from this model support the theory of dipole suppression by reflection from the metal and are backed up by experimental evidence. The work in this chapter was done in conjunction with Sam Berry and Mark Barnes and has been published in [110] and [113].

2.1 Introduction

The LPD effect allows the generation of THz radiation propagating parallel to the direction of the optical pump beam without the need for an external bias. The LPD effect was discovered by Klatt *et al.*, and relies on the semiconductor being partially masked with a metal [105]. When the optical pump is aligned along the metal edge, THz emission is produced and can propagate in the same direction as the optical pump beam. THz generated like this is much simpler to outcouple and detect compared to that generated using the PD effect. The theory behind this effect proposed by Klatt is demonstrated in figure 2.1(a). The metal partially masks the optical pump spot creating an asymmetric illumination pattern. This generates a strong carrier gradient close to the metal edge which allows carriers to diffuse underneath the metal. The mobility difference between electrons and holes in GaAs based semiconductors allow a charge seperation to form creating a dipole parallel to the material surface which radiates on a picosecond

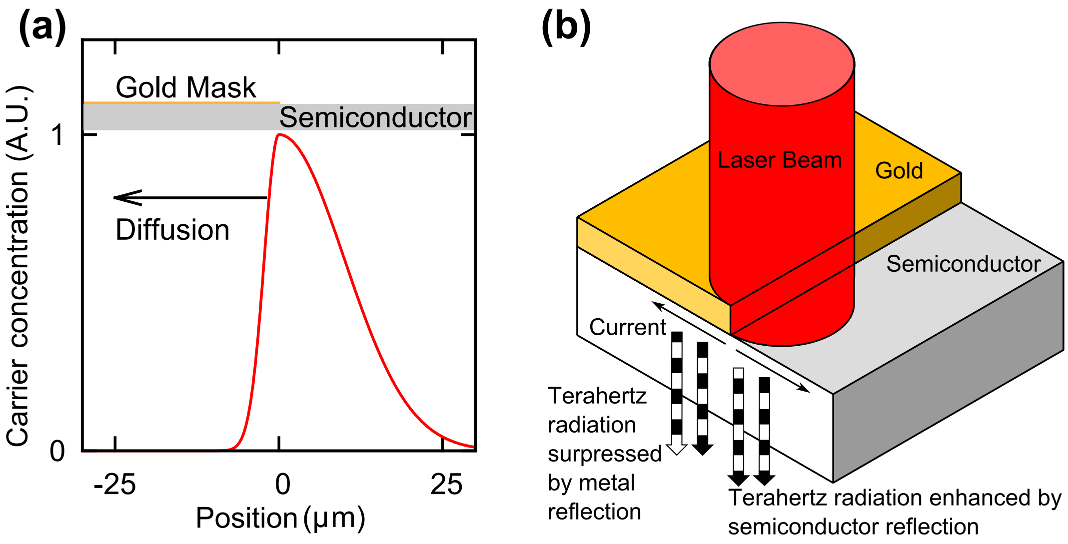

Figure 2.1: Figures showing the opposing interpretations of the LPD effect. In (a) is Klatt's theory, where the steep carrier gradient causes a carrier diffusion underneath the metal mask leading to a net current and THz emission. In (b) is a demonstration of the theory that there cannot be a net current but the dipole formed underneath the metal is suppressed by reflection, allowing the exposed dipole to radiate freely.

time scale. Klatt's interpretation of this means that the dipole formed under the metal mask radiates THz.

Work done in Southampton noted that any carrier concentration starting from zero and ending at zero would be unable to produce a net current. For a symmetrical carrier distribution this is obvious, as carriers diffusing in opposite directions will, at all times, produce zero net current. However, this is also true for asymmetrical carrier distributions, a statement which can be supported by considering the microscopic current distributions proportional to $\partial n_e/\partial x$. In this case the total current due to diffusion will be equal to $\int (\partial n_e/\partial x)\, dx$ between a large negative and large positive number. If the initial and final concentrations are zero then the integral will be equal to zero. A net current can not be produced by diffusion alone so the metal mask must play a different role to that interpreted by Klatt [109]. We proposed that carriers diffusing near the metal mask would produce two opposing lateral dipoles, one formed away from the metal and one formed underneath. The dipole formed underneath would be able to radiate but any emission which was reflected by the metal mask would experience a π phase shift, resulting in the dipole under the mask being suppressed. The dipole formed away from the metal would then be able to radiate freely and would do so perpendicular to the material surface, in the same direction as the pump beam (illustrated in figure 2.1 b). In our interpretation of the LPD effect it is the uncovered dipole that radiates, the opposite dipole to that which Klatt proposed would radiate. To test this theory, a PCA was used to determine which direction the THz field was oriented before turning off the bias to allow the device to function as an LPD emitter and record the direction of the field. From this it was determined that the THz field for an LPD emitter was oriented away from the metal edge, lending the first evidence in favour of the theory of dipole suppression [109].

2.2 Numerical drift-diffusion model

A 1D numerical drift-diffusion model similar to that in [78, 82] was created in Matlab and used to simulate the ultrafast generation of carriers within a GaAs semiconductor. The model takes into account the carrier generation, recombination and currents due to drift and diffusion. Carriers in the model are generated within a 1D space from arbitrary concentrations in both space and time. The generated carriers are free to drift and diffuse based on the carrier gradient, their diffusivity, mobility and the local electric field. They may also recombine or become trapped by defects. These calculations are made for each time step within the simulation. The equation which governs the evolution of the electron and hole densities, including both electric field and diffusion terms is,

$$\frac{\partial n_e}{\partial t} = \mu_e \frac{\partial}{\partial x}(n_e E) + D_e \frac{\partial^2 n_e}{\partial x^2} - b(n_e n_h) - \frac{n_e}{\tau_1} + G\,(x,t) \tag{2.1}$$

where the electron density is n_e, the hole density is n_h, the electric field caused by differing carrier mobilities is E and $G\,(x,t)$ is the optical generation term, determined by the laser spot shape, size and length. The mobility, μ, and the diffusion coefficient, D, follow the Einstein relation assuming quasi-thermal equilibrium [109]. τ_1 is the carrier density lifetime due to recombination via fast traps and b is the bimolecular recombination

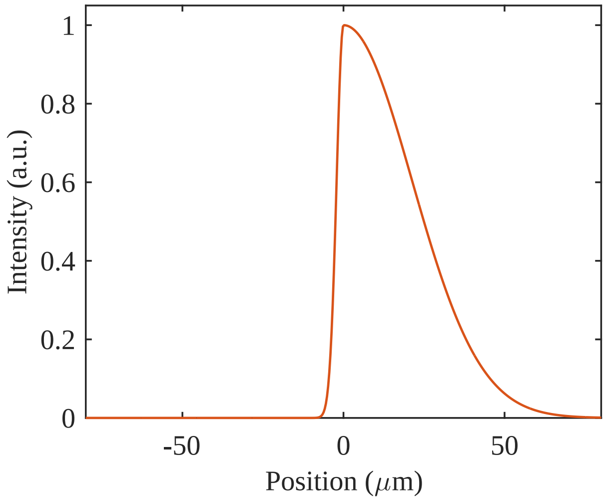

Figure 2.2: Spatial profile of a half-masked gaussian beam. This is the pump spot profile used in the drift diffusion model to excite an asymmetrical carrier distribution. The $1/e^2$ spot radius was set to 30 μm with the spot modelled asymmetrically to represent masking.

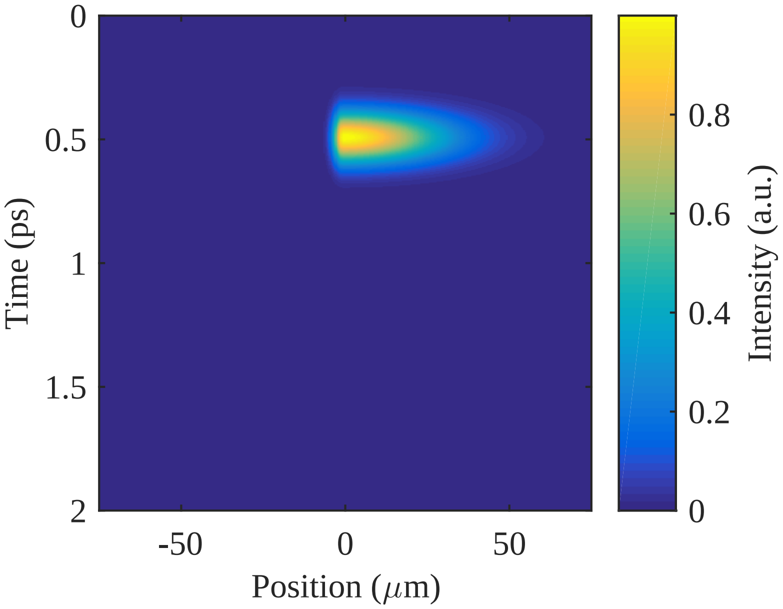

Figure 2.3: Normalised spatial and temporal profile of a half masked pump beam spot of pulse length 100 fs. The $1/e^2$ spot radius was set to 30 μm with the spot modelled asymmetrically to represent masking.

constant for carrier-carrier recombination. A similar equation was used for hole evolution. D was related to the carrier mobility and temperature, T, through,

$$D_{e,h} = \frac{\mu_{e,h} \; k_b \; T_{e,h}}{e} \tag{2.2}$$

The excess energy from the optical pulse means that the transient carriers experience a steep rise in temperature shortly after photoexcitation. Due to different energy dissipation rates of electrons and holes, and that the lattice temperature does not noticeably increase, it is assumed that the holes remain at room temperature [78]. The hot electrons experience increased mobility, though this is still negligible compared to the mobility change that would occur through doping [82]. The material properties of LT-GaAs used during the simulation were taken from [51, 78, 82, 118, 119] and are displayed in table 2.1. The incident electric

Electron temperature, T_e	3000 K
Hole temperature, T_h	300 K
Bimolecular recombination constant, b	20 x 10^6 cm s^{-1}
Carrier density lifetime, τ_1	200 fs
Electron mobility, μ_e	8500 cm^{2}V^{-1}s^{-1}
Hole mobility, μ_h	400 cm^{2}V^{-1}s^{-1}

Table 2.1: Table of properties for LT-GaAs used in the numerical drift-diffusion model from [51, 78, 82, 118, 119]

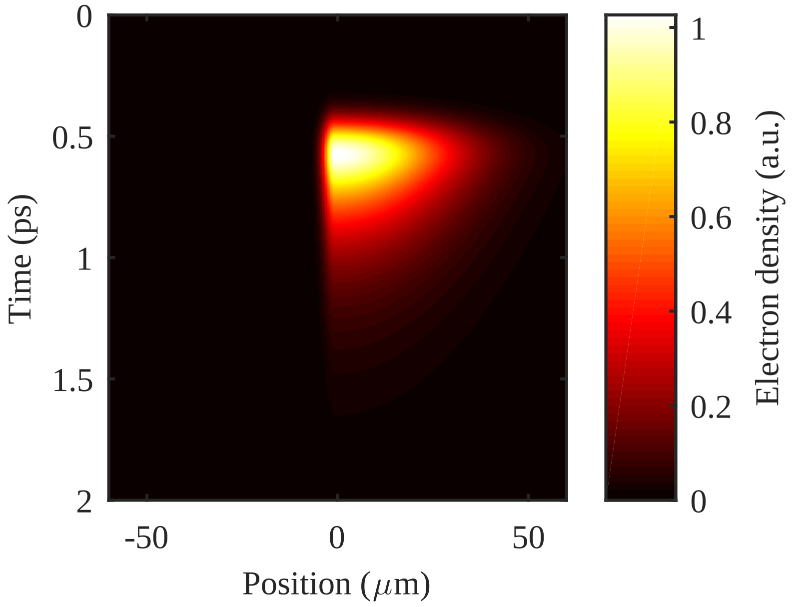

Figure 2.4: Simulation results of the evolution of carrier density for electrons after excitation by the pump beam profile of figure 2.3.

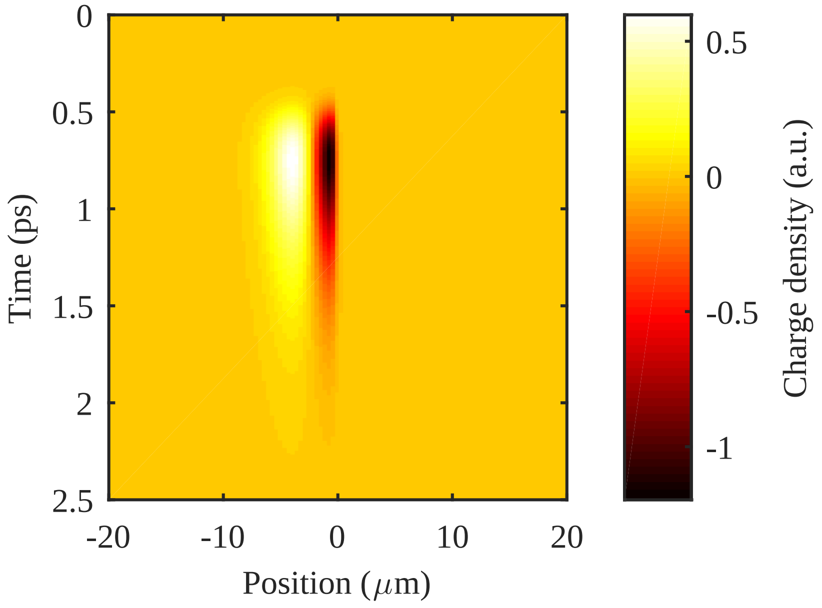

Figure 2.5: Simulation results of the time evolution of the difference in electron and hole distributions after photoexcitation. Negative values represent holes while positive values represent electrons. Close to the metal edge a separation of charge is caused due to the mobility difference of electrons and holes.

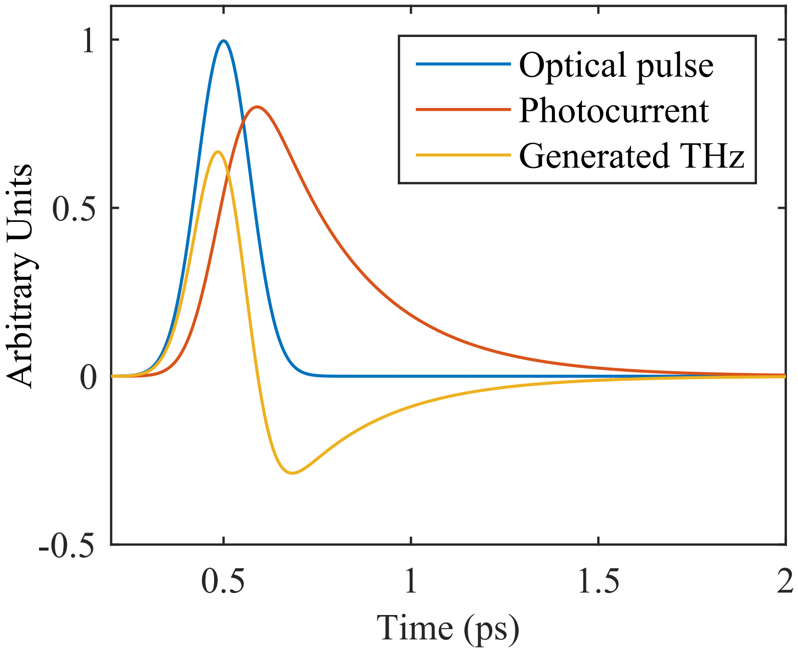

Figure 2.6: Simulation results of the time evolution of the unmasked half of a photocurrent (orange line) generated by an optical pulse (blue line) and the resultant THz (yellow line). The photocurrent generated is a convolution of the temporal envelope of the optical field with the impulse response of the semiconductor. The emitted THz is then the derivative of the changing photocurrent.

field was modelled as a half-gaussian in space to represent the laser spot which is partially masked by the metal layer. Figure 2.2 shows the spatial profile of the modelled pump spot, with a $1/e^2$ spot radius set to $30\,\mu$m and the spot modelled asymmetrically to simulate partial masking. For each time step in the simulation the electric field was calculated by solving Poisson's equation. The change in carrier concentration was calculated with equation 2.1 and the simulation was updated for the next iteration. The time step used for the model was 4 fs and the model space was quantised with a mesh size of 350 nm. These parameters were chosen to produce high resolution results for input into COMSOL multiphysics at a later time. The model assumes a constant mobility for the carriers, however for times shortly after photoexcitation this is not true and the mobility is a function of time [120]. As the electric field increases with time and carrier diffusion with no sudden changes in carrier velocity, the effects of any small mobility change are expected to be negligible. The model also does not consider the effects of velocity overshoot as the currents are formed mainly from diffusion instead of drift so the results are unlikely to be affected.

The evolution of the incident electric field modelled as a Gaussian in time and half gaussian in space is shown in figure 2.3. The resulting carrier density for electrons calculated by the simulation is shown in figure 2.4 and a similar distribution is calculated for the holes. The half gaussian electric field generates an asymmetric distribution of

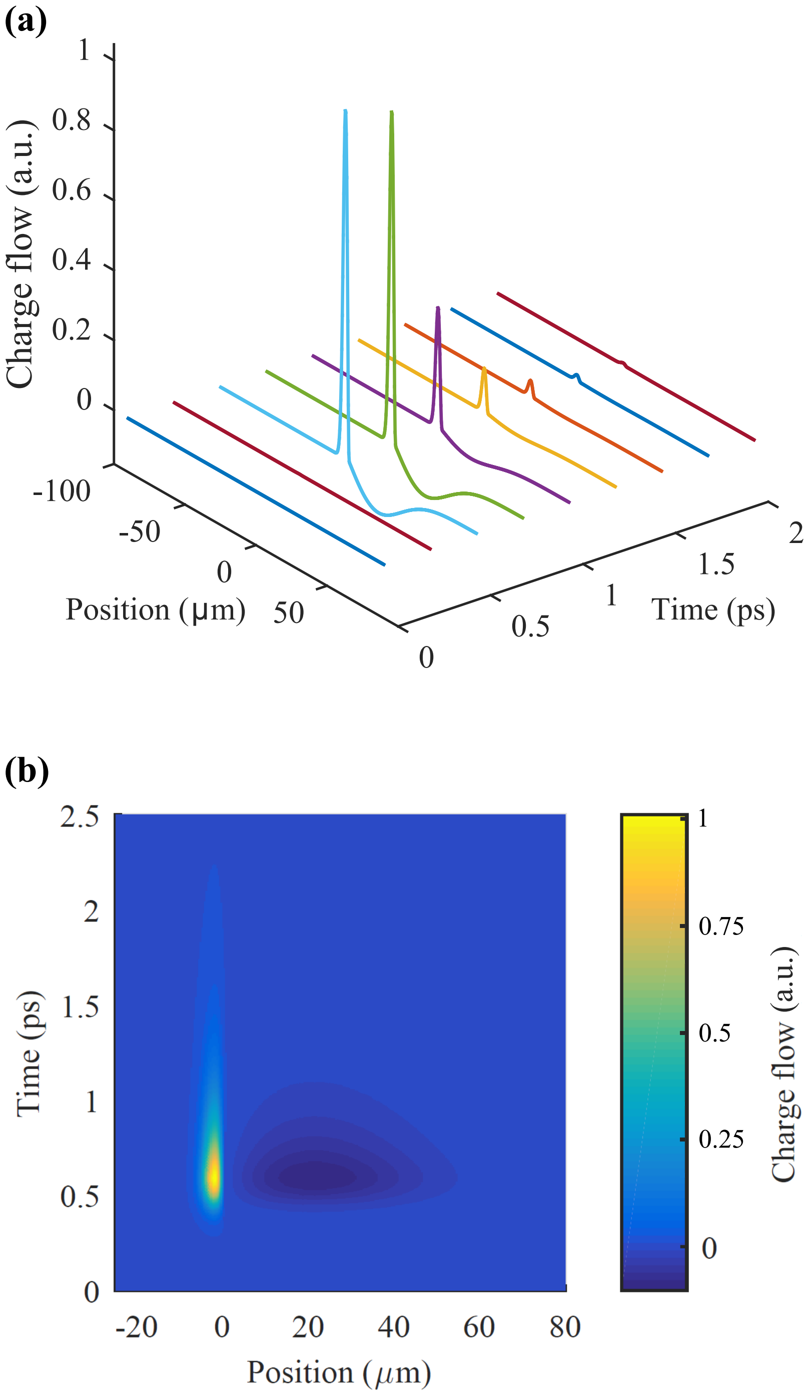

Figure 2.7: Simulation results of the 1D charge flow with time. Figure (a) shows a plot of charge flow with position from 0–2 ps in steps of 0.25 ps. Figure (b) shows a surface plot of the simulation results. There is no net current generated, suggesting the presence of the metal mask plays the key role in LPD emission.

carriers within the semiconductor. These carriers are able to undergo drift and diffusion before recombining or becoming trapped at defect sites. The carriers can diffuse past the boundary created by the half gaussian electric field and, as the electron mobility is much higher than that of the holes, a charge seperation is formed. Figure 2.5 shows the difference between the electron and hole distributions. The difference in carrier densities close to the mask edge allow for the separation of charge.

Movement of charge results in a current. For both symmetrical and asymmetrical charge distributions starting from zero, at any point in time the net current will be equal to zero [113]. Figure 2.6 shows the time evolution of the optical field used in the model and the resulting photocurrent produced in one half of the model. The optical pulse lasts for 100 fs and frees carriers within the semiconductor. A photocurrent is produced through the diffusion and recombination of these carriers (represented by the orange line). Emission caused by this can be estimated from the differential of generated photocurrent. This is plotted as the yellow line and takes the form of a typical THz pulse, however, as there is no net current this cannot be observed parallel to the excitation beam. Figures 2.7(a) and (b) show the resulting charge flow from the asymmetric carrier generation in the model and its evolution in time. The flow of charge close to the metal mask is large and confined to a small area, whereas away from the mask the charge flow is much lower but spread over a large region. This results in a total current across the simulation of zero, demonstrating that the drift-diffusion current from an asymmetrical distribution alone cannot result in observable THz emission parallel to the excitation beam.

2.3 Incorporation with COMSOL multiphysics

To ascertain the function of the metal mask on the emission of THz the results of the drift-diffusion model were incorporated into a COMSOL Multiphysics simulation, a finite element analysis program, with geometry based on a single LPD emitter. The simulation modelled a piece of 100 μm thick GaAs partially masked with a Au layer and otherwise surrounded by air. The Au boundary is modeled as a perfect electrical conductor, meaning that 100% of the incident field is reflected and does not penetrate the metal. The current calculated from the drift-diffusion model discussed previously was imported into COMSOL. These results were used as the model for a current on a 30 μm long 1D wire located 1 μm below the GaAs surface (inset of figure 2.8). The spatial mesh size used for the wire in COMSOL was matched to the spatial resolution of the Matlab model. The simulation was run using COMSOLs ‘Transient Electromagnetic Waves’ module for a duration of 4 ps, equal to that of the duration of the Matlab model. The simulation was repeated without the Au mask present for a direct comparison of the affect of the metal on the observed THz emission.

The results for these simulations are shown in figure 2.8. The images on the left show the resulting emission without the gold mask present. The images on the right show the resulting emission with the Au mask. From top to bottom the cases are shown over time steps of 0.5, 1, 1.5 and 2 picoseconds from the initial generation of current in the wire. In the case without the metal mask present a quadrupole radiation pattern is detected. This would give no emission in the direction parallel to that of the exciting pump beam. With the gold mask present the dipole underneath the metal is suppressed and the uncovered dipole is allowed to radiate perpendicular to the material surface. This shows that THz emission along the laser propagation axis can exist only if there is a metal mask present near to the carrier concentration. This was measured experimentally

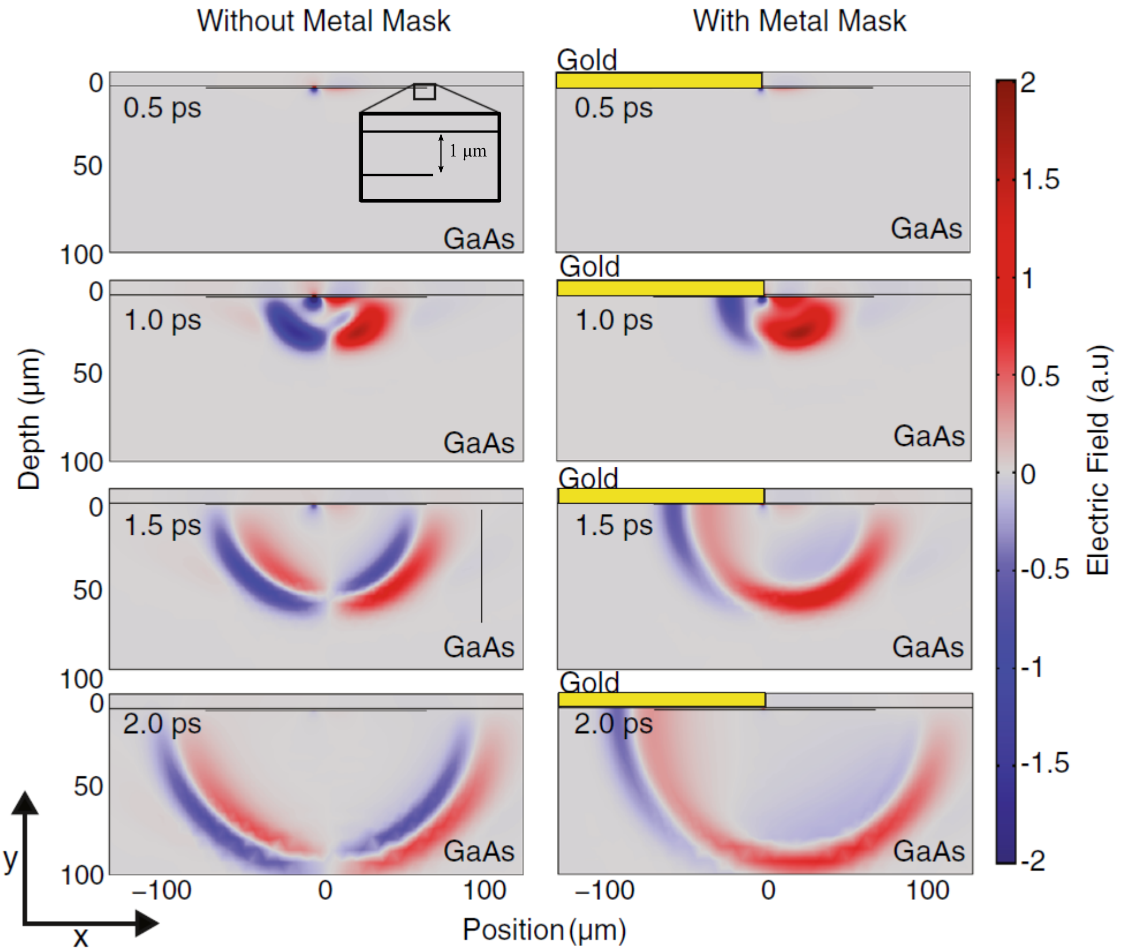

Figure 2.8: Simulation results of the dynamic electric field produced in GaAs by drift and diffusion from an asymetric carrier distribution. Red is positive and blue is negative field. From top to bottom are images in time steps of 0.5 ps. The left-hand images show the THz emission without a metal mask present. A quadrupole emission pattern is observed with no radiation propagating perpendicularly to the material surface. The right-hand images show the THz emission with a metal mask present. The dipole formed beneath the metal experiences suppression from reflection and the uncovered dipole is able to radiate perpendicular to the material surface.

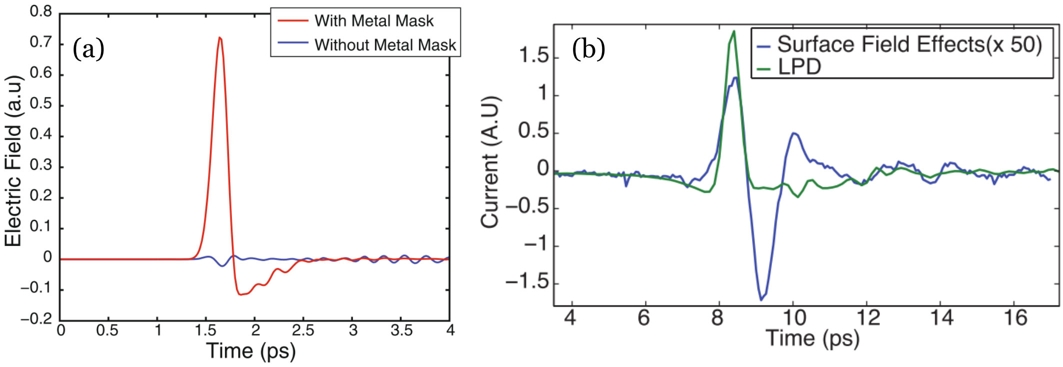

Figure 2.9: Figure (a) shows simulation results of the emitted electric field measured at the bottom centre of the model. The red line represents the emission observed when a metal mask is present. The blue line shows the emission observed without a metal mask. Figure (b) shows experimental results of THz radiation from a Gaussian pump spot on bare LT-GaAs in comparison to the radiation observed from radiation near a metal edge (LPD effect). THz radiation from bare LT-GaAs originates from diffusion currents and surface fields, due to the strong focusing provided from the combination of the Si-lens and parabolic mirrors. In both experimental and simulated cases emission in the same direction as the pump beam cannot be observed for an asymmetrical carrier distribution alone, a metal mask must also be present.

by imaging a partially masked gaussian pump beam on to a piece of semiconductor. No THz was measured for excitation with an asymmetrical pump spot, however, when a metal mask fabricated on the semiconductor surface was translated into the shadow of the beam, THz emission was observed. Figure 2.9(a) shows the electric field measured in both situations at the bottom center of the simulation as a function of time. This demonstrates that THz emission which is colinear with the propagation of the optical pump beam will only be observed when a metal mask is present. The emission measured in the presence of a metal mask in the COMSOL model also follows the expected profile predicted from figure 2.6. Figure 2.9(b) shows experimental THz-TDS scans supporting the results of figure (a). The green line shows the THz pulse profile when the pump spot is aligned close to a metal edge fabricated on LT-GaAs. The blue line shows a similar scan made when the pump spot is incident on bare LT-GaAs with no metal mask present. The emission in the case of the blue line is primarily due to surface field effects in the substrate and as such is around 50 times weaker than LPD emission. The results from figure (b) align almost identically with the simulation results of figure (a) in shape, however the experimental data shows some broadening of the THz pulse. This is due to the nature of real world measurements compared to the idealistic model. The simulation assumes only a 1D current within the emitter whereas in reality there would be contributions from a much larger space. The setup used for taking measurements involves collimation and focusing of the THz beam, as well as propagation through silicon lenses and air, all leading to a broader pulse than what is observed in the model.

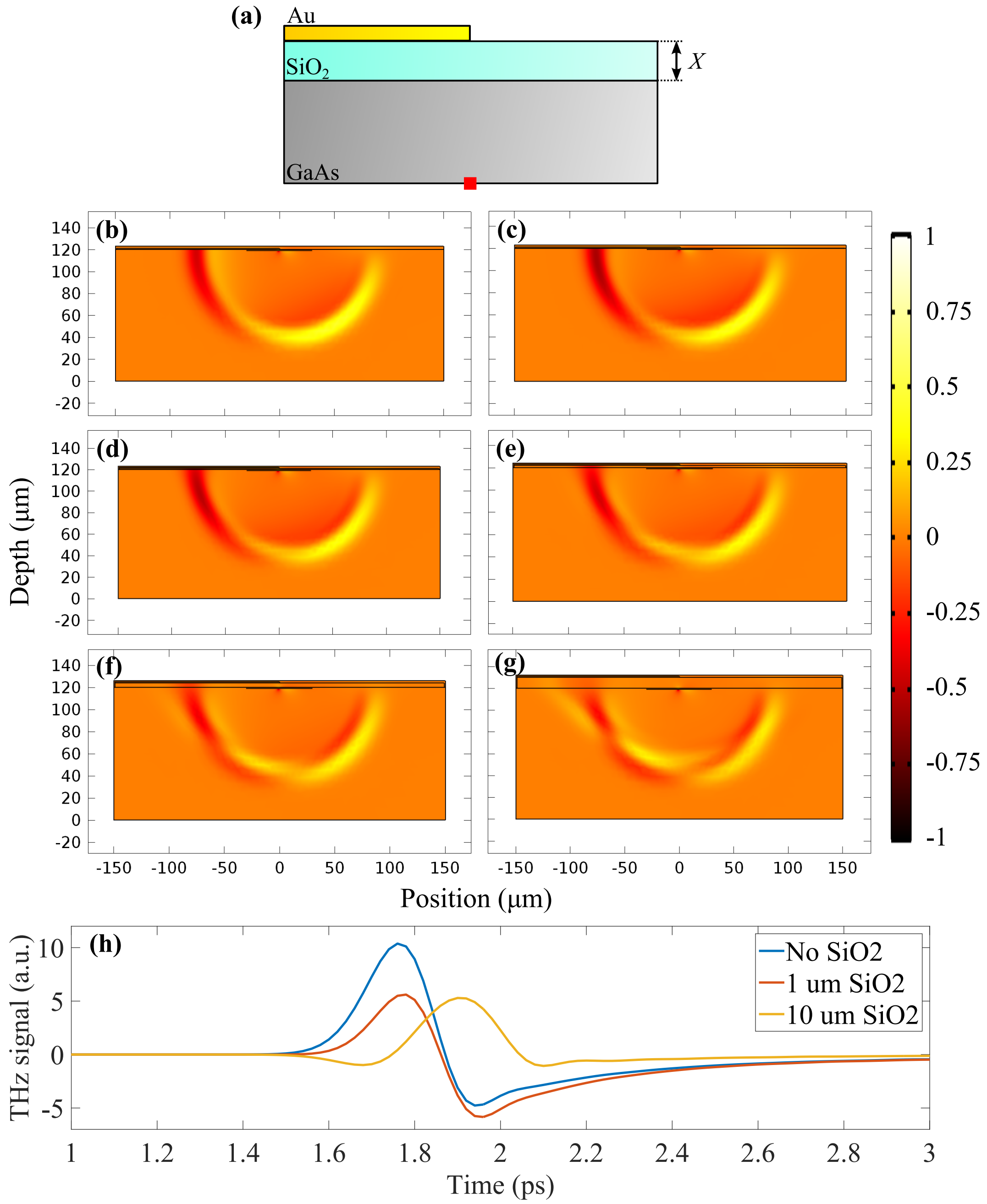

Figure 2.10: Simulation results of the emitted electric field produced for different insulating layer thicknesses between the metal and semiconductor at 1.5 ps after dipole emission. Figure (a) is a schematic of the model showing an SiO_2 layer modelled between the Au and GaAs. The thickness, X, is varied and figures b-g show the resulting electric fields for SiO_2 thicknesses of 0 nm, 200 nm, 1 µm, 4 µm, 6 µm and 10 µm respectively. The colour bar is normalised in each case. Figure (h) shows line scans taken from the bottom center of the simulation, indicated by the red square in (a), for SiO_2 thicknesses of 0 nm, 1 µm and 10 µm.

2.4 Effects of metal-dipole distance on emission

To determine experimentally if there are any contributions to emission from the metal-semiconductor contact an insulating layer must be fabricated between the two materials. By doing this the distance between the dipoles formed and the metal will change. As the covered dipole is suppressed due to reflection from the metal, any change in the dipole-metal distance could affect the quenching and therefore the THz emission. The COMSOL model was developed to investigate any effects on emission caused by this change in distance. First a material layer of SiO_2 was inserted between the Au and GaAs zones within the model. Figure 2.10(a) shows an example of this situation. The thickness, X, of the insulating layer was varied from 0 nm (with the layer not present) up to 10 μm, and the results of the emitted electric field for each case are shown in figures 2.10(b-g) respectively. Each image shows the electric field 1.5 ps after dipole emission. For SiO_2 layers under 1 μm thick there is little change in the emitted THz radiation pattern. As the thickness increases above 4 μm effects can be seen in the electric field. Due to the distance between the dipole and the metal being wavelength comparable, the reflection is delayed and so cannot destructively interfere. This leads to a quadrupole-like emission pattern most evident in figures 2.10(f) and (g). The field traveling towards the left of the images is also noticeably different compared to the LPD and quadrupole emission patterns shown in figure 2.9. This is due to refraction of the THz emission through the SiO_2 layer. Figure (h) shows line scans taken at the point indicated by the red square in (a) for thicknesses of 0 nm, 1 µm and 10 µm. For fabrication purposes insulating layers below 1 μm will not cause any detrimental effects to THz emission from the LPD effect. As most metal-semiconductor contact effects are diminished after a few nm this gives a large range from which to select a thickness for fabrication [121].

2.5 Conclusion

In this chapter I have demonstrated through numerical modelling and finite element analysis techniques that THz emission from the LPD effect is driven by suppression of dipoles below a metal mask. I have shown that for an asymmetrical carrier distribution formed within a semiconductor there can be no net current perpendicular to the material surface. Through modelling I demonstrated that a quadrupole emission pattern is produced without a metal mask present and no THz will be detected parallel to the direction of the optical pump beam. With a mask present the dipole formed beneath the metal experiences suppression due to the reflection from the metal gaining a π phase shift. With this dipole quenched the uncovered dipole radiates freely and does so in a direction parallel to the optical pump beam. The understanding gained on the underlying mechanism behind the LPD effect will permit better design of LPD emitters allowing their output to be improved.

Chapter 3

Multiplexing lateral photo-Dember emitters

In the previous chapter I showed, through modelling, the dipole suppression mechanism behind the LPD effect. In this chapter multiplexed lateral photo-Dember emitters are investigated computationally and experimentally. Firstly, I present my model of a multiplexed LPD emitter before characterising single edge LPD emitters and cylindrical lenses. Next, I show the enhanced THz emission for a multiplexed structure illuminated through a cylindrical micro-lens array. I then show the fluence and polarisation characterisation of the multiplexed emitter. These results have been published in [114].

3.1 Introduction

Although LPD emitters show improved output and bandwidth over PD emitters, they still demonstrate lower power than PCAs. As these devices are simple to fabricate – not requiring any complex electrode structures or insulation – and do not suffer from electromigration effects as PCAs do, their use as an alternative emitter could reduce costs for spectroscopy setups and commercial systems. However, in order for this to occur their output must be brought into line with existing commercial PCAs. One way of accomplishing this is by multiplexing LPD emitters to form an array. Multilpex THz emitters can prove difficult to fabricate. Photo-conductive emitters require interlacing finger electrodes to be fabricated on the surface of a semiconductor before being periodically masked by insulating strips. These strips are used to mask alternate positive-negative electrode pairs so that no carriers are excited in these regions [53, 79, 122]. This is necessary so that carriers are excited only in areas with correlating E-field directions to achieve net THz emission. Stringent fabrication processes are also necessary to enusure there is no electrical contact between the interlacing electrodes. Multiplexing of lateral photo-Dember emitters has also proven to be a non-trivial task.

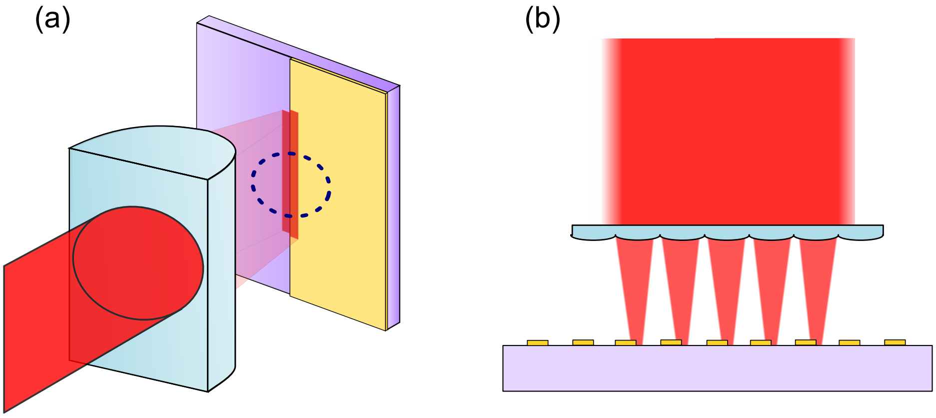

Figure 3.1: In (a) an example of a cylindrical lens focusing the pump beam along the THz generating edge is shown, with the dashed circle representing the spot that would be focused by an achromatic doublet. In (b) the use of a micro-lens array to focus the pump beam on to correlating gold edges of a multiplex LPD emitter is shown.

Work by Klatt *et al.*, involved a two stage metallic deposition procedure which required mounting the emitter at an angle inside the evaporator for the second deposition [79, 106]. Manipulation of the carrier diffussion has also been attempted with various metallic designs patterned onto the surface of the semiconductor [108]. However, many of these designs fail to achieve a net THz field direction, resulting in little or no emission.

In this section I descbribe a multiplex LPD THz emitter consisting of periodic strips of gold deposited onto the surface of a GaAs semiconductor. Multiple correlating gold edges are illuminated by focusing light through a micro-array of cylindrical lenses. The resulting carrier distributions create multiple THz wavefronts which superimpose, resulting in a 5.2 times improvement on the THz SNR obtained from a single emitter illuminated through a single cylindrical lens.

3.2 Modelling multiplex emitters

The drift-diffusion model incorporated with COMSOL, discussed in the previous chapter, was used to study the wavefront propagation and superposition for a miltiplexed LPD emitter design. The design under study consisted of periodic strips of Au deposited on a semiconductor surface. To produce net THz emission photogenerated carriers needed to be produced on only one side of each metal strip, otherwise opposing dipoles from the opposite sides of the metal would destructively interfere. Experimentally this was performed by focusing the optical pump beam using a cylindrical micro-lens array to produce a periodic series of focii. To support the accurate modelling of carrier concentrations by the drift-diffusion model the $1/e^2$ radius of the optical pump beam was set equal to the focal spot size produced by the micro-lenses. This spot size was found by modelling the micro-lens arrays with COMSOLs ‘Frequency Domain’ module,

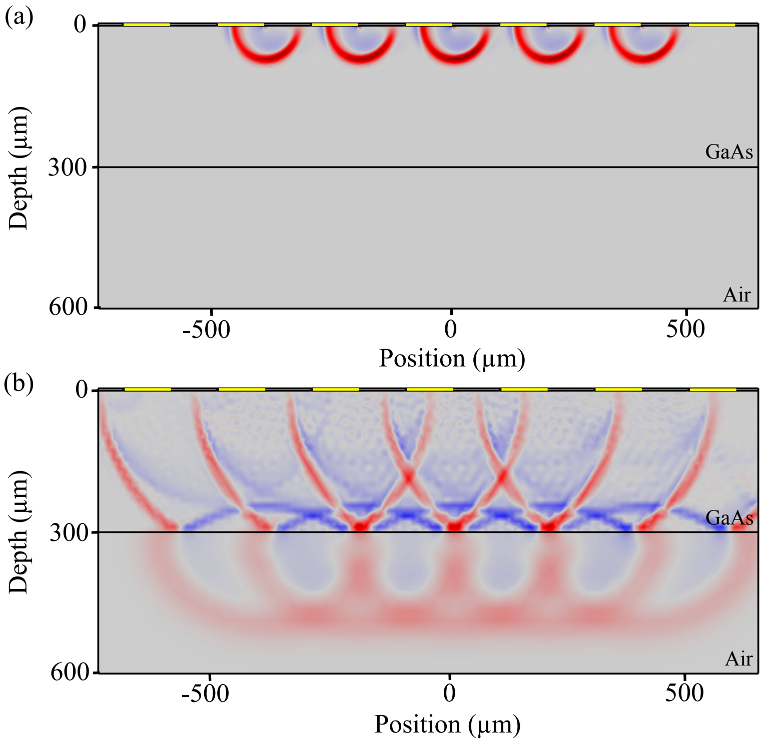

Figure 3.2: Model of the dynamic electric field (z-axis) produced by multiple asymmetric carrier distributions in GaAs; red is positive field and blue is negative field. In (a) the field is viewed 1.4 ps after initial dipole emission. In (b) the field is viewed 4.85 ps after initial dipole emission. The wavefronts constructively superimpose to form a single, planar THz wave.

results which are discussed later in section 3.5. This also provided an estimate of the focal length for all the lenses that were used in our experiments. The results of the drift-diffusion model were incorporated into a COMSOL Multiphysics simulation with geometry based on the multiplex emitter design discussed previously. The period of the Au strips was limited by the period of the micro-lens arrays commercially available. Lens arrays of 15 µm and 200 µm period were obtained and the model was based upon an emitter designed for use with the 200 µm array. $100\,\mu$m wide Au strips with a period of $200\,\mu$m were modelled on the surface of a $300\,\mu$m thick GaAs substrate. Air was included between the Au strips and a further $300\,\mu$m air layer was modelled underneath the GaAs to monitor the propagation of THz after leaving the substrate. Multiple lateral wires were modelled $1\,\mu$m below the semiconductor surface near to each metal strip as in figure 2.8 and the current results from Matlab were imported to each wire. The simulation was again run using the 'Transient Electromagnetic Waves' module to analyse the field evolution and propagation over time. The results from this model are shown in figure 3.2, where (a) shows the field 1.4 ps after dipole emission and (b) shows the field 4.85 ps after emission. As shown in (a), each dipole emits a THz pulse in accordance with the LPD effect. As each individual wavefront propagates through the semiconductor it undergoes superposition with neighbouring wavefronts. As shown in (b), after emerging from the semiconductor the wavefronts resemble one single plane wave. These results support the notion of a multiple emitter array producing constructive THz emission and the plane wave nature of the emission was observed experimentally as the parabolic mirrors of the setup could be coarsly adjusted without greatly affecting the detected THz amplitude. For a wide illumination producing multiple wavefronts, the use of a Si-lens would prove detrimental to measurements. This is due to the fact that only emission at the center of the Si-lens would be correctly steered by it onto the parabolic mirror. Wavefronts further towards the edges of the lens would not be effectively collected by the parabolic and would produce multiple peaks in the TDS scan. This was also observed experimentally as with an Si-lens in place no single THz pulse could be observed in the time-domain. For multiplex emitters illuminated with a large pump spot, no Si-lens should be used. However, if the pump beam is focused to a smaller spot size a lens could still prove beneficial.

3.3 Experimental investigation of cylindrical lenses

The multiplex emitters utilise a cylindrical micro-lens array to focus the incoming pump beam. To draw a direct comparison between a single and a multiplexed LPD emitter, a single cylindrical lens was used to investigate the effect of such a focusing mechanism on the THz generated from a single edge emitter. Theoretically, focusing the pump beam onto a single gold edge through a cylindrical lens would produce a greater THz emission for a given pump beam power than if a regular achromatic doublet objective were used. THz radiation is generated primarily along the metal/semiconductor edge. The cylindrical lens would focus the power that would usually be ‘wasted’ across the metal and semiconductor along a spot size length of the THz generating edge region (figure 3.1a). This would result in a larger length of the metallic edge being illuminated and higher fluences would be reached for lower laser powers, improving efficiency.

A 100 nm layer of Au was evaporated onto a piece of LT-GaAs to mask half of the semiconductor. A 5 nm layer of Cr between the Au and semiconductor was used as an adhesion layer. The resulting single-edge LPD emitter was then mounted in a typical transmission THz-TDS set up similar to the set up shown in figure 1.2. However, as LPD emitters do not require an electrical bias an optical chopper was used to modulate the pump beam in order to produce a signal for the lock-in amplifier to reference. The emitter was aligned with a Si-lens to increase the acceptance angle on to the first parabolic mirror. A Menlo systems PC LT-GaAs antenna aligned with a second Si-lens was connected to a lock-in amplifier for use as the detector in this system. A 100 fs, 80 MHz Ti:Sapphire laser centred at 800 nm, and with a $1/e^2$ spot size of 0.61 mm, was modulated by an optical chopper and focused onto the emitter surface by both an achromatic doublet and cylindrical lens in turn. The focal spot size on the emitter surface was initially adjusted to achieve the maximum THz amplitude possible and time-domain scans were taken for

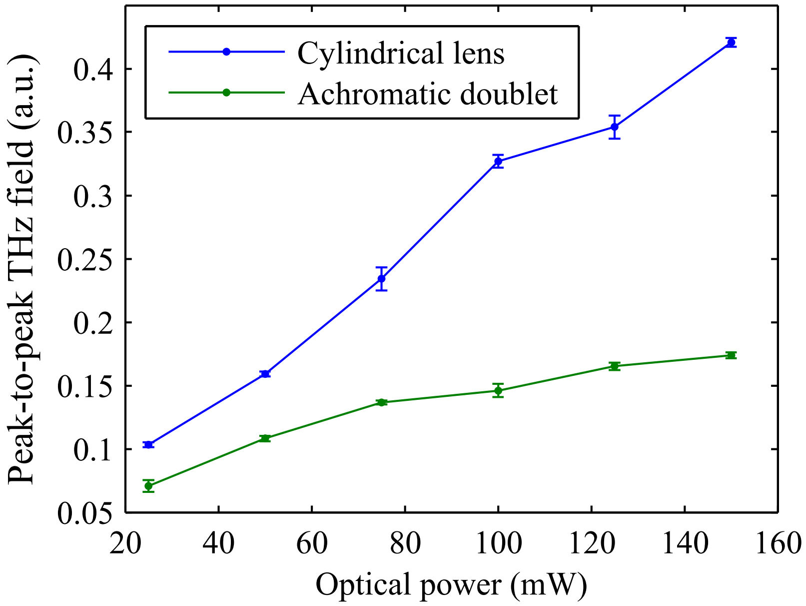

Figure 3.3: A comparison of the peak-to-peak THz field achieved for a given pump power for a single cylindrical lens (blue line) and an achromatic doublet lens (green line). Over double the THz field is achieved on average with a cylindrical lens over an achromatic doublet for a given pump power due to the increased fluence. The error bars represent the standard deviation from multiple TDS scans.

different incident optical powers, with the detector illumination power held at a constant 5 mW. Multiple TDS scans were taken for each case and the standard deviations are plotted as error bars. The results for both the achromatic doublet and the cylindrical lens are shown in figure 3.3. There is a clear improvement of emitted peak-to-peak THz field for the cylindrical lens, with it achieving an average of double the output of the achromatic doublet over the 20 to 150 mW range of pump powers. It must be noted that the pump spot sizes were optimised for maximum THz generation and the cylindrical lens has a distinct advantage over the doublet, as it naturally illuminates a larger length of the metal-semiconductor edge with increased fluence for a given input power. Overall this shows improved efficiency in the conversion of infrared pump to THz signal when using a cylindrical lens.

3.4 Experimental investigation of multiplexed emitters

Two multiplex emitter arrays of different period and strip width to match the micro-lens arrays were fabricated through photolithography. One comprised of 100 μm wide Au strips with a period of 200 μm on SI-GaAs and the other of 7 μm wide Au strips with a period of 15 μm on LT-GaAs. The Au was deposited on both emitters to a thickness of 100 nm with an 5 nm Cr adhesion layer between the Au and semiconductor. SI-GaAs was chosen as the first substrate due to its high dark resistivity, whereas LT-GaAs was chosen

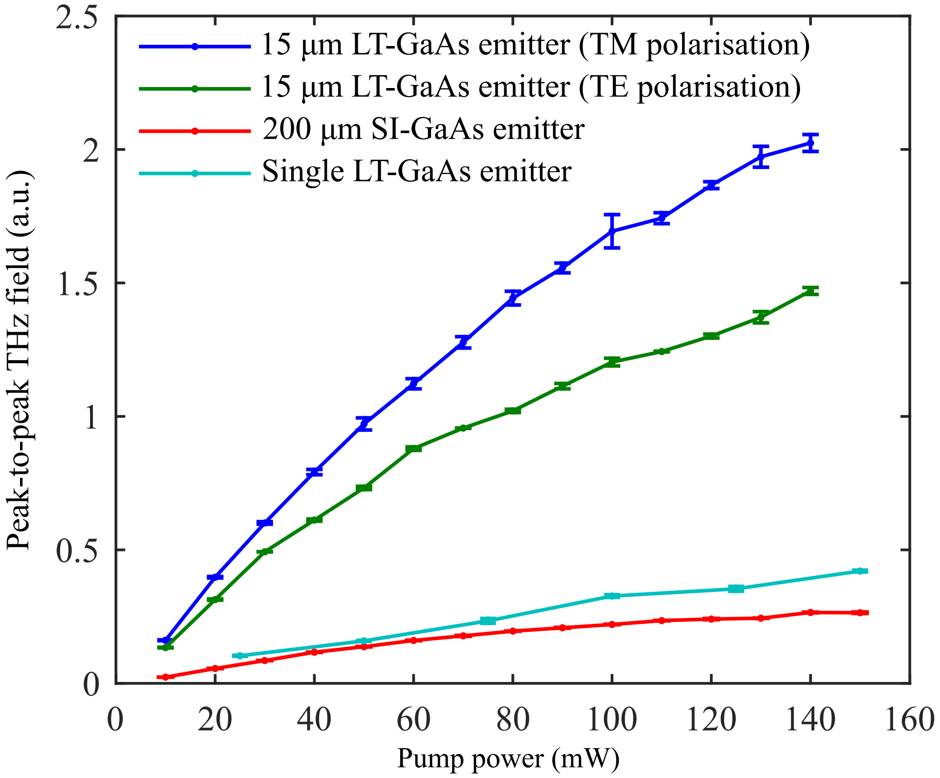

Figure 3.4: Graph of peak-to-peak THz field as a function of optical pump power for three different emitters. The blue and green lines represent the 15 μm period LT-GaAs emitter illuminated with TM and TE polarisation respectively. The red line represents the 200 μm SI-GaAs emitter, and the turquoise line represents the single edge LT-GaAs emitter illuminated through a single cylindrical lens. The error bars represent the standard deviation from multiple TDS scans.

due to its sub-picosecond carrier lifetime, a trait which sees it used in many commercial photoconductive antennas. Each emitter in turn was mounted in the transmission THz-TDS set up described previously. A Si-lens was not included on the emitter arm of the set up as this would disturb the superposition of the emerging THz wavefronts. The pump beam was directed through a cylindrical micro-lens array of period equal to that of the emitter used and on to the emitter surface. The multiple foci produced by the lens array were aligned against correlating gold edges on the emitter, which was positioned at the focal distance from the lens. This was required since, if the emitter surface were simply illuminated without the lens array, opposing gold edges would produce opposing dipoles which would suffer destructive superposition resulting in no net THz radiation in the desired direction. The THz emission of both multiplex emitter arrays was measured as a function of incident optical power from 10 to 150 mW, with the detector illumination power held at a constant 5 mW. The measurements for the 15 μm period emitter were repeated for two different polarisations of incident illumination; Parallel to the edges of the gold strips (TE polarisation) and perpendicular to the edges of the gold strips (TM polarisation). All these results are shown in figure 3.4.

The results show that the 15 μm period multiple emitter exhibits a greater increase

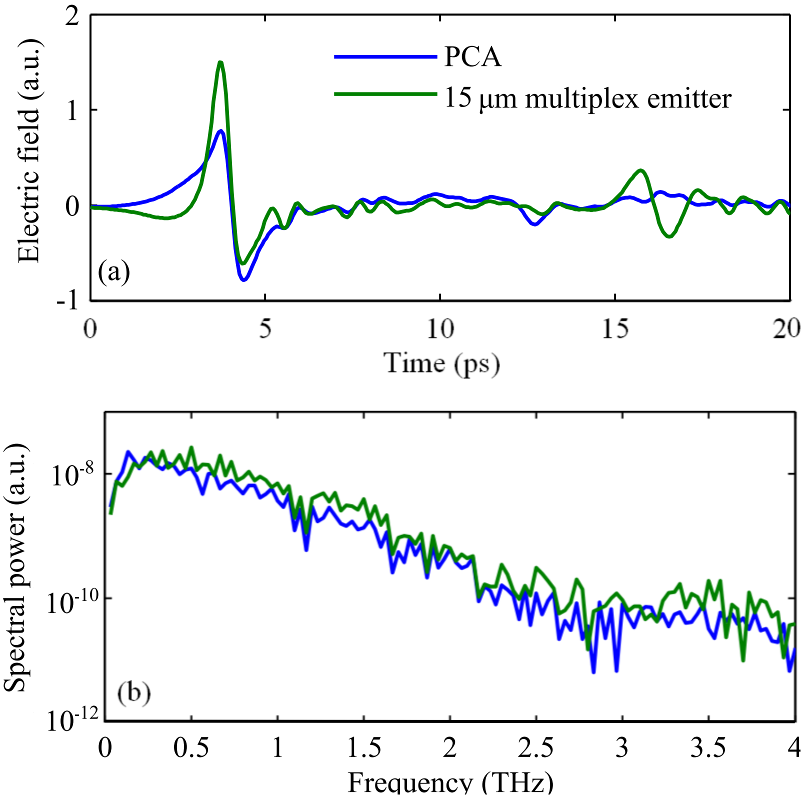

Figure 3.5: Plots showing the time-domain scans and respective Fourier transforms for the 15 μm period LT-GaAs multiplex emitter (green line) and a commercial Menlo Systems PC antenna (blue line).

in peak-to-peak field of emitted THz radiation in comparison with the 200 μm period array and with the single emitter illuminated by a single cylindrical lens. In this case the single emitter with cylindrical lens shows improved emission over the 200 μm period emitter. This is most likely due to the 200 μm period array being fabricated on SI-GaAs, which shows a lower saturation fluence in comparison to LT-GaAs, significantly reducing its output [115, 123]. The presence of the Si-lens for focusing the THz produced by the single emitter would also make direct comparisons between the two emitters difficult. It was also found that incident light polarised perpendicular to the gold edges (TM) produces a significant increase in emitted field when compared with polarisation parallel to the edges (TE) for multiple emitters. This has been shown to occur for both LPD and PC emitters and is due to field enhancement at the metallic edge [124, 125]. The output fields for the 15 μm period emitter and single emitter from figure 3.4 were compared. The average output field increase for the multiple emitters over single emitter at these illuminations was found to be 5.2. This shows the multiple emitters to emit over 5 times greater THz field – over 25 times greater power – than a single LPD emitter despite the presence of the Si-lens allowing a larger acceptance angle for the single emitter. This increase in signal did not constitute a simultaneous increase in noise, allowing an equivalent increase in SNR. It was also noted that with the multiplex emitters in place the parabolic mirrors could be more coarsely adjusted without affecting the THz signal compared to when a single emitter was in place. This supports the computational results in the previous chapter which showed a THz plane wave forming from the superposition of multiple wavefronts. It is feasible to improve this result by focusing to a wider spot and increasing the total optical power, however this was unachievable due to the power available from our laser setup.

To compare the output of a multiplex LPD emitter with a PC antenna, scans were made with the 15 μm period LT-GaAs multiplex emitter illuminated with 100 mW of power and the detector illuminated with 5 mW power. This emitter was then replaced with a Menlo systems PC antenna which was aligned with a hyper-hemispherical Si-lens. Time domain scans were taken with the emitter biased at 5 V and both detector and emitter optical powers at 5 mW. Figure 3.5 shows the time-domain scans and frequency spectra of this. The multiplex emitter shows comparable bandwidth to a PC antenna in our setup, spanning ~3 THz before becoming indistinguishable from the noise floor. A power comparison between the two devices cannot be made due to the freedom in choice of the applied bias in the PC antenna. However, increasing the bias of a PCA can also increase the noise floor due to the electric fields involved, leading to little change in SNR. For multiplex LPD emitters the SNR increases with the optical power due to the absence electrical noise. If the maximum voltage is chosen then the PC antenna would be more powerful, but this would considerably decrease its lifetime due to electrical damage and electromigration of metals [104].

3.5 Fluence calculations for multiplexed emitters

Typically with a single emitter the THz emission will eventually saturate at a certain fluence, determined by the pump beam power and spot size. To calculate the fluence for the multiplex emitters several assumptions must first be made. If the pump beam is a typical gaussian we know that there is less power present the further from the center of the beam we are. The micro-lens array produces many focii. A micro-lens located near the center of the gaussian pump beam will focus a greater optical power than a micro-lens located nearer to the edge of the beam. We can assume the multiplex LPD emitter to consist of many individual emitters. As such we can assume the individual emitter illuminated by the central focus will reach saturation before the individual emitters further from the center. This unique product of using a lens array means that overall the multiplex emitter will reach saturation more gradually and at a slightly higher overall fluence than a single emitter. To calculate the fluence incident on a multiplex emitter the following technique was used.

A three dimensional gaussian beam was modelled based on the 1/e^2 spot radius of the laser beam. The number of foci produced by each micro-lens array that fell within the laser spot was calculated. This allowed an estimate of the number of gold strips

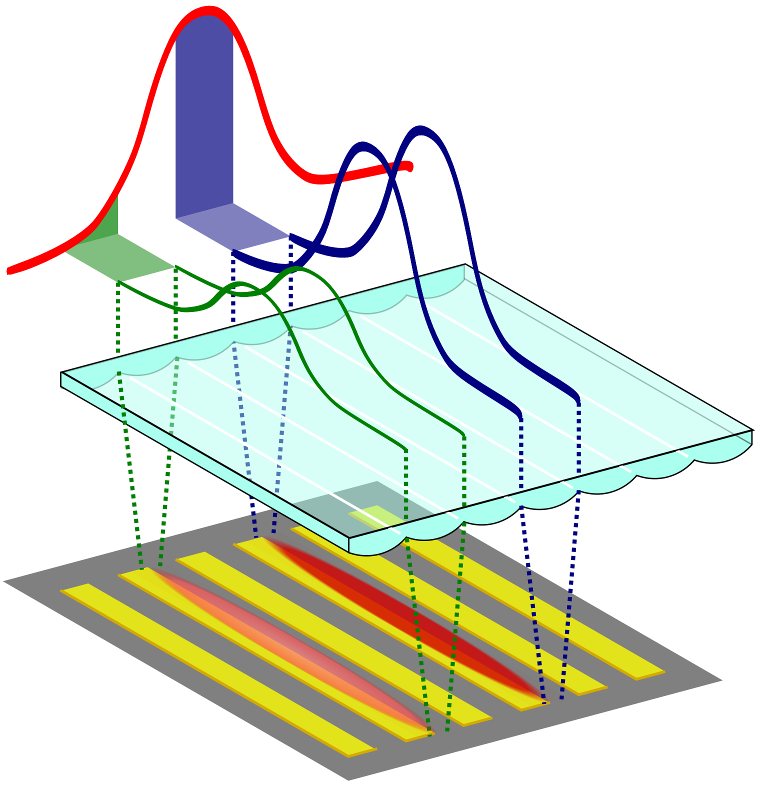

Figure 3.6: A demonstration of the technique used for fluence calculation. The percentage of power of the gaussian beam focused by each micro-lens is calculated using the pump beam spot size and number of micro-lenses that are illuminated. The spot size produced by the micro-lenses is found through COMSOL simulation and coupled with percentage power to produce an estimate of the total fluence.

illuminated on each array; a total of 7 and 82 strips for the 200 μm and 15 μm period arrays respectively. The percentage of the total gaussian beam power that would be focused by each micro-lens in each array was then calculated (Illustrated in figure 3.6). The spot size produced by each micro-lens was calculated using the formula $d_0 = 4f\lambda/\pi D$, where d_0 is the 1/e focal spot diameter, f is the focal length of the micro-lens, λ is the wavelength and D is the diameter of the input beam. Specifications from the lens array suppliers were used, with f=1.6 mm and D=200 μm for the 200 μm array and f=16.4 μm and D=15 μm for the 15 μm array. The results gave a 1/e focal spot diameter of 8.15 μm and 1.11 μm for the 200 and 15 μm lens arrays respectively. To support these results a single lens from the 15 μm array was modelled using COMSOL Multiphysics to find an estimate for the focal spot size produced. The dimensions of an individual micro-lens were taken from the specifications supplied by the producer (Jenoptik Inc.) and recreated within a frequency domain COMSOL model. The lens material was set as SiO_2, the surrounding material as air and an input wavelength of 800 nm was used. Figure 3.7 (a) shows the electric field results for the 15 μm period lens array. A focus is formed approximately 15 μm from the center of the micro-lens. This distance is comparable to the focal length of 16.4 μm quoted by the suppliers, assuming this is correct for 800 nm

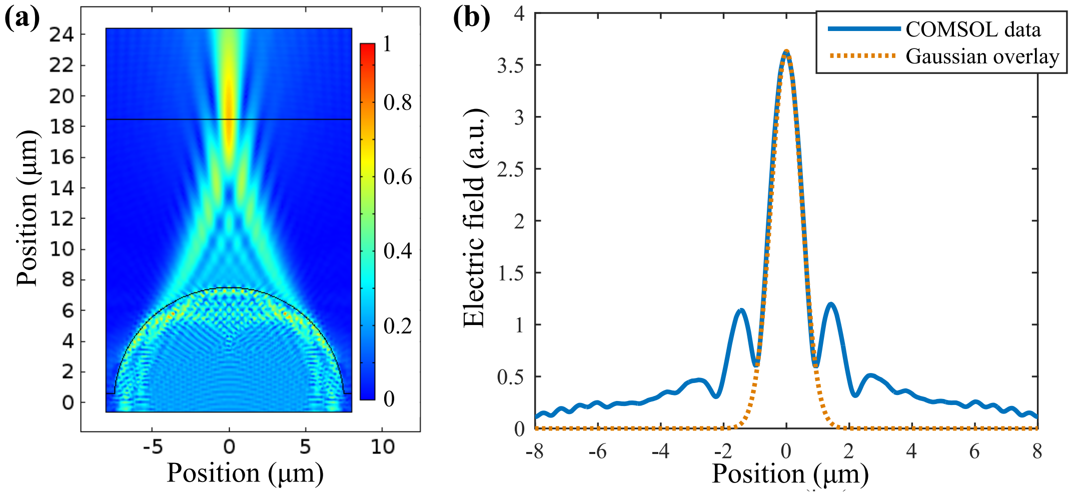

Figure 3.7: Figure (a) shows the electric field results for a single lens from the $15\,\mu$m array focusing 800 nm wavelength light. The blue line in figure (b) shows the intensity profile measured across the horizontal line at y = $18.5\,\mu$m in (a). This also includes the diffraction effects generated in the COMSOL model. The orange line is an estimate of the spot profile without diffraction effects. The 1/e spot diameter for these plots is $1.38\,\mu$m.

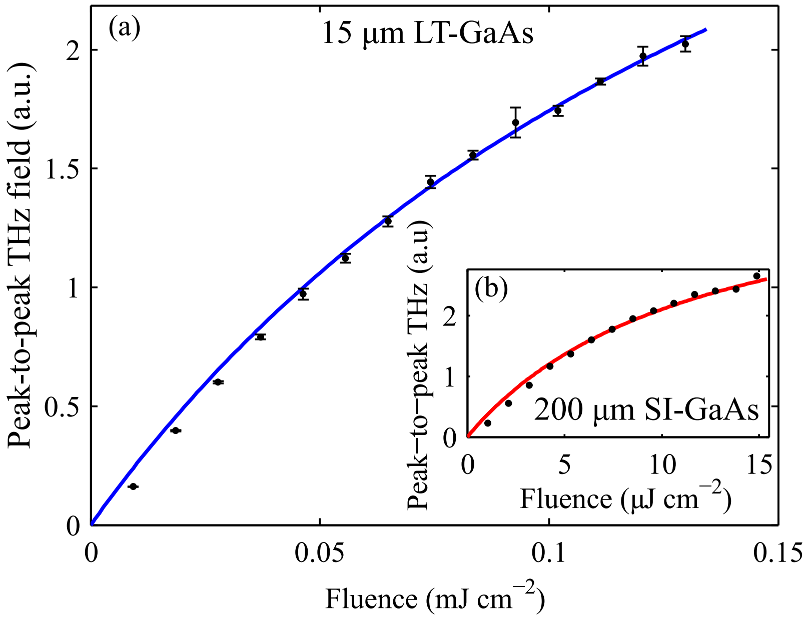

Figure 3.8: (a) and (b) show the peak-to-peak amplitude of the detected THz as a function of fluence for the $15\,\mu$m period LT-GaAs multiplex emitter and the $200\,\mu$m period SI-GaAs emitter respectively. The solid lines represent saturation curve fits, with the average saturation fluence for LT-GaAs found to be $F_{\text{sat}} = 0.18$ mJ cm^{-2}, and for SI-GaAs $F_{\text{sat}} = 12\ \mu$J cm^{-2}.

light. Figure 3.7 (b) shows the electric field profile simulated along the horizontal line at y = 18.5 μm in (a). There are clear effects from diffraction in (b) so a gaussian function was overlaid to negate this. The estimate for 1/e focal spot diameter for the 15 μm micro-lens array produced by COMSOL is 1.38 μm, a value comparable to that previously calculated. The percentage power focused by each microlens coupled with the spot size produced allowed the total fluence to be calculated.

Figure 3.8(a) shows the peak-to-peak THz power plotted as a function of fluence for the 15 μm period multiplex emitter, with the inset (b) showing the same for the 200 μm period emitter. The curve fits the saturation formula $E_{\mathrm{THz}}(F) = A\omega \sum_{i=1}^{n} F_{\mathrm{i}}/(F_{\mathrm{i}} + F_{\mathrm{sat}})$, where A is a coefficient of conversion and alignment efficiency, ω is the 1/e^2 pump spot radius and F_{sat} is the saturation fluence. For the summation; n is dependent on the number of focii produced by the micro-lens array, and F_{i} is the fluence produced at each focus. The average saturation fluence for LT-GaAs was found to be $F_{\mathrm{sat}} = 0.18$ mJ cm^{-2}, and for SI-GaAs $F_{\mathrm{sat}} = 12$ μJ cm^{-2}, which are consistent with similar work on single edge LPD emitters [110, 115]. These results show this method of determining fluence for multiple-focus producing lenses to be accurate and reliable.

3.6 Conclusion

In this chapter I have demonstrated the operation of a multiplexed LPD emitter both computationally and experimentally. A multiplex LPD emitter coupled with a cylindrical micro-lens array exhibits over five-times THz field enhancement compared to a single edge emitter illuminated through a single cylindrical lens. The multiplex emitter exhibits bandwidth and SNR comparable to that of a PC antenna and its output offers further opportunity for improvement by creating a smaller period array or by illuminating a larger area of the emitter surface. I have shown through simulation that the superposition of multiple THz wavefronts lead to a single, enhanced THz pulse which is supported by my experimental findings. The results agree with previous work which show LT-GaAs to exhibit a higher saturation fluence - and therefore higher THz emission - than SI-GaAs. I have also demonstrated a simple method for calculating the fluence for multiplex emitters coupled with lens arrays, which produced saturation fluence values consistent with other work.

These multiplex emitters are simple to fabricate and highly durable, as they do not require an external bias which can decrease the lifetime of PCAs. Alignment of the micro-lens array can however prove time consuming. In the following chapter I describe a novel multiplex emitter design which does away with the need for a focusing element.

Chapter 4

Double-metal emitters

In the previous chapter I showed through simulation and experiment that by multiplexing a LPD emitter we can achieve an enhancement of over five times the THz output when compared with a single edge LPD emitter. The design utilised parallel metal strips fabricated on the surface of a semiconductor. The device needed to be illuminated through a cylidrical micro-lens array. This was required so that the pump beam could be focused only along correlating gold edges to generate a net dipole direction and result in observable THz emission. Alignment with the micro-lens array can prove difficult and time consuming, as the focus and position of the array must be adjusted to coincinde with the edges of the metal strips. A separate lens array must also be purchased for each emitter created with a different period of striplines. These points conspire to make this emitter design less than desirable.

In this chapter I describe the development of a bias-free, Schottky-enhanced, double-metal emitter. These devices utilise two different overlapping metals to achieve net THz emission through selection of each metals' skin depth and work function. I explore the theory of operation of these emitters, describing both the LPD and Schottky components of THz emission, as well as the fabrication process. I present my comparison of different metal combinations and characterise the devices at different temperatures, fluences and polarisations. The work presented here was in conjunction with Duncan McBryde and Sam Berry, and has been published in [116, 117].

4.1 Introduction

Multiplexed PCA's were introduced in 2005 by Dreyhaupt *et al* [122]. An example of such a device is shown in figure 4.1. The multiplexed PCA consists of an interdigitated array of electrodes fabricated on to the surface of a semiconductor. A bias is applied across the array and every second electrode pair is masked to ensure carriers are only

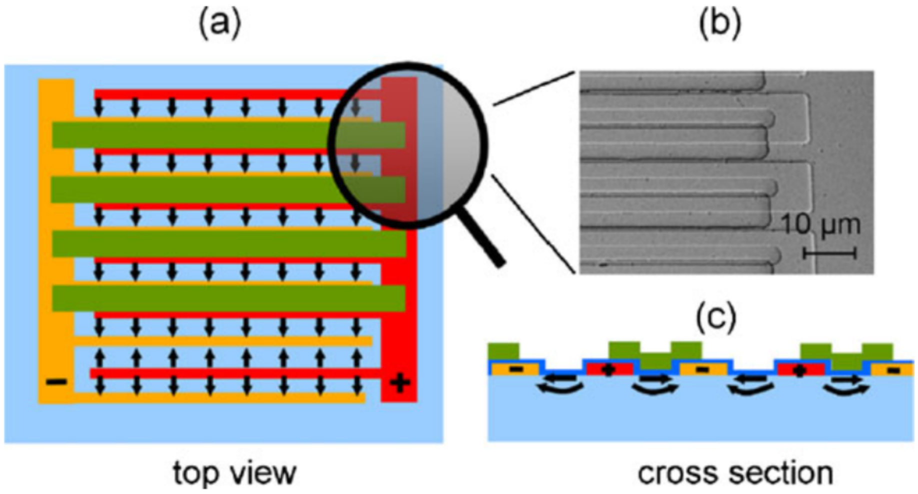

Figure 4.1: (a) shows a top view diagram of the multiplexed PCA design, (c) shows a cross section and (b) is an SEM image of a fabricated device. The yellow and red parts indicate electrodes of opposite bias, the arrows indicate the direction of the electric fields. The green areas show the masking of every second electrode pair to ensure carriers are only photogenerated in regions of correlating field direction. Image used from [53].

photoexcited in regions of correlating electric field direction. Carriers are then accelerated in the same direction to produce a net current and THz emission. This design allows multiplexed PCA's to be operated without the need for optics to focus the pump beam on to the emitter surface. These antenna are now commercially available from companies such as Laser Quantum Ltd and are opening the door to simpler, less alignment-sensitive setups for THz-TDS. However, these antennae still require an electrical bias to operate, reducing their lifetime and their simplicity. Any damage or electrical shorts in one area of the antenna can also render the device unusable.

Klatt *et al.*, developed a multiplexed LPD emitter which did not need focusing optics for the pump beam [106]. Their device was fabricated by depositing wedge-shaped metallic striplines on to the surface of a semiconductor. This was achieved by patterning striplines of aluminium 'walls' onto the semiconductor before depositing gold at an angle to form the wedge shaped structures. Figure 4.2(a) shows the intended wedge design and inferred carrier density formed. Figure 4.2(b) shows an image of the fabricated emitter, which resembles a step-shaped structure instead of the intended wedge. Later fabrications of these devices replaced the Al walls with photoresist to ease the fabrication process. These multiplexed wedge emitters demonstrated good THz emission, however, the LPD process was misinterpreted by Klatt *et al.*. They believed the asymmetrical diffusion currents created at the gold edges would cause stronger dipole emission from underneath the thick part of the gold. Research in our group, which I discussed in *Chapter 2*, was able to disprove this interpretation of the LPD effect and introduce the new concept of dipole suppression [109, 110, 113]. This mechanism suggested that the emission Klatt *et al.*, were seeing from their wedge emitters was, in fact, due to the thin sections of gold

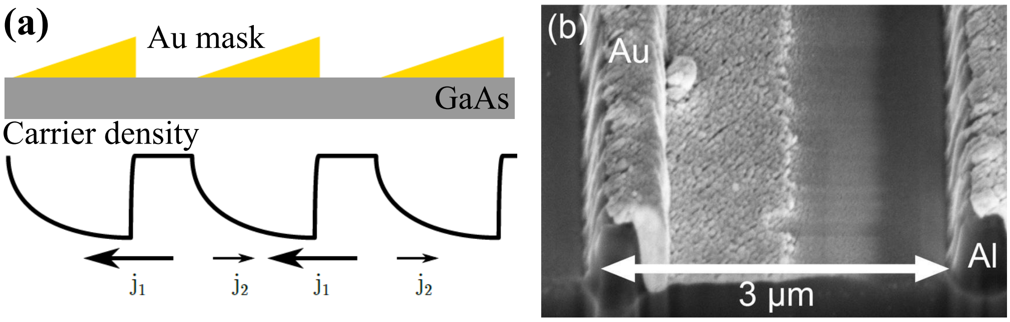

Figure 4.2: (a) shows a diagram of the intended wedge shaped emitters and the supposed carrier density predicted by Klatt. (b) shows a SEM image showing the multiplexed emitters fabricated by Klatt *et al.* Thin walls of Al (later photoresist) are deposited on the GaAs surface. Au is evaporated at an angle to create a set of thin wedges. The gold does not show linear variation of thickness and also exhibits signs of percolation. Image used from [106] and is the same as figure 1.11, replicated here for ease.

being of thickness below the skin depth of the generated THz. This would mean that the dipole formed under this area would not be completely suppressed, allowing it to radiate. The theory is explored further in the following section.

4.2 Design principles of double-metal emitters

The double-metal (DM) LPD emitters utilise two different metals to achieve a net dipole direction within the semiconductor allowing for THz emission. The metals are chosen for their skin depth in both the THz and the infrared region to engineer the LPD effect to produce a net dipole emission direction. By using two metals with differing work functions we can also engineer a built in Schottky field to further aid and enhance our THz emission.

4.2.1 Lateral photo-Dember contribution

The theory of dipole suppression in the LPD effect states that THz reflected from the metal surface gains a π phase shift, quenching the dipole formed under the metal. By changing the reflectivity of the metal mask it is possible to control how much of the THz is reflected, and therefore how much quenching that dipole experiences. By using two metals with different reflectivities it would be possible to engineer an emitter with a net dipole direction and no need for a focusing lens.

Figure 4.3 shows an example of a DM emitter. Two metals of different reflectivities are fabricated in strips next to, and partially overlapping each other. An ideal pairing of metals would involve both of them being opaque to the infrared pump beam, so that LPD dipoles are formed at each metal edge. In the case of a repeating double-metal element the dipoles formed outside of the metal mask would oppose each other and cancel out. The dipole formed under the high reflectivity metal would experience full quenching, as the THz reflected from the metal would gain a π phase shift and interfere. Less THz would be reflected by the low reflectivity metal, meaning that the dipole formed underneath would only be partially quenched. In DM emitters it is this dipole formed underneath the low reflectivity metal that is the primary THz source. By repeating this double-metal element an emitter would be created with a net dipole direction without the requirement for any focusing optics. This emitter would also not require any tricky angular deposition methods as used by Klatt *et al.*, to create their wedge emitters.

The reflectivity of the metals is dependent on their skin depths. This is the depth to which eddy currents form within the material from interaction with electromagnetic waves. For thicknesses of metal above the skin depth interaction will be significant, therefore by varying the thickness of the metal we can affect how much of the THz will interact and be reflected. This explains why the wedge emitters developed by Klatt *et al.*, were able to function effectively, as the thin side of the gold would have been below the skin depth at THz frequencie whilst the thick side remained above the skin depth. The skin depth of a metal is described by the relation;

$$\delta = \sqrt{\frac{2\rho}{(2\pi f) \times (\mu_{\mathrm{e}}\mu_{\mathrm{r}})}} \approx 503 \times \sqrt{\frac{\rho}{(\mu_{\mathrm{r}} f)}} \tag{4.1}$$

where ρ is the resistivity of the metal, μ_{r} is the relative permeability of the metal, μ_{e} is the relative permeability of free space and f is the frequency of the incident electromagnetic radiation [126]. Figure 4.4 shows the skin depths (δ) of different metals in the 0.5-4 THz range. From the figure we note that the skin depths of gold and aluminium are very

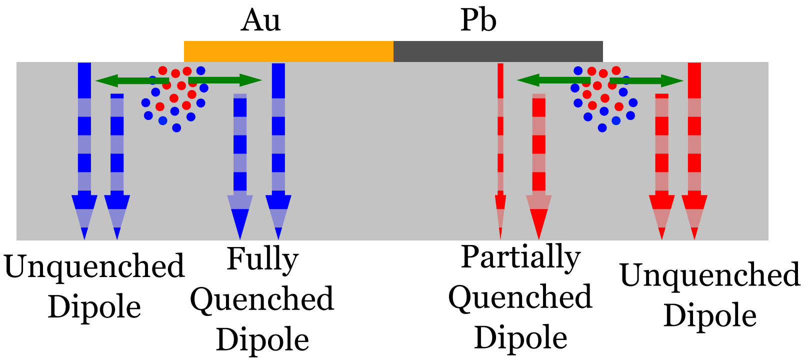

Figure 4.3: A diagram showing the emission mechanism for the double-metal emitter due to the lateral photo-Dember effect. Carrier diffusion creates radiative dipoles near the metal boundaries, shown as green arrows. Each set of dipoles created on the boundary points have equal magnitude. Dipoles created under the metal surface are quenched by reflection from the surface and are suppressed. The difference in the reflectivity between the two metals causes net terahertz emission to be observed.

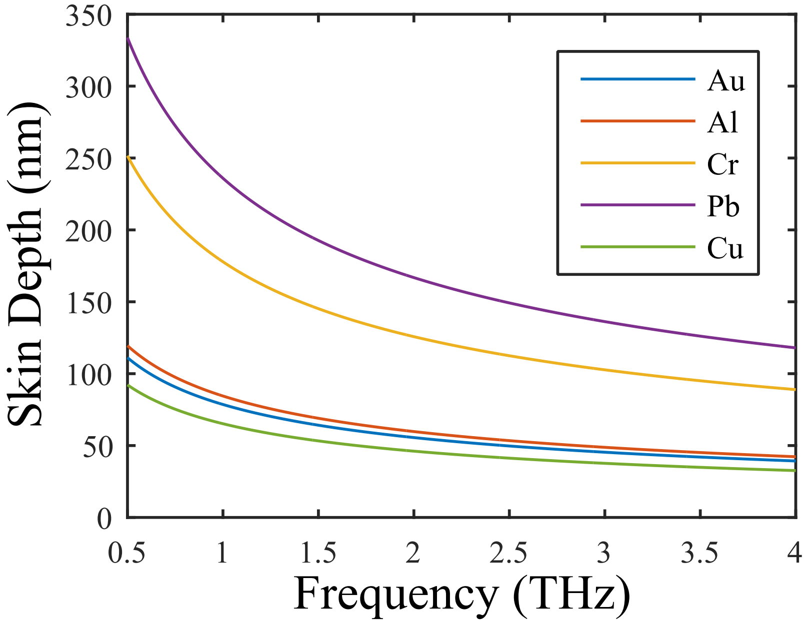

Figure 4.4: A plot of the skin depth of different metals against THz frequencies. Due to the large difference in skin depth in comparison to Au, Pb was selected as an ideal candidate for these emitters.

similar at THz frequencies. As this metal pairing was the first used by Klatt *et al.*, for their wedge emitters it demonstrates how the thicknesses of the metals play an important role.

Due to the large difference in skin depth in comparison to Au, Pb was selected as an ideal candidate for these emitters. The transparency of Pb was tested experimentally in a transmission THz-TDS setup to confirm the thicknesses required for fabrication. Pb was thermally evaporated onto glass microscope slides which were placed into a THz beam and the transmission of the THz was monitored. Pb layers below 24 nm in thickness are transparent at 1 THz [127] and we found that Pb layers of up to 80 nm thickness allow transmission across a spectral range of 2 THz, whilst completely blocking the 800 nm optical pump beam.

4.2.2 Schottky contribution

By using two different metals it is possible to engineer the Schottky effect to aid the LPD effect in producing THz. In a semiconductor the conduction and valence bands bend close to the surface, pinning the Fermi level and forming a depletion region [74]. This band bending has been shown to cause THz emission and can influence LPD emitters [74, 115]. It has also been shown to affect the polarity of THz emission under exposure to intense optical fluences [115, 128]. The bending of the bands near the surface can be influenced by applying a metal to the surface. Figure 4.5 shows the band diagram for a DM emitter consisting of Au and Pb patterned on GaAs. The metals have different

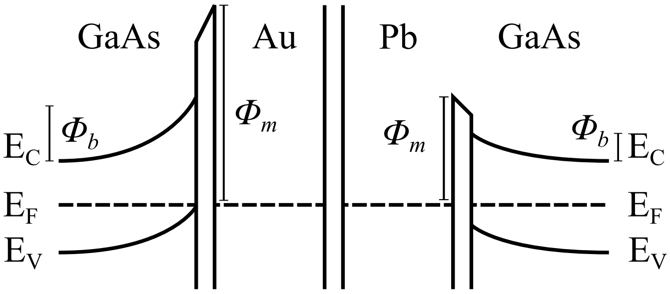

Figure 4.5: A band diagram for the Au/Pb emitter. Both Au and Pb create a Schottky barrier near the metal/semiconductor interface. The two metals have different work functions, ϕ_m, which create different barrier heights, ϕ_b. Band bending occurs near the metals causing currents related to the barrier heights, j_{Au} and j_{Pb}. If $j_{Au} \neq j_{Pb}$ a net current is generated resulting in terahertz emission.

work functions (ϕ_m) which cause a difference in Schottky barrier heights on each side of the double-metal strip. The barrier height difference leads to a difference in the band bending at the semiconductor surface (ϕ_b) creating transient lateral currents near to the metal/semiconductor boundaries. If the work functions of the metals are the same then the Schottky barrier heights, and therefore the lateral currents generated, are the same and will therefore cancel. For the metals demonstrated in figure 4.5 Au has a barrier height of around 0.9 eV [129, 130] and Pb a height of 0.8 eV [131] at 300 K when bonded with GaAs. This difference will produce a net lateral current which can aid the diffusion of carriers and contribute to the THz emission. It should be noted, however, that the barrier height is highly dependent on the surface quality of the semiconductor, with surface passivated devices showing stronger emission than devices with an oxide layer [132]. It has been shown that plasmonic effects from metals deposited on semiconductors can also enhance the THz emission from these devices through enhanced pump beam absorption and increased numbers of excited carriers [133, 134]. The use of metals with different plasma frequencies may also encourage differences in pump beam absorption either side of the double-metal strips, leading to further enhancement of the THz emission.

4.3 Fabrication

The fabrication of DM emitters was carried out by Duncan McBryde, Sam Berry and myself. DM emitters were fabricated using a two stage photolithography method. The substrate was prepared by immersion in acetone and IPA before being rinsed in DI water and baked in an oven at 90 °C for 30 minutes. This was to ensure a clean substrate surface for good results. S1813 positive photoresist was spun to a thickness of ~1 μm on the substrate surface and then baked on a hotplate at 90 °C for a further 2 minutes. The prepared substrate was aligned with a mask designed for standard photolithography and UV exposed, then developed. The first metal was deposited through thermal deposition

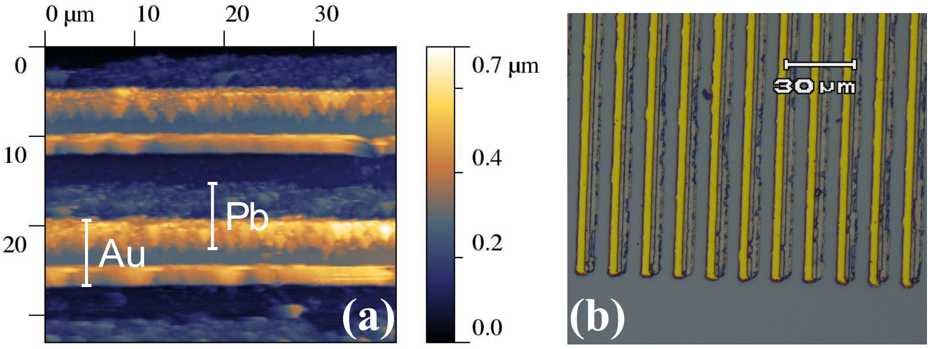

Figure 4.6: Images of the DM emitters after fabrication. In (a) an AFM image of an Au/Pb emitter is shown where an overlap of metals can be clearly seen. In (b) an image taken from an optical microscope is shown.

and the remaining photoresist and excess metal was removed by immersion in acetone. This left a pattern of 4 µm wide metal strips with a period of 15 µm on the surface of the substrate.

The process was repeated and the mask was positioned for the second strip pattern by optically aligning it with the already deposited metal strips to ensure an overlap in the strip pattern. After exposure, deposition and lift off the resulting DM emitter was cleaned and observed under an optical microscope. Figure 4.6(a) shows an SEM image of a Au/Pb emitter with a 2 µm overlap between the metals, while (b) shows an optical mocroscope image of the completed emitter. For initial tests emitters were created on SI-GaAs. Pb was deposited to a desired thickness of 60 nm and Au was deposited to a desired thickness of 100 nm with a 3 µm Cr adhesion layer. However, due to a detector error around 200 nm of Au and 120 nm of Pb were deposited in this initial run. The thickness of the deposited Pb was still below the expected THz skin depth so the dipole underneath would not experience complete suppression. Another Au/Pb emitter was fabricated on LT-GaAs to test for a difference in emission as observed with single LPD emitters and the multiplexed emitters described in the previous chapter.

To characterise the relative strengths of the LPD effect and the Schottky effect, DM emitters were fabricated on a SI-GaAs substrate with a 100 nm insulating SiO_2 layer. This insulating layer was used to eliminate the band bending caused by the metal, which can be eliminated by just a few nm of insulation [121]. This created a DM emitter which functioned solely due to the LPD effect with no Schottky influence.

4.4 Characterisation

All of the fabricated DM emitters were characterised in a standard THz-TDS setup pumped by an 80 MHz, 100 fs Ti:Sapphire laser centered around 800 nm. A Menlo Tera-8 photoconductive antenna aligned with a silicon lens was used as a receiver. For all

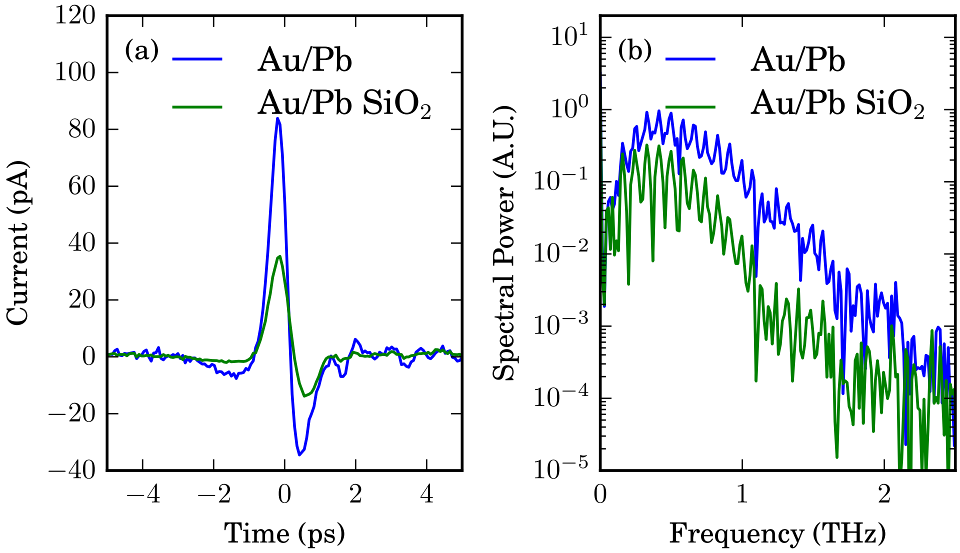

Figure 4.7: THz-TDS scans for both the SiO$_2$ insulated and the uninsulated Au/Pb emitters patterned on SI-GaAs. (a) shows the time domain scans whilst (b) shows the relating Fourier transfroms. With an SiO$_2$ layer the Schottky effects are eliminated, reducing the THz field output by more than half and showing the Schottky barrier plays a much greater role in DM emitters than observed in single edge LPD emitters.

measurements an average power of 7 mW was incident on the receiver and the pump beam was optically modulated to provide a signal for detection with a lock-in amplifier. The emitters were mounted without any focusing silicon lenses and were illuminated with a full $1/e^2$ pump beam spot diameter of 1.2 mm. This spot size permitted a maximum of 67 double-metal strips to be illuminated and allowed the emitter to generate planar THz waves, instead of acting as a point source. In the case of fluence measurements, an objective lens and variable neutral density filter allowed the intensity and spot size of the pump beam on the emitter to be adjusted.

4.4.1 Fluence saturation

Firstly, the output of the fabricated DM emitters were measured in the setup described previously. Figure 4.7 shows the time-domain scans and their corresponding

Fourier transforms in (a) and (b) respectively for the DM emitters illuminated with 180 mW average power. The presence of an SiO$_2$ layer quells the effect of the Schottky barrier, reducing THz output by more than half when compared to the uninsulated emitter. In chapter 1 I discussed that the presence of an insulating layer between the metal and semiconductor does not affect the output of a single LPD emitter. This implies the Schottky barrier plays a more important role in multiplexed emitters than single LPD emitters. This is most likely due to the size and scale of the devices. The

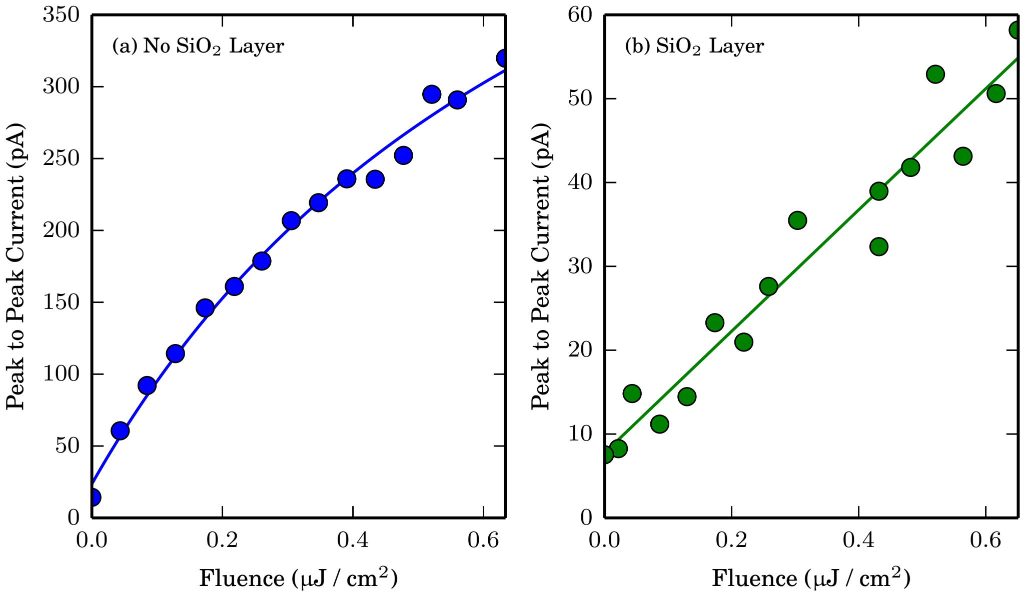

Figure 4.8: These figures show the fluence dependence of Au/Pb emitters without an SiO$_2$ layer, (a), and with an insulating SiO$_2$ layer, (b). The pump beam spot radius was set at 430 μm and the saturation fluence, F_{sat} was determined to be 0.82 μJ cm^{-2} for (a), whereas (b) shows no saturation.

currents induced by the Schottky barrier height differences occur near to the metal. With repeating structures fabricated over a 15 μm period these currents can have a greater effect on emission. Our results also showed that DM emitters fabricated on an LT-GaAs substrate produced minimal emission. This is likely due to the fact that Schottky effects are not as influential in LT-GaAs [115] but could also be caused by unquantified fabrication errors.

Next, the pump beam was focused with an objective lens to a spot size of 430 μm on the emitter, illuminating approximately 28 double-metal elements, and incident optical power was varied to investigate the fluence characteristics of DM emitters. Figure 4.8 shows the peak-to-peak current measured by the lock-in amplifier plotted against fluence for the uninsulated (a) and the SiO$_2$ insulated (b) emitters. The saturation curves were fitted using the formula

$$E_{\mathrm{THz}}(F) = A\frac{F}{(F + F_{\mathrm{sat}})} \tag{4.2}$$

Where F is the optical fluence, F_{sat} is the optical saturation fluence and A is the coefficient describing efficiency. F_{sat} for the uninsulated device was found to be 0.82 μJ cm^{-2}. For the SiO$_2$ insulated device no saturation was observed. The saturation observed in the uninsulated emitter is attributed to charge accumulation within the depletion region, as is observed with single LPD emitters on SI-GaAs. At higher fluences the drift current of electrons moving from the metal to the semiconductor is reduced. Higher carrier concentrations lead to higher carrier density, a decrease in barrier height and a higher Fermi energy in the semiconductor [115, 128].

4.4.2 Polarisation and alignment

Figure 4.9 shows that both insulated and uninsulated Au/Pb DM emitters exhibit the same emission dependence with optical pump polarisation as single edge LPD emitters as discussed in the previous chapter. Enhanced THz emission is observed for polarisation angles perpendicular to the double-metal strip lines (TM). This dependence is also apparent in the insulated emitter, suggesting the enhanced emission is due not only to Schottky enhancement but also by diffraction causing carriers to form nearer to the metal boundary.

The LPD effect allows transmission of THz radiation along the same direction as the pump beam. The regular photo-Dember effect in a bare semiconductor produces THz emission perpendicular to the direction of the pump beam. To couple emission out parallel to the pump beam direction the semiconductor must be angled with respect to the pump beam. Any change in this angle will affect the amplitude of the THz emission. The emission dependence on emitter angle with respect to the pump beam was examined

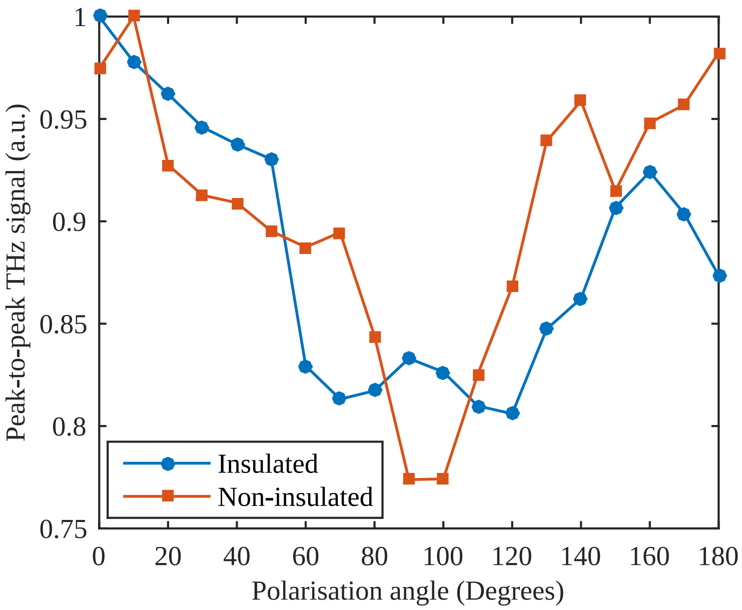

Figure 4.9: Normalised pump beam polarisation dependence of the insulated and uninsulated Au/Pb DM emitters. The angles of 0° and 180° correspond to TM polarisation and 90° to TE polarisation as described in chapter 3. Both emitters show strongest emission from a TM polarised pump beam, with reduced emission under TE polarisation. As the insulated emitter is unaffected by Schottky effects this dependence is likely due to enhanced diffraction of the pump beam at TM polarisation.

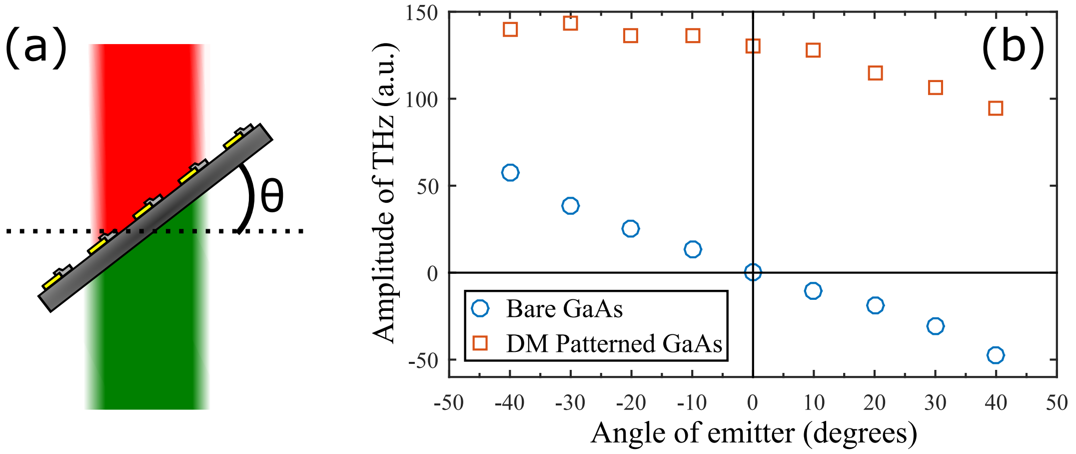

Figure 4.10: Figure (a) shows a schematic for the angular measurements and defines θ. Figure (b) shows a plot of the amplitude of the emitted THz radiation with variation of the emitter angle in respect to the pump beam for an Au/Pb DM emitter (red squares) and bare SI-GaAs (blue circles). The DM emitter shows constant emission and no polarity flip compared to the bare SI-GaAs, which shows a polarity flip and no emission at 0° as expected.

for the uninsulated Au/Pb emitter and compared with that of a piece of bare SI-GaAs. The schematic for this experiment is shown in figure 4.10(a) and the peak-to-peak THz emission with respect to emitter angle results are shown in figure 4.10(b). At an angle of 0° the bare SI-GaAs shows no detectable THz emission parallel to the pump beam as expected. As the angle is increased the THz emission increases linearly, with negative peak-to-peak values representing a reversal in the polarity of the THz pulse. The DM emitter demonstrated strong emission at 0° and steady amplitude emission at other angles with no polarity inversion. This is attributed both to the LPD effect and the intrinsic net lateral current due to the Schottky effects maintaining a consistent emission direction. For angles between +10° and +45° the peak-to-peak THz amplitude gradually decreases with increasing angle. The asymmetric nature of this angle dependence suggests the emitting dipoles may be inhibited by this positive angular change. This could be due to a simple shadowing effect of the metals on the semiconductor surface, shifting the dipoles away from the metals. Another likely cause could be due to the photon drag effect. This is where photons absorbed by the material impart their momentum to the photogenerated carriers. Changing the angle of the emitter would either increase or decrease the momentum of carriers diffusing underneath the Pb layer, thus producing an overall effect on the THz emission.

4.4.3 Emitter lifetime

After the initial fabrication of the Au/Pb DM emitters, it was noted that over time the THz output gradually decreased. This is due to oxidation of the Pb strips as well as mechanical wear (scratches, burns etc). To combat this loss of output another Au/Pb

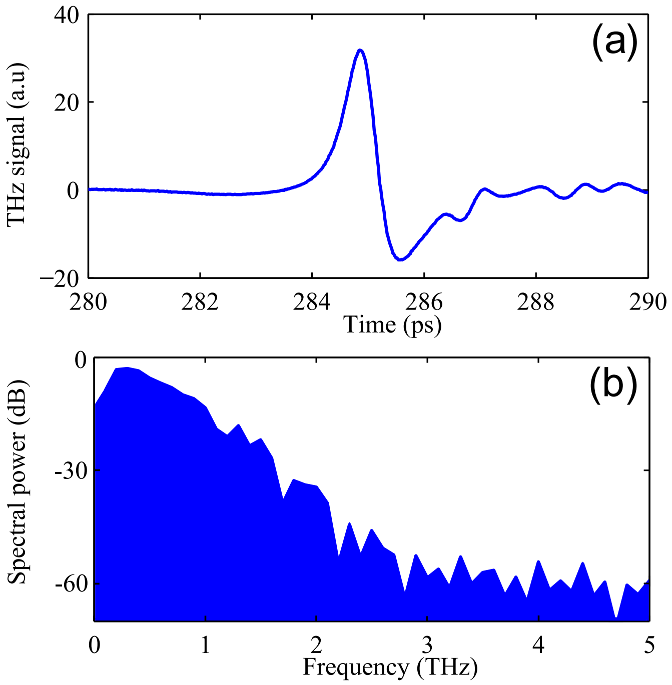

Figure 4.11: A time-domain scan of a coated Au/Pb DM emitter illuminated with spot size and fluence of 0.23 µm and 2.4 µJ cm^{-2} respectively is shown in (a). The corresponding Fourier transform is shown in (b). This emitter exhibits up to 3 THz bandwidth to 1 dB above the noise floor, with SNR of ∼56 dB and shows no loss in output over time due to oxidation.

emitter was fabricated. Deposition thicknesses of 60 nm for both Au and Pb were used with a 5 nm Cr adhesion layer between the Au and semiconductor, and after deposition a polyimide (PI) coating layer was spun onto the emitter surface and baked to protect the Pb from oxidation. The newly fabricated emitter was aligned in a TDS setup with an objective lens and the spot size was adjusted to achieve higher fluence for maximum THz transmission. Approximately 15 double-metal strips were illuminated with a 1/e^2 spot radius of 115 µm and a fluence of 2.4 μJ/cm^2. Figure 4.11(a) shows the time domain scan for the coated DM emitter. From figure 4.11(b) an improvement in bandwidth with respect to the previous Au/Pb emitter bandwidth in figure 4.7 can be noted. This is due to the thickness of the metals deposited, as the previous emitter had much thicker depositions than intended. The thinner metals deposited on this Au/Pb emitter allow larger bandwidth as the higher THz frequencies generated underneath the Pb are not reflected and so not suppressed. The coated emitter also boasts an improved signal-to-noise ratio of 56 dB and, due to the coating, does not exhibit any loss of signal over time.

4.4.4 Temperature characterisation

The DM emitters were mounted within a helium flow cryostat to test their low temperature characteristics. Both the uninsulated DM emitter and the SiO$_2$ insulated emitter were

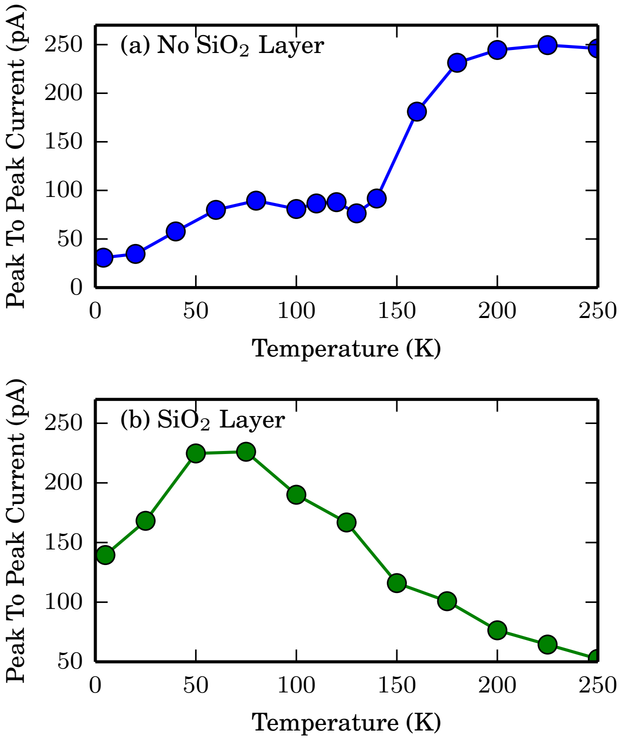

Figure 4.12: Peak-to-peak THz emission for the Au/Pb emitters with varying temperature. (a) shows the temperature dependence for the emitter without an insulating layer and (b) shows the temperature dependence for the emitter with the SiO_2 insulating layer.

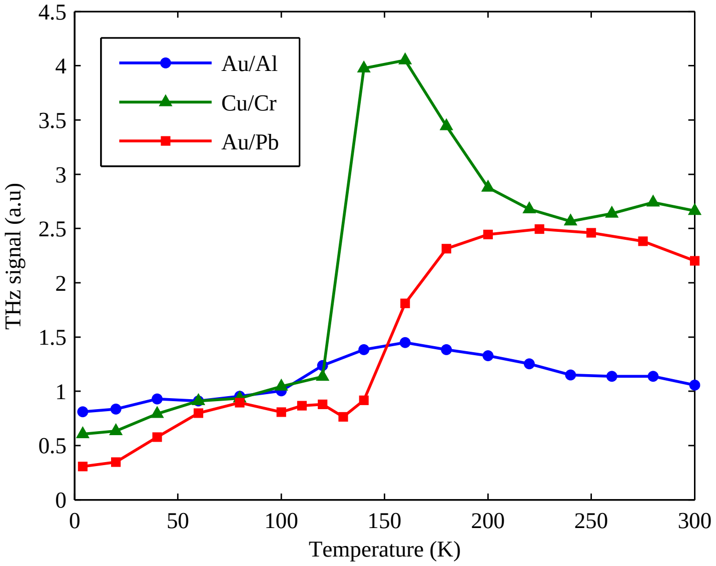

Figure 4.13: Peak-to-peak THz emission with temperature for Au/Al (blue circles), Cu/Cr (green triangles) and Au/Pb (red squares) emitters. Cu/Cr emitters show the strongest THz emission which peaks between 140 and 160 K.

mounted in turn and were aligned within a TDS set up of the same design as the one described previously. The THz emission of both emitters was investigated over the temperature range of 4 - 300 K. Figure 4.12 (a) and (b) show the peak-to-peak THz signal at different temperatures for the uninsulated and insulated emitters respectively. For the SiO_2 insulated emitter in 4.12(b) the THz output increases with decreasing temperature, with an optimum emission temperature at ~50-80 K. This increase in output is attributed to higher electron mobility at low temperatures [135], as the free electron path length is increased due to fewer free carriers being present. This allows the formation of a stronger dipole and implies carrier diffusion is the main source for THz emission when Schottky barrier emission is removed. Both emitters exhibit a decrease in THz output below 50 K which is in accordance with the reduction in electron mobility in GaAs at these temperatures [135]. In the case of the uninsulated emitter in (a) there is a contribution from the Schottky barriers formed at the Au/GaAs and Pb/GaAs interfaces as well as emission due to diffusion. These emitters show reduced performance when the temperature is decreased below 200 K. This follows the temperature relationship of the Au/GaAs Schottky barrier height [136]. Between 50 K and 100 K the peak-to-peak THz emission remains consistent, experiencing a small rise in output. This coincides with the temperature region in which carrier mobility reaches its peak values and Schottky barrier height approaches its minimum values [135, 136]. These results suggest that for the DM emitters the Schottky effects dominate the emission at room temperature, whilst at low temperatures the carrier mobilities allow the LPD effect to become dominant. These temperature characteristics mean that the operating conditions of the devices should be considered prior to fabrication to achieve the best function possible.

For a comparison further DM emitters were fabricated using metal pairings of Au/Al and Cu/Cr, which were chosen due to their differing work functions and skin depths in the THz range [74, 116, 127]. The thickness of each of the metals deposited was kept at 60 nm with a 5 nm Cr adhesion layer between the Au and semiconductor. The peak-to-peak emitted THz was measured for the same temperature range as before and the results are shown in figure 4.13 along with the results for the Au/Pb emitter for a direct comparison. The Au/Al emitter demonstrates a consistent peak-to-peak THz emission throughout the temperature range, varying in output by only 48 %. The Cu-Cr and Au-Pb emitters show the highest peak-to-peak THz output of the double-metal emitters at room temperature. The Cu/Cr emitter also exhibits the largest peak-to-peak output between the temperatures of 140 and 180 K.

4.4.5 Characterisation of metals

To investigate the effects of the different metals on the emitted THz, each of the metals used in the DM emitters were separately fabricated to form single edge LPD emitters. These were aligned in a similar TDS setup without the cryostat present. For each emitter

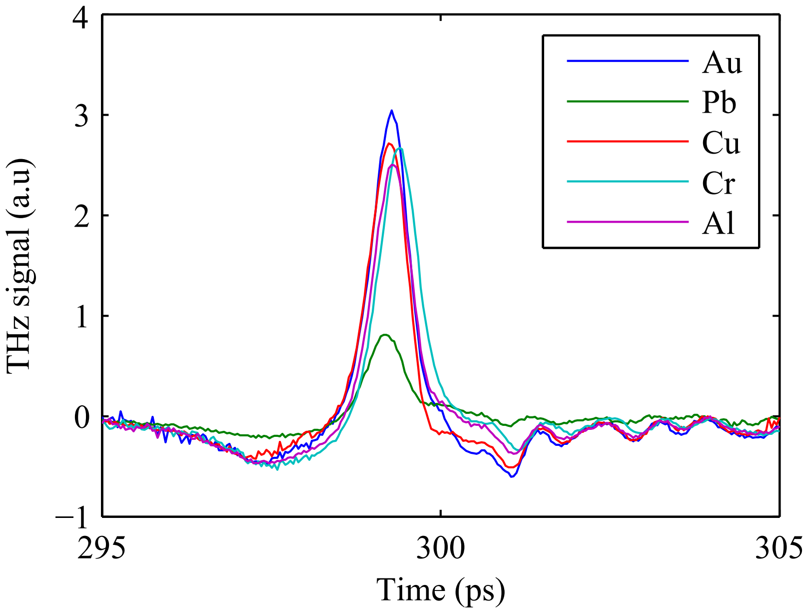

Figure 4.14: TDS scans for each of the single edge emitters. Au, Pb, Cu, Cr and Al are represented by the dark blue, green, red, light blue and purple lines, respectively. Most of the metals show similar emission strength suggesting the Au/Al and Cu/Cr emitters are primarily Schottky driven.

an objective lens was used to focus the pump beam onto the metal edge and spot size was adjusted to achieve maximum THz transmission. Similar to the DM emitters, they were aligned without the presence of an Si-lens. Figure 4.14 shows TDS results for the single edge LPD emitters. The single edge Cu, Cr, Au and Al emitters show similar output, suggesting that the emission of the Cu/Cr and Au/Al DM emitters is driven mainly by Schottky effects. Due to a larger skin depth and lower conductivity than Au, Al and Cu, it was expected that the Cr emitter would show THz output lower than these and above the Pb emitter. The increased output of the Cr device could be due to the semiconductor surface quality of the emitters, or may be due to a thicker Cr deposition than intended. Au shows the strongest emission while Pb shows the weakest emission. This is to be expected due to Pb having the largest skin depth of the chosen metals in the THz range [127] and is the reason this metal pairing was chosen for our first DM emitters. A similar bandwidth and SNR was achieved with the Cu/Cr emitter compared with the Au/Pb device. As LPD emitters are not subject to the dark current limitations that photoconductive antennas are and emission scales with area, it would be possible to improve on this result with access to higher laser powers and by expanding the beam to a larger spot size. As discussed previously, the Schottky barriers are strongly affected by the quality of the metal-semiconductor contact [132] which can vary depending on the oxidation and passivation of the semiconductor surface prior to applying the metal [137]. We have not used any surface passivation technique in the development of our emitters to simplify the fabrication process. As this could lead to variation in the emitter efficiency we fabricated a further two Au/Pb and Cu/Cr emitters and found a variation of peak-to-peak output of 10% between similar emitters.

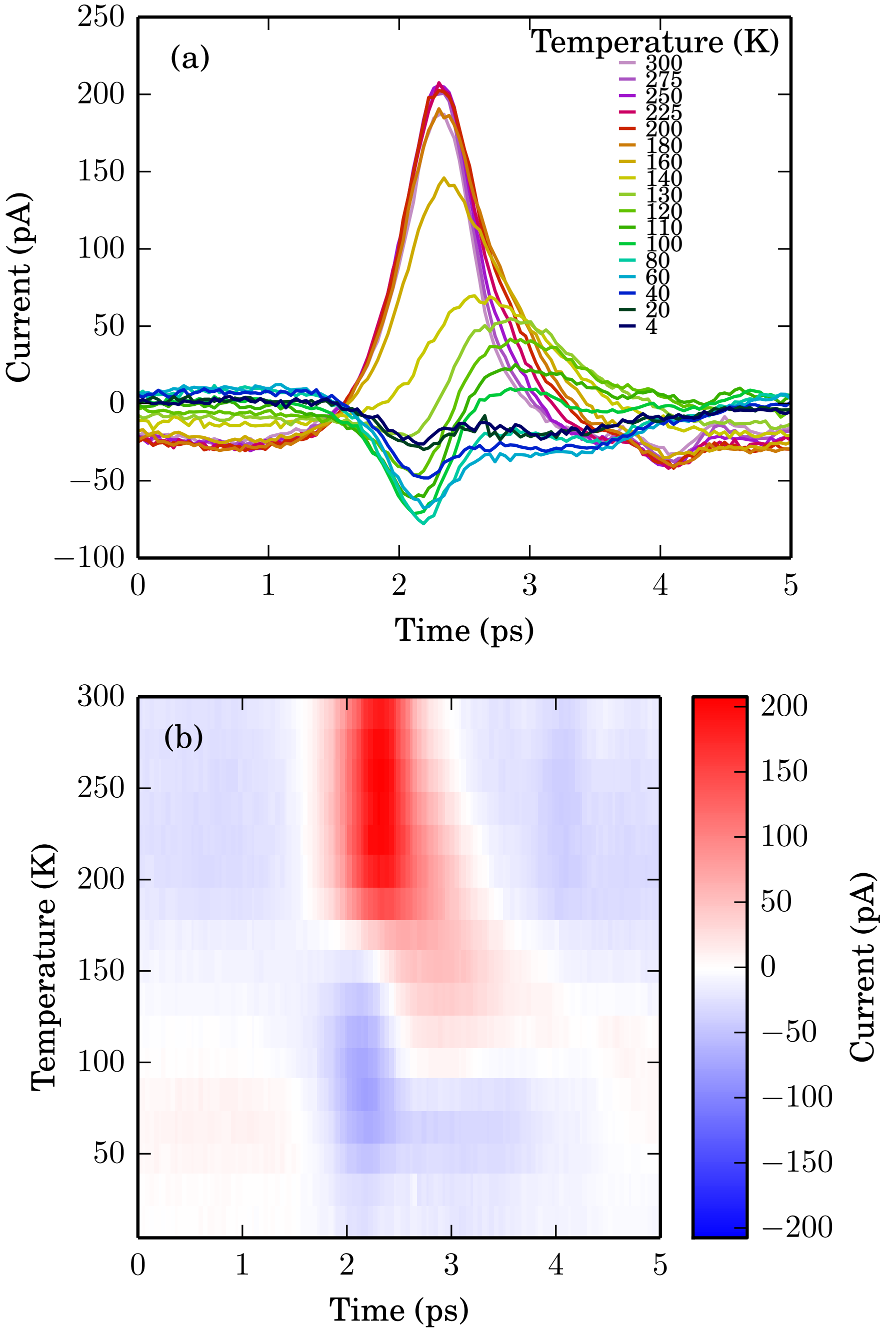

Figure 4.15: Temperature dependence THz-TDS scans of an Au/Pb DM emitter fabricated with no insulating layer ranging from 4-300 K. Figure (a) shows the individual THz-TDS of detected current with time superimposed with each other over the range of temperature. Figure (b) shows the same data as figure (a) as a two dimensional image of detected current against temperature and time.

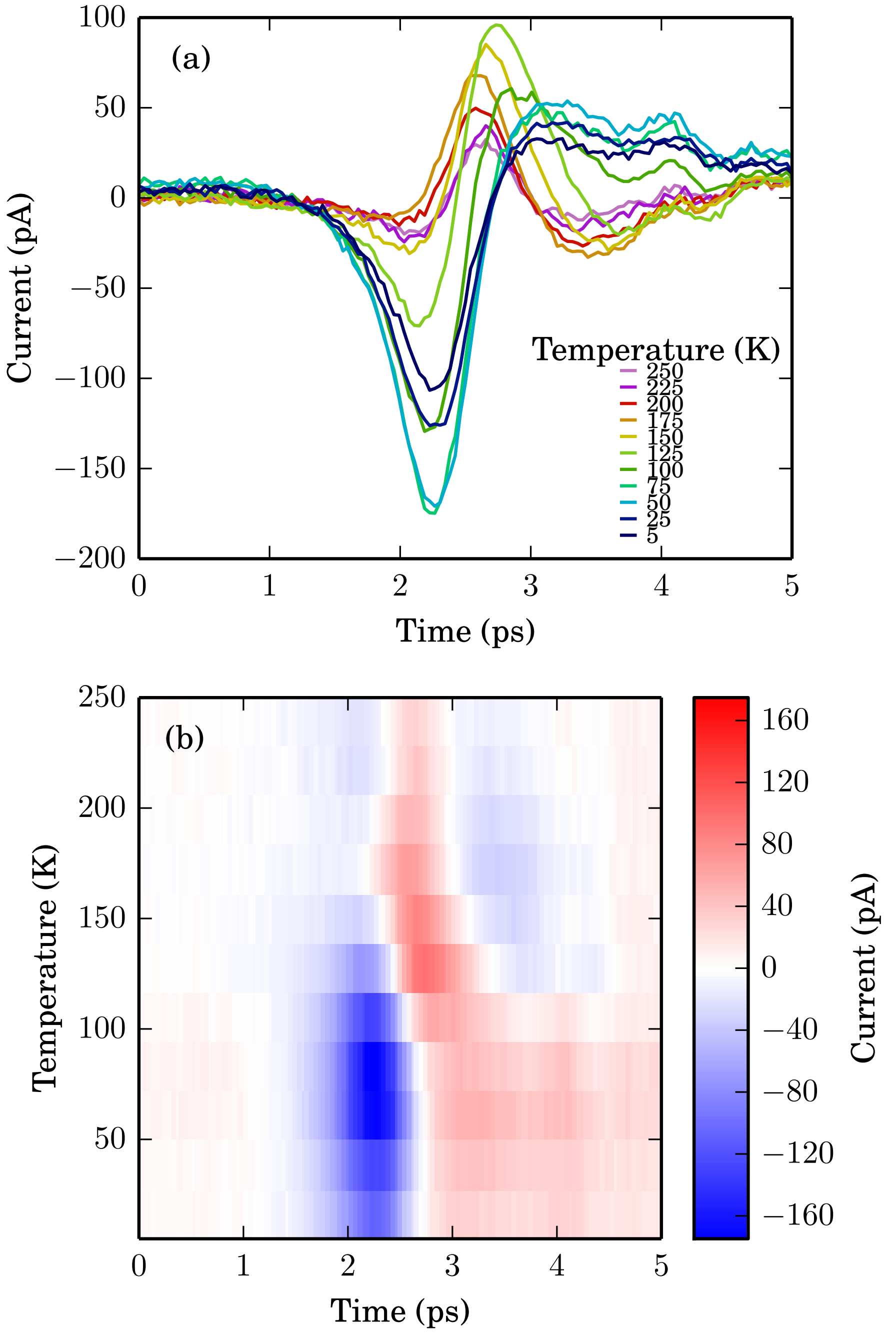

Figure 4.16: Temperature dependence THz-TDS scans of an Au/Pb DM emitter fabricated with an SiO_2 insulating layer ranging from 5-250 K. Figure (a) shows the individual THz-TDS of detected current with time over the range of temperature. Figure (b) shows the same data as figure (a) as a two dimensional image of detected current against temperature and time.

4.4.6 Temperature dependent polarity flip

A polarity flip of the emitted THz radiation was observed for both insulated and uninsulated emitters between 80 K and 120 K. Polarity flips in SI-GaAs have previously been observed to demonstrate a dependance on the polarisation of the exciting beam due to an enhanced electric field at the Au/GaAs interface [115]. The flip in polarity was attributed to competing THz emission mechanisms such as Schottky emission. The polarity dependence for the uninsulated Au/Pb emitter is shown in figure 4.15 and the same dependence for the insulated emitter is shown in figure 4.16. For the uninsulated emitter the main pulse peak is shown to shift by ∼500 fs betweek 200 K and 100 K.

Comparing figure 4.15 (b) and figure 4.16 (b) directly we see that an increase in signal amplitude occurs at 2 ps for the temperature range of 50-100 K without being shifted in time. This rise in output is attributed to the increased photo-Dember efficiency due to carrier mobility as it is evident in both the uninsulated and insulated emitters. The polarity flip is evident both in the uninsulated and insulated Au/Pb emitters as well as the Cu/Cr emitter. Several tests were carried out to identify contributing factors to the polarity inversion. The polarisation of the pump beam, the fluence upon the emitters and the wavelength of the laser were varied, however, the polarity flip remained evident and unchanged in all cases. The single edge Au LPD emitter was also mounted in the cryostat

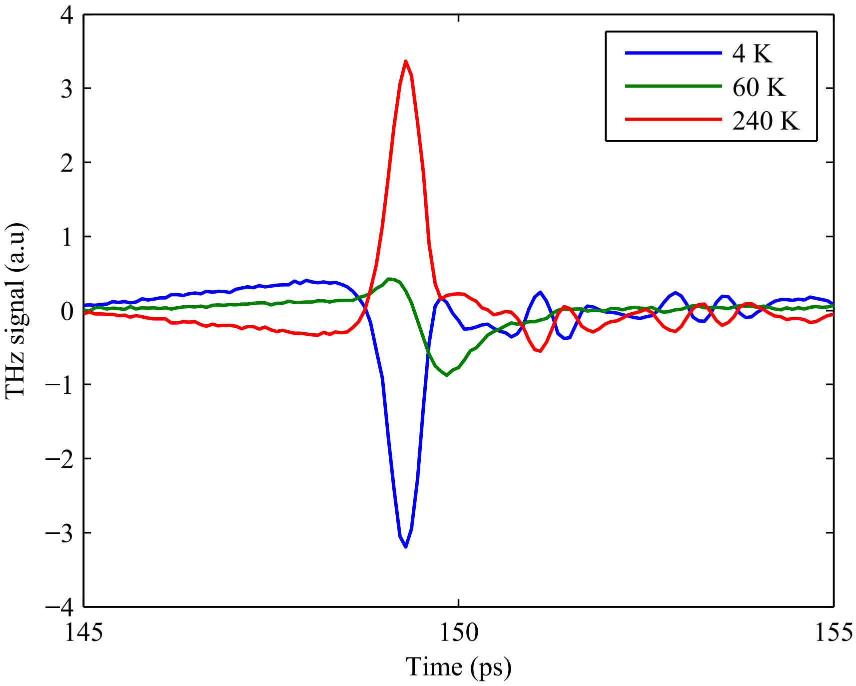

Figure 4.17: Time domain scans for a single edge Au emitter at three different temperatures. The red line shows the THz TDS scan at 240 K. As temperature is reduced the signal gradually decreases to the level shown by the green line at 60 K. Below this temperature the polarity reverses and amplitude gradually increases to the large, inverted signal at 4 K shown by the blue line.

to test for a polarity reversal. Figure 4.17 shows the resulting TDS measurements at 4, 60 and 240 K. The polarity reversal is still evident in all single emitters utilising only one metal. This suggests that the flip in polarity is linked to some intrinsic property of the SI-GaAs semiconductor competing with THz emission. Nakajima *et al.*, [138] found evidence for polarity reversal with temperature in bare InP surfaces. This was attributed to competition between the drift current caused by the surface electric field and diffusion currents due to the LPD effect, where at low temperatures the diffusion dominates causing a flip in signal polarity. This is not completely applicable in the case of the DM emitters as there is the Schottky effect on the surface fields from the presence of the metals. However, competing mechanisms would explain why the uninsulated Au/Pb emitter exhibits a lower THz output than the insulated Au/Pb emitter in the region where electron mobility is at its highest value. Only the Au/Al DM emitter did not exhibit a polarity flip with temperature. This may be due to the similar skin depths of Au and Al, their differing work functions, or could be an attribute of surface quality of that particular emitter.

4.5 Optimisation

As mentioned previously, Schottky effects can be insulated against by a layer a few nm thick [121]. As such, it is possible that the 5 nm Cr adhesion layer applied beneath the Au would be masking the work function of Au with the lower work function of Cr. To

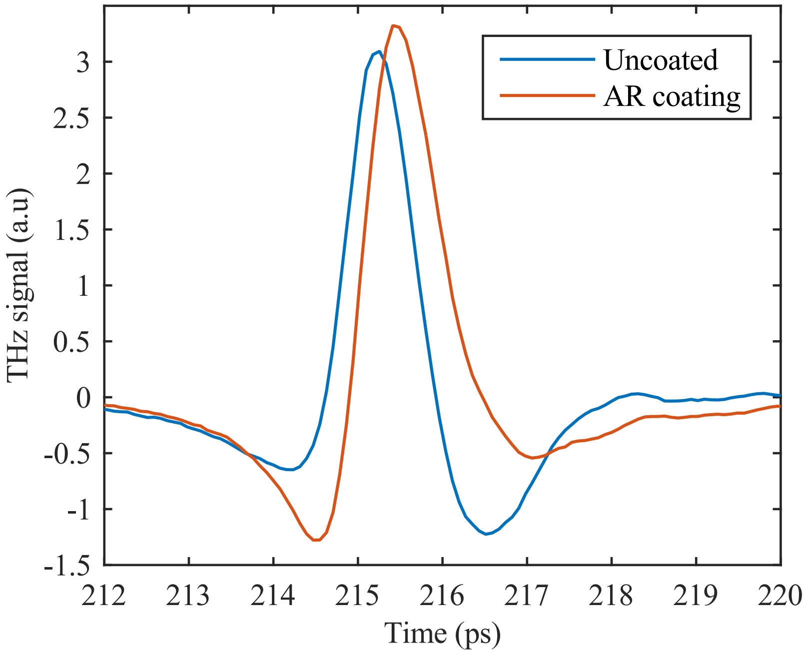

Figure 4.18: Time domain scans for the same Au/Pb emitter without (blue line) and with (orange line) an AR coating applied. The coating enhanced the pump beam absorption of the emitter, allowing a ∼7% increase in THz output.

investigate these effects a further fabrication of Au/Pb emitters were made without the Cr adhesion layer. As the Au would experience a reduced adhesion, the Pb was applied during the first stage of photolithography to prevent exposing the Au to damage. After fabrication the output of these emitters were compared to one of the previous generation in a typical THz-TDS setup. The results showed similar THz output to the emitters with a Cr adhesion layer. Due to uncertainty in surface quality and reduced adhesion of the Au it is difficult to quantify if the removal of the Cr layer had any affect.

THz emission is dependent on the pump beam power, so stronger absorption of the pump beam by the semiconductor will result in greater emission. A method of enhancing the absorption of the pump beam is by applying an anti-reflection (AR) coating to the surface of the emitter. A 134 nm thick layer of SiO_2 was deposited onto the surface of an Au/Pb DM emitter to act as an AR coating for a pump wavelength of 780 nm. To test the effectiveness of the coating 100 mW of pump beam was directed at a piece of bare GaAs and the reflection was captured by a power meter. The was repeated with a bare patch on the AR coated emitter and the reflected beam power was found to have reduced by $\sim$10%. Whilst this is a long way from being an ideal AR coating it does show reduced reflection and would work as a benchmark for future processing. THz scans were performed on the same emitter before and after deposition of the AR coating with a pump power of 150 mW and the results are shown in figure 4.18. From this a small ($\sim$7%) enhancement of the emitted THz can be seen from the AR coated emitter. This enhancement is comparable to the reduction in reflection of the device and an improved AR coating could lead to significant improvement of DM emitters output.

4.6 Graphene DM emitters

In recent years there has been evidence for THz emission from many different materials such as; ferromagnetic films [85], black silicon [139] and vertically aligned InN nanorods [86]. THz emission has also been observed in graphite flakes [140] and even from graphite in the form of a pencil drawing [141]. It is these observations which has led to the current interest in graphene as a THz device. Graphene is composed of a single layer of carbon atoms arranged in a hexagonal “honeycomb” lattice. The structure itself allows the charge carriers to have high mobilities and show ballistic transport at room temperatures, leading to their title of massless Dirac fermions [142, 143]. IR and THz spectroscopy has been used to characterise graphene [144, 145] and many devices for the absorbtion and photodetection of THz based on graphene have also been created, including; graphene micro-ribbons [146], transistor based photodetectors [147], dielectric slab structures for tunable absorbers [148] and many devices which utilise plasmonics and metamaterials in their function [149–151]. Emission of THz from graphene devices is an area which is yet to be fully explored. Due to the comparable mobilities between electrons and holes in graphene, it is unlikely that the dipole necessary for LPD emission

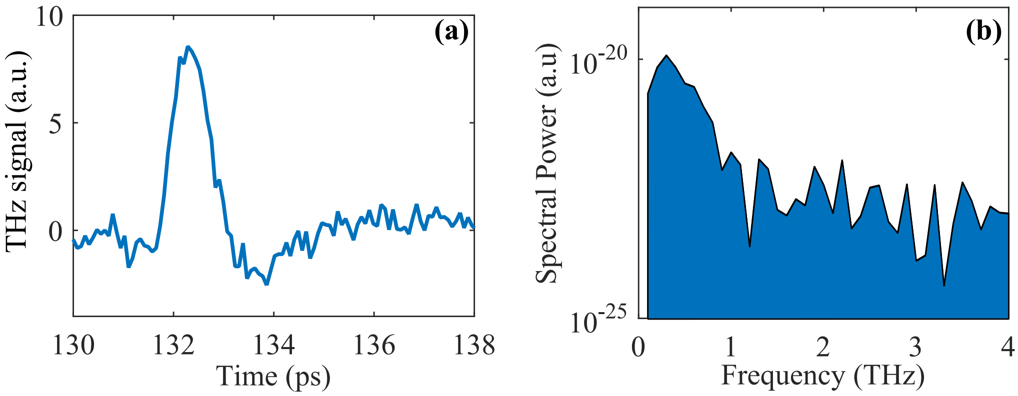

Figure 4.19: Initial THz-TDS scans for DM emitters fabricated on single layer graphene. The TDS measurements is shown in (a) with its corresponding spectrum shown in (b). The signal produced is small and barely above the noise floor due to the low absorption of the optical pump by the graphene in comparison to bulk GaAs.

could form. Therefore, THz emission from graphene is usually attributed to the photon drag effect, where photon momentum is transferred to an electron causing a net current in the material [152]. This effect has been observed in graphene monlayers [153] as well as carbon nanotubes [154]. Though restricting to the LPD effect the similarities in mobility could be exploited by Schottky contacts, making the DM emitter design a possible solution for THz emitters fabricated on graphene. A similar concept of using two metals with different work functions was explored by Mueller *et al.*, for use as a photodetector [155]. In this case two metals mere fabricated as interdigitated finger electrode structures on top of graphene and the differing work functions were exploited to measure a photocurrent generated by a 1.55 µm laser.

Monolayer CVD grown graphene was sourced from the company 2D-tech. The graphene was deposited on a z-cut quartz substrate as this exhibits very low loss at THz frequencies so can be used in a transmission THz-TDS setup without attenuation [5, 156]. The metal pairing of Au/Pb was fabricated in double-metal strips on the surface of the graphene. This was then coated with a PI layer to protect the Pb from oxidisation. The resulting DM graphene emitter was aligned within a linear THz-TDS setup, the resulting scan is shown in figure 4.19. The TDS scan in figure 4.19(a) shows a THz pulse generated from the graphene. The amplitude of the emitted pulse was over an order of magnitude lower than that observed from DM emitters on SI-GaAs. Figure 4.19(b) shows the relating fourier transform of the time-domain data. The emitter exhibited poorer bandwidth and a much lower SNR when compared to DM emitters on semiconductor, though this could be due to higher frequencies being indistinguishable from the noise floor. This low output in graphene DM devices is attributed to the pump beam absorption. Visible wavelength absorption of graphene is high (at around 2.3%) considering the atom-thin nature of the material, but for a device this is still quite weak [157, 158]. The pump absorption could be increased by using multilayer graphene, leading to higher

THz output, though increasing the number of layers has been known to reduce carrier mobility [159]. The absorption of 800 nm light is around 68% for GaAs [160]. If graphene absorption could be brought into line with this, and the conversion of the pump beam to THz output in graphene remained linear with pump absorption, we could expect an increase in output of around 30 times. However, though mobilities in suspended graphene are high the mobility can be reduced significantly when graphene is applied to a substrate [161], something that would need to be taken into account for future fabrication. A single LPD emitter was also fabricated on monolayer graphene, however this yielded no detectable THz emission. This is attributed to the similar mobilities of electrons and holes in graphene meaning a substantial charge separation cannot form from diffusion alone and so the emission of the DM-graphene emitters are highly dependent on the Schottky effect. Varying the fluence on the graphene emitter yielded little change in the output or spectrum, so this device could not be fully characterised.

4.7 Conclusion

In this chapter I demonstrated a new multiplexed emitter which utilises the LPD effect coupled with the Schottky effect to produce THz emission. These emitters rely on a double-metal structure formed of metals with different skin depths and work functions to engineer the LPD effect and band bending from Schottky contacts and provide an emitter which does not require any focusing element for the pump beam. Moreover, THz emission from DM emitters has proven to be unaffected by emitter angle with respect to the pump beam, making these devices ideal for use as drop-in components in existing setups. These devices are easy to fabricate and do not require an electrical bias so are robust and will not suffer from electromigration effects. Due to surface quality, similar devices showed a 10% variation in output, therefore the strength of emission is difficult to predict without first fabricating the devices. Emission at room temperature is primarily Schottky driven, though carrier diffusion and the LPD effect dominate at low temperatures. These devices perform well at low temperatures in the range of 50-80 K and so could be easily used in cryogenic applications where alignment may be restricted. DM structures were also patterned onto monolayer graphene. Very weak emission was measured from these devices and was attributed to the low absorption of the pump beam and reduced carrier dynamics for graphene on a substrate.

DM emitters on SI-GaAs show bandwidth comparable to a PC antenna and good SNR. As LPD emitters are not subject to the dark current limitations that PC antennas are and emission scales with area, it would be possible to improve on these results with access to higher laser powers and by expanding the beam to a larger spot size. There is also scope for possible further improvement with different metal pairings that may optimise both the Schottky contacts and the LPD effect. The coating to prevent the metals oxidising can also double as an anti-reflection coating to increase pump beam absorption and enhance THz emission even further.

A similar nano-scale bi-metal type device, the TeraBlast, is currently being marketed by Protemics GmbH aimed towards the near field imaging market. However, the function of these devices is attributed solely to effects of the metal work functions.

Chapter 5

Terahertz beam steering and focusing

In the previous chapter I demonstrated a THz emitter which utilises both the LPD and Schottky effects to produce observable radiation without the need for focusing optics or complex alignment. The device is formed of overlapping strips of two different metals on a semiconductor to engineer the reflectivities and work functions and achieve net THz emission. I characterised these emitters and investigated the use of different metal pairings to improve their output and performance at various temperatures.

In this chapter I show that the emitted THz can be controlled and focused through manipulation of the infrared pump beam. As the DM emitters do not need any focusing optics for the pump beam it is possible to exercise a lot of control over the THz emission itself through shaping of the optical pump beam wavefronts. I show that it is possible to focus the THz emission directly onto the detector without the need for lenses or parabolic mirrors, proposing a lensless, compact spectrometer system. I also demonstrate circular DM emitters with a radial polarisation profile, showing that DM emitters could be designed for various applications.

5.1 Introduction

Over the past decade focus has begun to shift from generating THz radiation to controlling and guiding it, as this will be necessary for bringing THz technology to the consumer. Many methods for controlling THz once emitted have been investigated, including paper lenses [162] and tunable graphene metasurfaces [163]. Tsurupica (plastic) lenses which can focus both optical and THz light are now commercially available from companies such as Tydex and Menlo Systems. Work has also continued developing ways of efficiently coupling THz radiation into waveguides. THz can be guided along metal wires [164–

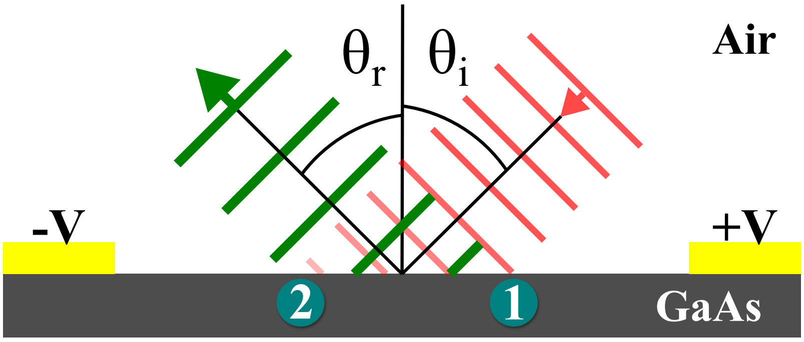

Figure 5.1: Diagram of beam steering. The optical pump beam (shown as red) is incident on a photoconductive antenna at angle θ_i. THz (shown as green) is first emitted at 1 before being emitted at 2. This introduces a phase delay to the THz wavefront, causing it to be emitted from the surface at angle θ_r=θ_i.

166], dielectric waveguides [167] and waveguides which combine metallic, dielectric and air components [61]. Other techniques for guiding and manipulating THz have utilised plasmonic structures, including; ultasubwavelength plasmonic waveguides [168], polarisation rotators [169], absorbers [149] and structures for THz collimation [60].

Aside from optics and waveguides, ways of controlling THz without the need for extra components have also been explored. These focus primarily on the manipulation of the exciting pump beam as it generates the THz pulse. It has been shown that changing the incident angle of the pump beam gives control over the emission direction of the THz radiation [170] and it has also been noted that it is possible to control the focus of the THz beam through manipulation of the optical pump beam [171]. This effect occurs due to the way the pump beam interacts with the semiconductor and is illustrated in figure 5.1. The pump beam frees carriers in the semiconductor which then radiate THz. If the pump beam wavefront approaches at an angle, θ, to the semiconductor surface normal then THz will be excited first at position 1 before position 2 introducing a phase delay along the THz wavefront generated. If the distance between 1 and 2 is greater than the THz wavelength then the phase difference will be sufficient to cause the THz to be emitted at an angle similar to θ [170]. This principle can also be applied to the focusing described in [171], and a diagram of this is shown in figure 5.2. When light is focused by a lens the wavefronts become curved in proportion to the focal length of the lens. Exciting an emitter with a curved wavefront would induce phase delays across the beam and result in a THz wavefront with the same curvature as the pump beam. The curved THz wavefront would come to a focus near to where the pump beam would have – the focal point of the lens – providing the pump beam spot size on the emitter is larger than the THz wavelength generated.

Without the need for focusing elements for the pump beam to operate and the possibility for size scaling, DM emitters are ideal candidates for characterising beam focusing effects by manipulation of the pump beam. As they do not require a bias it is also possible to locate them close to the detector without fear of parasitic coupling effects. This could

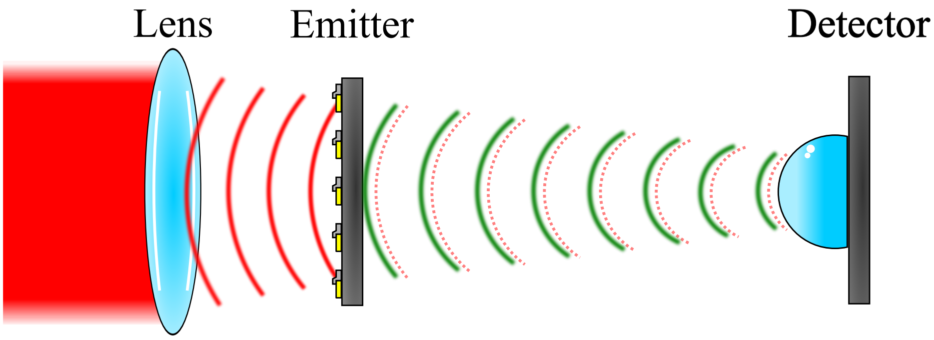

Figure 5.2: Example of the beam focusing mechanism. The pump beam is focused by a lens causing a curvature of the wavefronts and a phase difference across the beam. As the emitter is excited THz wavefronts are emitted with a corresponding phase difference, causing the THz to focus where the optical beam would have. The diagram shows the THz being directly focused on to a receiver.

allow a system as shown in figure 5.2 with no THz optics required. With current use of diode lasers for synchronous THz generation and detection [172, 173] it would be possible to develop a lensless, compact spectrometer for material characterisation.

5.2 A simple model

A simulation based on the Huygens priciple of wavefront propagation was created in Matlab to model the interference of multiple THz wavefronts with a phase difference. An array of sources emitting at 2 THz were modelled along the y-axis from y=-15 to +15 cm, with a period of 15 μm, to represent the dipoles formed at each double-metal strip. A phase delay was introduced between the sources to model excitement by a focusing pump beam with radius of curvature of 10 cm. The electric field contribution from each source was calculated using,

$$E(x,y) = E_0 \sum_j A(y) \exp\left[\mathrm{i}kR_j(x,y)\right] \tag{5.1}$$

where E_0 is the electric field and $R_j(x,y) = \sqrt{x^2 + y_j^2}$ is the distance of the calculation point j from the center of the beam, and y_j is the location of the j^{th} source from the center of the y-axis. A(y) describes both the amplitude and phase terms of the calculation by,

$$A(y) = \underbrace{\exp\left[\frac{-y_j^2}{D^2}\right]}_{\text{Amplitude term}} \overbrace{\exp\left[\frac{\mathrm{i}k}{2f}\right]}^{\text{Phase term}} \tag{5.2}$$

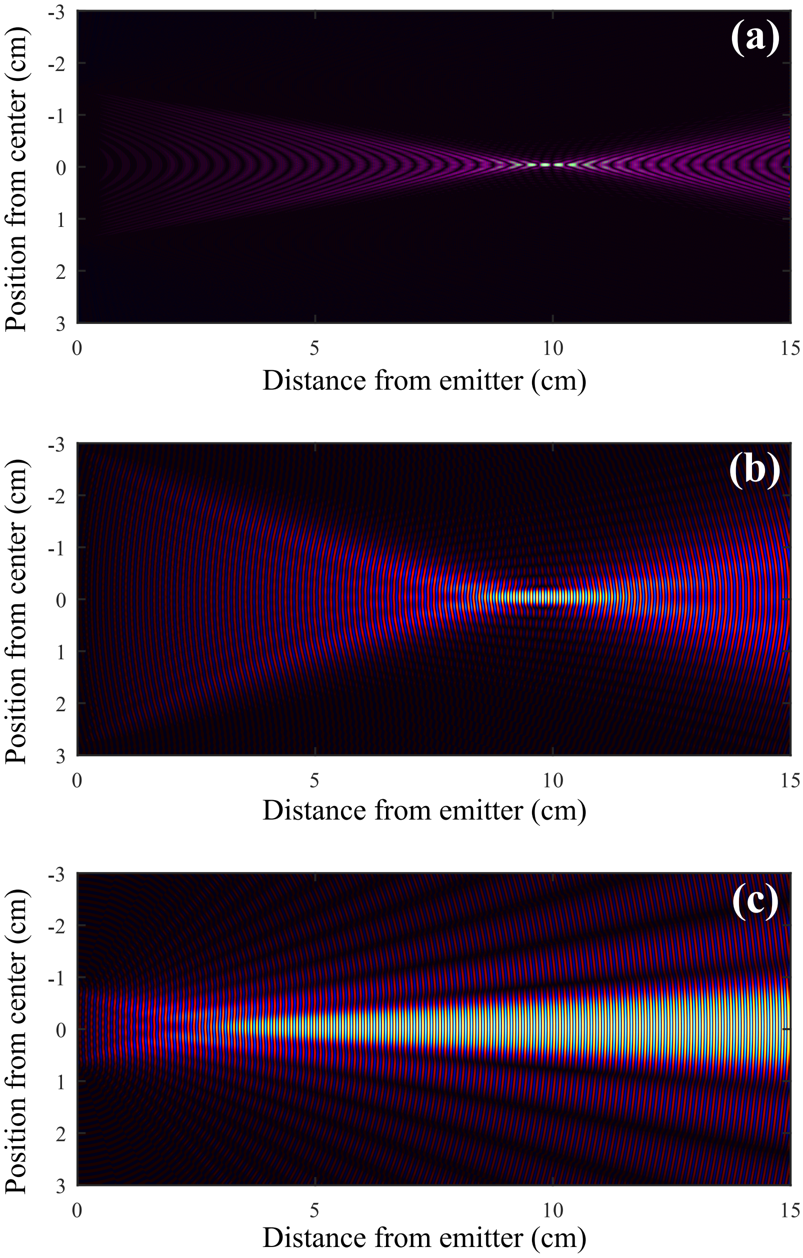

Figure 5.3: Simple model results for beam focusing. In (a) individual point sources are modelled along the y-axis at x=0, from y=-15 to +15 cm. They emit at 2 THz with a phase difference which would be induced by a 10 cm focal length lens. The THz produced then comes to a focus at 10 cm from the emitter. Figures (b) and (c) show the focusing effects at 250 GHz for different illumination spot sizes. In (b) point sources emit from y=-6 to +6 cm and the field reaches a focus at 10 cm from the emitter. In (c) point sources emit from y=-7.5 to +7.5 cm. In this case the width range of the emitting sources provides insufficient phase difference to cause focusing, and only diffraction is observed.

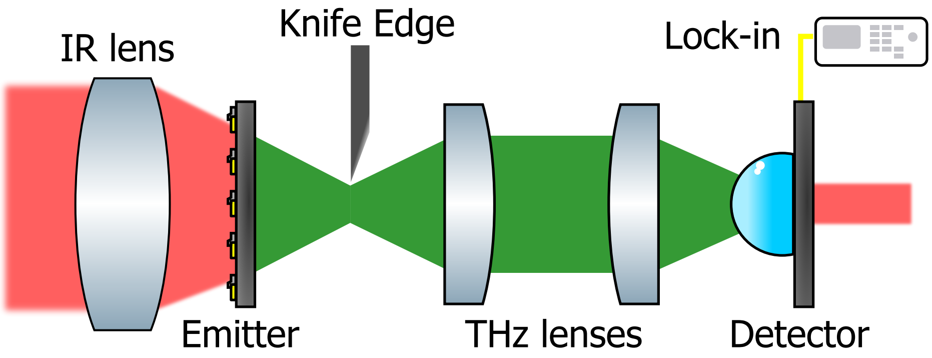

Figure 5.4: Diagram of the beam focusing setup. The optical pump beam (shown as red) is first expanded to a large diameter before being focused by an 88.3 mm focal length lens. The DM emitter is positioned along the focusing beam. Two Tsurupica THz lenses are used to capture the emitted THz (shown as green) and guide it to a focus on the detector. Knife edge measurements are made along the THz beam and the signal measured by the lock-in is noted.

where D is the diameter and f is the focal length of the lens. The results of this model are shown in figure 5.3(a). The phase difference between each source induces a curvature to the THz wavefronts relating to the focal length of the lens. This curvature causes a focusing of the THz at a distance of 10 cm from the emitter, a distance equal to the focal length used. This simple model shows how changing of the pump beam can directly affect the emission of THz and the properties of the beam. For the THz to come to a focus the phase difference between the dipoles formed must be adequate. The number of dipoles excited must be sufficient to achieve focusing over a range of frequencies. Figure 5.3(b) shows a situation where range of sources emitting at 250 GHz was increased to cover y=-6 to +6 cm. The field comes to a focus again at 10 cm from the emitter. By reducing the width range of the emitting sources we limit the focusing effects at lower frequencies, as the width range becomes close to the emission wavelength. Figure 5.3(c) shows the same case as (b) but with the range reduced to y=-7.5 to +7.5 cm. In this instance the width range of the source is insufficient to produce a focus at 250 GHz and only diffraction effects are observed. To observe focusing experimentally the pump beam must be expanded to a large size and a lens of appropriate focal length must be used to achieve the required illumination width on the emitter.

5.3 Experimental results

Several large area Au/Pb DM emitters measuring 2 cm by 2 cm were fabricated. Figure 5.4 shows the linear THz-TDS setup that was created for the beam focusing measurements. The parabolic mirrors were replaced with a rail, with the emitter and detector facing each other and optics positioned to slide along the rail for alignment. The output from a 100 fs, 80 MHz Ti:sapphire laser was split and used as both the pump beam and probe beam. The pump beam was modulated by an optical chopper and expanded to a diameter of

~2.5 cm. The expanded beam was then focused by a lens with an effective focal length of 88.3 mm. This size of pump spot and focal length of the lens was calculated to achieve a radius of curvature which would result in an x value of 1.75 mm, a value significantly larger then the THz wavelengths produced and sufficient to produce observable focusing of the THz emission. The large area emitter was placed at 37 mm from the lens, which formed an 11.8 mm optical pump spot width on the emitter. The emitted THz radiation was collimated by a Tsurupica lens and focused by a second Tsurupica lens onto a photoconductive antenna acting as receiver. The pump and probe beam powers were 500 mW and 7 mW, respectively. Knife edge measurements were made at 3 mm intervals along the THz beam between the emitter and first Tsurupica lens using a blade mounted on an x-y translation stage. The transmitted THz amplitude was read from a lock-in amplifier and the position of the knife edge was recorded from the x-y stage. The results in figure 5.5 show the $1/e^2$ diameter of the THz beam against distance from the emitter. The spot size decreases to a focal spot radius of ~1.3 mm at a distance of 50 ± 3 mm from the emitter, a total of 87 ± 3 mm from the lens, which is close to the focal length of the lens.

After the initial knife edge characterisation the rail set up was altered to resemble the setup in figure 5.2 with no optics between the DM emitter and photoconductive detector. The system was aligned so that the focus of the THz beam would fall on the detector. This was then adjusted to produce the largest detectable THz signal and a TDS scan was taken. Figures 5.6 (a) and (b) show the resulting TDS and frequency spectrum from this configuration respectively. The emitter exhibits reduced bandwidth in this configuration, achieving only around 1 THz. This is most likely due to the focusing conditions of the beam, with possible improvements by using much shorter focal length lenses to focus the optical pump beam onto the emitter to achieve a smaller focal spot size. Other reasons for this may be due to the size of the optical spot on the emitter limiting performance. To focus to a pump spot size considerably larger than the THz wavelengths means the

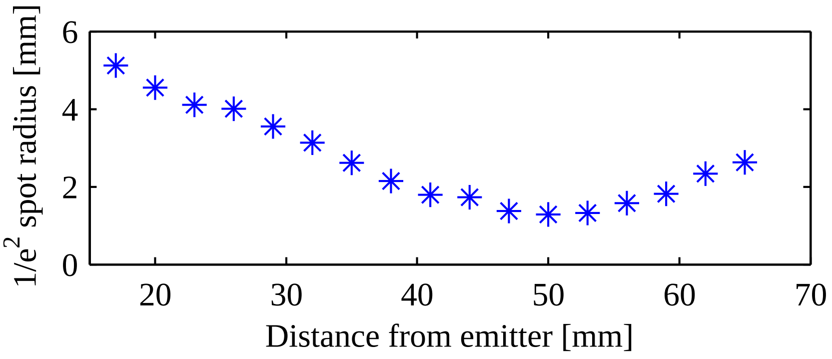

Figure 5.5: Resulting measurements of the $1/e^2$ spot size of the THz beam with distance from the emitter. The minimum spot size of the THz beam was measured to be ~1.3 mm at a distance of 87 ± 3 mm from the lens. This is close to the focal length of the pump beam lens, 88.3 mm.

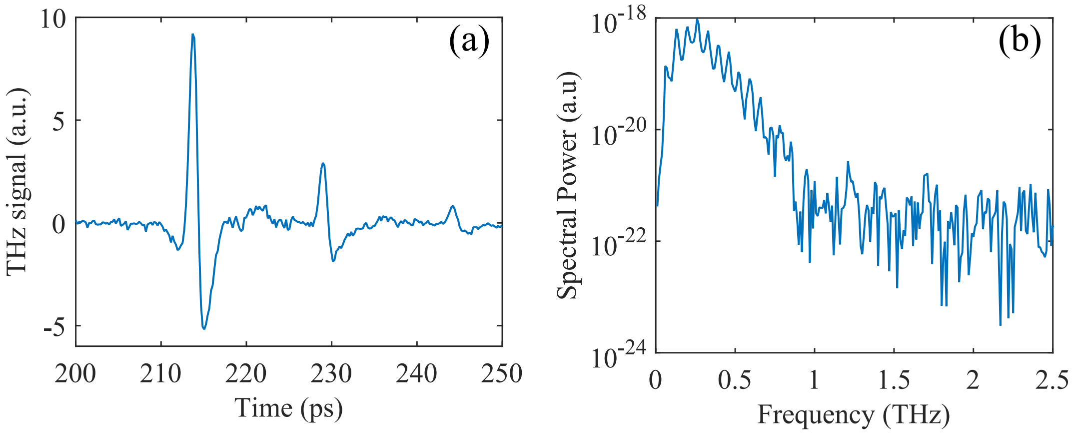

Figure 5.6: Figure (a) shows the TDS scan with the emitted THz directly focused onto the detector through manipulation of the optical pump beam. Figure (b) shows the relating frequency spectrum of the TDS trace.

optical fluence across the emitter is vastly reduced. Therefore the higher THz frequencies may be present but at much lower amplitude than the noise floor.

These results give evidence for direct focusing of THz by manipulation of the pump beam as suggested in [171]. Due to the pulse energies available with the laser it was necessary to position the emitter at a point where the optical fluence was sufficient to produce measurable THz emission and an observable focal point. With higher pulse energies available from a laser amplifier, it would be possible to use a larger IR spot size on the emitter to measure a more prominant focusing effect. With higher energies it would also be possible to perform pinhole scanning along the THz beam to determine the mode profile of the beam and also characterise the bandwidth, showing any chromatic abberations present. Such focusing could be used to develop TDS systems in which there is no need for parabolic mirrors or THz focusing lenses, as well as offering opportunities for directly focusing the emitted THz into a waveguide or QCL and tuning the focal freqeuncy to match.

5.4 Circular emitters

With recent interest in coupling of THz into waveguides it is becoming more important to take into account mode matching for efficient coupling. Several techniques have been explored for transferring free-space propagating THz into a waveguide, including using a coupling wire perpendicular to the waveguide [165, 174, 175], etched grooves in the waveguide [164] or generating the THz between the wires of a two-wire waveguide [166, 176]. This is a developing area not just for communications and data transfer, but also for improved sample measurement in TDS systems [177]. Directly matching the mode profile of the emitter to the waveguide could improve coupling losses and system efficiency. However, to develop photoconductive antenna capable of different modes and polarisations requires fabricating complex electrode arrangements to ensure no short circuits, as well as having to mask certain areas of the device to selectively prevent generation of carriers [53, 122, 165]. Without the requirement for electrical biasing or masking, DM emitters provide many possibilities for tailoring their design to meet the requirements of the waveguide.

A circular DM emitter was designed to produce radially polarised THz emission which would be optimal for coupling into a dielectric coaxial waveguide due to its symmetry [53]. The design for this emitter is shown in figure 5.7(a) where 7 µm wide overlapping rings of Au and Pb are fabricated on top of a semiconductor over a period of 21 µm. Compared to the electrode design for a circular PCA (figure 5.7(b)) the DM emitter design is much simpler and easy to fabricate and still produces radially polarised THz of the form demonstrated in (c). This device was fabricated on SI-GaAs and was characterised in a typical linear TDS setup. Due to limitations in the laser power available, the entire emitter could not be illuminated and characterised through pinhole scanning. However, TDS scans were taken over different areas of the fabricated circular DM emitter to determine if the polarisation profile was radial, as illustrated in figure 5.7(c). Figure 5.8 shows the results of these scans. Translating the pump beam spot to opposite areas of the circular emitter produces THz with opposite polarity. For positions 3 and 4 the emitter had to be rotated by 90° so that the emitted polarisation was in the same plane as the detector. If the entire emitter were to be illuminated this would produce emission with a radial polarisation. The green line in figure 5.8(b) shows the resulting TDS scan taken when illuminating the center of the circular emitter. In the far field, radial polarisation will cancel out and it is this effect that the THz-TDS system measures. The small signal we do measure is due both to non-uniformity in the semiconductor and possible slight misalignment in the setup itself. In close proximity to, or butt coupled with a dielectric coaxial waveguide the radially polarised THz generated by the circular DM emitter would be transferred into the waveguide efficiently. Coupling of photo-Dember emission

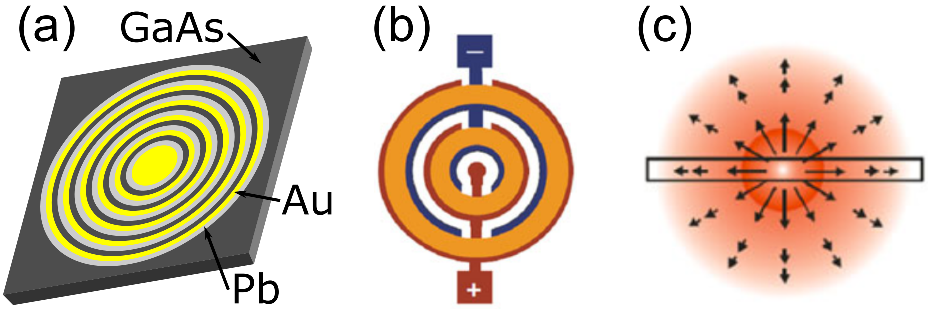

Figure 5.7: (a) shows a schematic of the circular DM emitters. Overlappping DM rings of Au (yellow) and Pb (light grey) are fabricated onto SI-GaAs (dark grey). In (b) an example of the electrode structure necessary for a photoconductive emitter to produce the same polarisation emission. (c) shows the expected polarisation mode of these emitters, with the arrows describing the direction of the THz field. (b) and (c) are taken from [53]

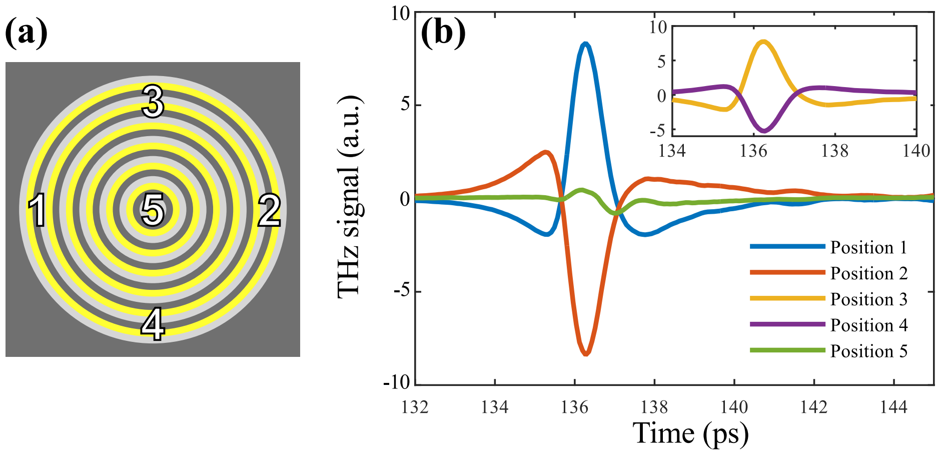

Figure 5.8: (a) shows an illustration of the points illuminated on the circular DM emitter. In (b) the results of TDS measurements taken at these respective points are shown. For opposing positions the polarity of the detected THz is seen to flip. For positions 3 and 4 (inset) the emitter had to be rotated by 90° to ensure the emitted polarisation plane was in the same axis as the detector so that a signal could be read. For the central position 5 very little signal is recorded due to opposing polarisations cancelling in the far field.

to coaxial waveguides has already been shown through near field scanning techniques. With the ease of fabrication for DM emitters it would be possible to produce designs which would generate various polarisation patterns and mode profiles. With control over the pump beam and emitter design it may also prove possible to generate circular and elliptically polarised THz.

5.5 Conclusion

In this chapter I have investigated the beam steering properties of DM emitters. I have demonstrated a simple model based on the Huygens principle of wave propagation which predicts the focusing of a THz beam through control of the phase of the excitation. I have shown experimentally with knife edge measurements that the THz beam comes to a focus at a point equal to the focal length away from the lens used to focus the pump beam. Without the need for optics to control the THz beam it is possible to focus the emitted THz directly on to the detector through pump beam manipulation. By using DM emitters which do not require a bias it is possible to position the emitter close to the detector without concern for interference from unwanted electric fields. This could enable the design of a compact spectrometer unit requiring only a laser to function, with the possibility of utilising diode lasers enabling a compact, transportable unit for THz spectroscopy.

I have fabricated a circular DM emitter and shown experimentally that the polarity of the emitted THz exhibits a radial polarisation. The DM emitter design also allows for unique structures to be fabricated, making it possible to engineer different emission polarisations and mode profiles. Using double-metal elements means there is no need for complex electrode designs or masking, so fabrication can remain simple. By tailoring the emission of THz devices and utilizing the beam steering and focusing methods, it would be possible to adapt emitters for use with waveguides for transmission of THz.

Chapter 6

Conclusion

The work presented in this thesis explores the suppression of dipoles formed from lateral diffusion currents by the presence of a metal mask and ways of enhancing devices based on this effect through multiplexing. Initially inspired by the work of Klatt *et al.*, [79, 105, 106] who demonstrated THz emission from lateral diffusion currents, through computer simulations and experimental verification Mark Barnes, Duncan McBryde and I were able to propose an alternate explanation for the LPD effect relying on suppression of dipoles due to reflection from a metal mask. In this thesis I have built upon the LPD dipole suppression theory to create multiplexed LPD devices capable of producing THz emission of comparable bandwidth and SNR to a commercial PCA.

In *chapter 2* I showed through numerical modelling the evolution of carrier diffusion and drift within a semiconductor. The model showed that no net current could be produced by diffusion alone. I then incorporated the results of this model into a finite element analysis program – COMSOL Multiphysics – to explore the effect of the metal mask on the carrier distributions. The results showed that with a metal mask present the dipole formed beneath experiences suppression due to reflection from the metal surface, whilst the uncovered dipole is free to radiate and does so on a picosecond timescale to produce THz emission perpendicular to the material surface. I showed that without a metal mask present a quadrupole emission pattern is instead observed, with no THz propagation perpendicular to the material surface. Next I showed through modelling that introduction of an insulating layer between the metal and semiconductor has little effect on the emitted THz for thicknesses significantly below the wavelength.

Next, in *chapter 3* I demonstrated a multiplex LPD emitter design consisting of periodic strips of Au deposited on the surface of a semiconductor illuminated via a cylindrical micro-lens array of period equal to that of the Au strips. I showed computationally the constructive superposition of multiple THz wavefronts for a multiplexed emitter geometry and the formation of a THz plane wave. For a fixed optical pump power the emitter is capable of producing over five times the output of a single edge LPD emitter illuminated with a single cylindrical lens. The multiplexed device showed comparable bandwidth and SNR to a commercial PCA, without the need for an applied bias. I demonstrated a simple fitting of saturation fluences for these devices which support previously published values. These emitters also show promise of further improving the output by creating a smaller period array or illuminating an increased area of their surface.

In *chapter 4* I discuss my work in conjunction with Duncan McBryde for developing an emitter which is unconstrained by the requirement for a micro-lens array. I demonstrated a double-metal LPD multiplex emitter design which utilises the difference in skin depths and Schottky barrier heights of different metals to produce THz without the need for focusing optics. I have fully investigated the temperature characteristics of the double metal emitters and have shown that the emitter which is insulated against Schottky effects demonstrates emission that follows the electron mobility temperature dependence, where as at room temperature emission is primarily Schottky driven. I have shown that the emission of DM emitters demonstrates a weak sensitivity to device angle with respect to the pump beam allowing them to be easily aligned and used as a drop-in device for existing setups. Like the single metal LPD devices in chapter 3, these emitters show good bandwidth and signal-to-noise with further scope for improvement with different metal pairings and larger pump spot sizes and fluences. DM structures patterned onto monolayer graphene were also tested, however THz emission from these devices was found to be poor. This is attributed to the low optical pump absorbtion of the graphene and the reduction of carrier mobilities for graphene when applied to a substrate.

Finally, in *chapter 5* I investigated the THz beam focusing and steering properties of DM emitters. I demonstrated a simple model based on the Huygens principle of wave propagation to show the focusing of wavefronts with an induced phase delay between them. I showed through direct knife edge measurements on the THz emission that focusing of the emitted THz beam can be controlled through manipulation of the optical pump beam. Due to the DM device not requiring a bias, the setup could be altered so that the emitter was close to the PCA detector without electrical interference. This allowed the THz emission to be focussed directly on to the detector through pump beam manipulation without any THz steering optics. This proves the concept of a possible compact THz spectroscopy system without optical components for guiding the THz beam. I fabricated circular DM emitters and showed that they were able to produce radially polarised THz emission. Control of the THz beam shape, focus and polarisation allows for enhanced coupling into waveguides through specific engineering to match mode profiles. With DM emitters fabrication remains simple and easy to tailor for various applications.

6.1 Outlook

The multiplex emitters demonstrated in this thesis have great commercial application, with similar large area devices utilising a repeating bi-metallic structure already being marketed under the name 'Terablast' by Protemics GmbH. Protemics has also filed a patent application for the device (German patent application: DE102012010926 A1) though this describes its function as solely Schottky dependent, ignoring the LPD contribution. The device is primarily marketed for near-field imaging or far-field spectroscopy applications as the lack of bias means there are no parasitic coupling effects present when aligning close to a detector. This is particularly useful for coupling directly into waveguides and, with work towards making THz-TDS systems more compact and transportable [173], these emitters will prove extremely useful. Due to their lack of bias there are no local shorting effects, allowing the emitter to continue to function if part of it becomes damaged. Photoconductive devices will always have the upper hand in terms of THz output power but LPD emitters will always find applications in areas requiring robust, bias-free, scalable operation able to match in terms of SNR.

The focusing effects explored in this thesis also contribute towards the function of the double-metal emitters. These devices can be operated as an array emitter or a point source by changing the focus of the optical pump beam. I have also shown the possibility of a lens-less setup for time-domain spectroscopy. Such a system would prove to be extremely robust and compact as the emitters need no alignment. Various metallic patterns can also be utilised to produce arbitrary output polarisation profiles without concern for electrical shorts. This allows these emitters to be designed with a specific function in mind. For instance the mode profile of the emitters can be produced to match that of a device or waveguide to improve coupling efficiency.

The use of QCLs as amplifiers for THz pulses generated by PCA's has been thoroughly investigated over the past few years [63, 64]. The future need for simplification of these systems could require the use of LPD emitters directly seeding a QCL waveguide. The multiplex DM devices presented in this thesis would be an ideal candidate for patterning directly onto the facet of a QCL, reducing the size and complexity of a Quantum Cascade Amplifier system for high power TDS. There has been a lot of recent interest towards coupling THz pulses into plasmonic waveguides for guiding [63, 107]. Beam steering and focussing will be key in efficient coupling, and work towards developing new THz optics from liquid crystals, graphene and polymers is already making headway [178–180] with a lot of recent interest in THz metasurfaces [60, 134, 181]. Furthermore, difference frequency generation (DFG) of CW THz has seen a great deal of interest over the past decade. Whilst primarily this was achieved with PCAs [69, 70] there is now a move towards passive components such as LPD emitters for coherent THz generation [182] of which the double-metal emitters would be an ideal candidate. DFG within vertical external cavity surface emitting lasers (VECSELs) is also being investigated to produce THz, as well as intracavity components for THz emission and use in TDS [183, 184].

With their robust, scalable design and a variety of applications suitable for their operation, I believe the double-metal THz emitters presented here will have a wide commercial and academic impact in the future.

Appendix A

Publications

Journal Publications

- **P. C. Gow**, D. McBryde, S. A. Berry, M. E. Barnes, and V. Apostolopoulos. "Characterisation of THz emission from double-metal-patterned gallium-arsenide multiple emitters." *Electronics Letters 50, no. 25 (2014): 1966-1968.*
- **P. Gow**, S. A. Berry, D. McBryde, M. E. Barnes, H. E. Beere, D. A. Ritchie, and V. Apostolopoulos. "Multiple lateral photo-Dember terahertz emitters illuminated by a cylindrical micro-lens array." *Applied Physics Letters, 103.25 (2013): 252101.*
- D. McBryde, **P. Gow**, S. A. Berry, M. E. Barnes, A. Aghajani, V. Apostolopoulos. "Multiple double-metal bias-free terahertz emitters" *Applied Physics Letters, 104.20 (2014): 201108.*
- M. E. Barnes, G. J. Daniell, **P. Gow**, and V. Apostolopoulos. "Simulation of Terahertz Generation from Lateral Diffusion Currents in Semiconductor Devices", *Journal of Infrared, Millimeter, and Terahertz Waves. 35.12 (2014): 1030-1044.*
- M. E. Barnes, S. A. Berry, **P. Gow**, D. McBryde, G. J. Daniell, H. E. Beere, D. A. Ritchie, V. Apostolopoulos. "Investigation of the role of the lateral photo-Dember effect in the generation of terahertz radiation using a metallic mask on a semiconductor", *Optics Express, 21.14 (2013): 16263-16272.*
- D. McBryde, M. E. Barnes, S. A. Berry, **P. Gow**, H. E. Beere, D. A. Ritchie, V. Apostolopoulos. "Fluence and polarisation dependence of GaAs based Lateral Photo-Dember terahertz emitters" *Optics Express, 22.3 (2014): 3234-3243.*

Conference Proceedings

- **P. C. Gow**, D. McBryde, S. A. Berry, M. E. Barnes, and V. Apostolopoulos, "Double-metal Schottky enhanced THz emitters.", *European Conference on Lasers* *and Electro-Optics - European Quantum Electronics Conference, (Optical Society of America, 2015)*

- **P. Gow**, S. A. Berry, D. McBryde, M. E. Barnes, H. E. Beere, D. A. Ritchie, and V. Apostolopoulos. "Multiple lateral photo-Dember terahertz emitters illuminated by a cylindrical micro-lens array.", *EOS Topical Meeting on Terahertz Science and Technology (TST 2014)*
- D. McBryde, M. E. Barnes, **P. C. Gow**, S. A. Berry, G. J. Daniell, H. E. Beere, D. A. R., and V. Apostolopoulos. "Characterisation Of Low Tempreture And Semi-insulating GaAs Lateral photo-Dember THz Emitters.", *International Conference on Infrared, Millimeter, and Terahertz Waves, 2013*
- M. E. Barnes, D. McBryde, **P. C. Gow**, S. A. Berry, G. J. Daniell, H. E. Beere, D. A. Ritchie, and V. Apostolopoulos. "Investigation Into The Role Of The Metal Mask And Pump Laser Illumination Parameters For Lateral Photo-Dember Emitters.", *International Conference on Infrared, Millimeter, and Terahertz Waves, 2013*
- M. E. Barnes, D. McBryde, S. A. Berry, **P. C. Gow**, G. J. Daniell, H. E. Beere, D. A. Ritchie, and V. Apostolopoulos. "Terahertz Emission From Lateral Surge Currents And Suppression Of dipoles Under A Metal Mask.", *International Conference on Infrared, Millimeter, and Terahertz Waves, 2013*

Bibliography

[1] T.G. Phillips and J. Keene. “Submillimeter astronomy (heterodyne spectroscopy)”. *Proceedings of the IEEE* 80.11 (1992), pp. 1662–1678 (cit. on p. 2).

[2] Frank Schwierz. “The frequency limits of field-effect transistors: MOSFET vs. HEMT”. *International Conference on Solid-State and Integrated Circuits Technology Proceedings, ICSICT* (2008), pp. 1433–1436 (cit. on p. 2).

[3] A. G. Davies, Edmund H. Linfield, and Michael B. Johnston. “The development of terahertz sources and their applications”. *Physics in Medicine and Biology* 47.21 (2002), pp. 3679–3689 (cit. on p. 2).

[4] J.C. Wiltse. “History of Millimeter and Submillimeter Waves”. *IEEE Transactions on Microwave Theory and Techniques* 32.9 (1984), pp. 1118–1127 (cit. on p. 2).

[5] D. Grischkowsky, Søren Keiding, Martin Van Exter, and Ch. Fattinger. “Far-infrared time-domain spectroscopy with terahertz beams of dielectrics and semiconductors”. *Journal of the Optical Society of America B* 7.10 (1990), p. 2006 (cit. on pp. 2, 17, 71).

[6] P.H. Siegel. “Terahertz technology”. *IEEE Transactions on Microwave Theory and Techniques* 50.3 (2002), pp. 910–928 (cit. on pp. 3, 7, 13).

[7] E. Borie. “Review of gyrotron theory”. August (1991) (cit. on p. 3).

[8] Bradley G. Whitford, Klaus J. Siemsen, Hans D. Riccius, and Kenneth A. M. Baird. “New Frequency Measurements and Techniques in the 30-THz Region”. *IEEE Transactions on Instrumentation and Measurement* 23.4 (1974), pp. 535–539 (cit. on p. 3).

[9] P. Y. Han, M. Tani, M. Usami, S. Kono, R. Kersting, and X. C. Zhang. “A direct comparison between terahertz time-domain spectroscopy and far-infrared Fourier transform spectroscopy”. *Journal of Applied Physics* 89.4 (2001), pp. 2357–2359 (cit. on p. 3).

[10] D. H. Auston. “Picosecond optoelectronic switching and gating in silicon”. *Applied Physics Letters* 26.3 (1975), pp. 101–103 (cit. on p. 3).

[11] Chi H. Lee. “Picosecond optoelectronic switching in GaAs”. *Applied Physics Letters* 30.2 (1977), p. 84 (cit. on p. 3).

[12] Tatsuo Yajima and Nobuo Takeuchi. "Spectral Properties and Tunability of Far-Infrared Difference-Frequency Radiation Produced by Picosecond Laser Pulses". *Japanese Journal of Applied Physics* 10.7 (1971), pp. 907–915 (cit. on p. 3).

[13] K. H. Yang. "Generation of Far-Infrared Radiation by Picosecond Light Pulses in LiNbO3". *Applied Physics Letters* 19.9 (1971), p. 320 (cit. on pp. 3, 11).

[14] D. H. Auston, K. P. Cheung, and P. R. Smith. "Picosecond photoconducting Hertzian dipoles". *Applied Physics Letters* 45.3 (1984), p. 284 (cit. on pp. 3, 8, 16).

[15] D. H. Auston, K. P. Cheung, J. A. Valdmanis, and D. A. Kleinman. "Cherenkov radiation from femtosecond optical pulses in electro-optic media". *Physical Review Letters* 53.16 (1984), pp. 1555–1558 (cit. on p. 3).

[16] Alfred P. DeFonzo, Madhuri Jarwala, and Charles Lutz. "Transient response of planar integrated optoelectronic antennas". *Applied Physics Letters* 50.17 (1987), p. 1155 (cit. on p. 4).

[17] M. Van Exter, Ch Fattinger, and D. Grischkowsky. "High-brightness terahertz beams characterized with an ultrafast detector". *Applied Physics Letters* 55.4 (1989), pp. 337–339 (cit. on p. 4).

[18] Masahiko Tani, Shuji Matsuura, Kiyomi Sakai, and Shin-ichi Nakashima. "Emission characteristics of photoconductive antennas based on low-temperature-grown GaAs and semi-insulating GaAs". *Applied Optics* 36.30 (1997), p. 7853 (cit. on pp. 4, 9).

[19] D. E. Spence, P. N. Kean, and W. Sibbett. "60-fsec pulse generation from a self-mode-locked Ti:sapphire laser." *Optics Letters* 16.1 (1991), pp. 42–44 (cit. on p. 4).

[20] Q. Wu and X.-C. Zhang. "Free-space electro-optic sampling of terahertz beams". *Applied Physics Letters* 67.24 (1995), p. 3523 (cit. on p. 4).

[21] P.U. Jepsen, D.G. Cooke, and M. Koch. "Terahertz spectroscopy and imaging - Modern techniques and applications". *Laser & Photonics Reviews* 5.1 (2011), pp. 124–166 (cit. on p. 5).

[22] P.H. Siegel. "Terahertz Technology in Biology and Medicine". *IEEE Transactions on Microwave Theory and Techniques* 52.10 (2004), pp. 2438–2447 (cit. on p. 5).

[23] Bryan E. Cole, Ruth M. Woodward, David A. Crawley, Vincent P. Wallace, Donald D. Arnone, and Michael Pepper. "Terahertz imaging and spectroscopy of human skin in vivo". In: ed. by Richard F. Haglund, Jr., Joseph Neev, and Richard F. Wood. Vol. 4276. 2001, pp. 1–10 (cit. on p. 5).

[24] Ruth M. Woodward, Vincent P. Wallace, Bryan E. Cole, Richard J. Pye, Donald D. Arnone, Edmund H. Linfield, and Michael Pepper. "Terahertz pulse imaging in reflection geometry of skin tissue using time-domain analysis techniques". In: ed. by Gerald E. Cohn. Vol. 47. 0. 2002, pp. 160–169 (cit. on p. 5).

[25] David Crawley, Christopher Longbottom, Vincent P Wallace, Bryan Cole, Don Arnone, and Michael Pepper. “Three-dimensional terahertz pulse imaging of dental tissue”. *Journal of Biomedical Optics* 8.2 (2003), p. 303 (cit. on p. 5).

[26] Philip F. Taday, I. V. Bradley, D. D. Arnone, and M. Pepper. “Using Terahertz pulse spectroscopy to study the crystalline structure of a drug: A case study of the polymorphs of ranitidine hydrochloride”. *Journal of Pharmaceutical Sciences* 92.4 (2003), pp. 831–838 (cit. on pp. 5, 17).

[27] Anthony J. Fitzgerald, Bryan E. Cole, and Philip F. Taday. “Nondestructive analysis of tablet coating thicknesses using Terahertz pulsed imaging”. *Journal of Pharmaceutical Sciences* 94.1 (2005), pp. 177–183 (cit. on p. 5).

[28] Joan M. Taylor, Sangeeta Tanna, and Tarsem Sahota. “In vivo study of a polymeric glucose-sensitive insulin delivery system using a rat model.” *Journal of Pharmaceutical Sciences* 99.10 (2010), pp. 4215–4227. arXiv: `z0024` (cit. on p. 6).

[29] Andrew Welch. “Full-Body Scanners: Full Protection from Terrorist Attacks or Full-On Violation of the Constitution”. *Transp. LJ* 37 (2010), p. 167 (cit. on p. 6).

[30] A. W. M. Lee, B. S. Williams, Sushil Kumar, Qing Hu, and J. L. Reno. “Real-time imaging using a 4.3-THz quantum cascade laser and a 320 /spl times/ 240 microbolometer focal-plane array”. *IEEE Photonics Technology Letters* 18.13 (2006), pp. 1415–1417 (cit. on pp. 6, 7).

[31] Hua Zhong, Jingzhou Xu, Xu Xie, Tao Yuan, Ron Reightler, Eric Madaras, and Xi Cheng Zhang. “Nondestructive defect identification with terahertz time-of-flight tomography”. *IEEE Sensors Journal* 5.2 (2005), pp. 203–207 (cit. on p. 6).

[32] Naoto Nagai, Masakiyo Sumitomo, Mitsuru Imaizumi, and Ryoichi Fukasawa. “Characterization of electron- or proton-irradiated Si space solar cells by THz spectroscopy”. *Semiconductor Science and Technology* 21.2 (2006), pp. 201–209 (cit. on pp. 6, 17).

[33] Naoto Nagai and Ryoichi Fukasawa. “Abnormal dispersion of polymer films in the THz frequency region”. *Chemical Physics Letters* 388.4-6 (2004), pp. 479–482 (cit. on p. 6).

[34] Naoto Nagai, Tomoko Imai, Ryoichi Fukasawa, Koya Kato, and Koji Yamauchi. “Analysis of the intermolecular interaction of nanocomposites by THz spectroscopy”. *Applied Physics Letters* 85.18 (2004), p. 4010 (cit. on p. 6).

[35] M. Misra, K. Kotani, I. Kawayama, H. Murakami, and M. Tonouchi. “Observation of TO1 soft mode in $SrTiO_3$ films by terahertz time domain spectroscopy”. *Applied Physics Letters* 87.18 (2005), p. 2909 (cit. on p. 6).

[36] Jonas D. Buron, David M. A. Mackenzie, Dirch. H. Petersen, Amaia Pesquera, Alba Centeno, Peter Bøggild, Amaia Zurutuza, and Peter U. Jepsen. “Terahertz wafer-scale mobility mapping of graphene on insulating substrates without a gate”. *Optics Express* 23.24 (2015), p. 30721 (cit. on p. 6).

[37] Takeshi Yasui, Takashi Yasuda, Ken-ichi Sawanaka, and Tsutomu Araki. "Terahertz paintmeter for noncontact monitoring of thickness and drying progress in paint film". *Applied Optics* 44.32 (2005), p. 6849 (cit. on pp. 6, 18).

[38] Masayoshi Tonouchi. "Cutting-edge terahertz technology". *Nature Photonics* 1.2 (2007), pp. 97–105 (cit. on pp. 6, 13).

[39] S. Koenig, D. Lopez-Diaz, J. Antes, F. Boes, R. Henneberger, A. Leuther, A. Tessmann, R. Schmogrow, D. Hillerkuss, R. Palmer, T. Zwick, C. Koos, W. Freude, O. Ambacher, J. Leuthold, and I. Kallfass. "Wireless sub-THz communication system with high data rate". *Nature Photonics* 7.12 (2013), pp. 977–981 (cit. on p. 7).

[40] Jianjun Yu, Xinying Li, and Nan Chi. "Faster than fiber: over 100-Gb/s signal delivery in fiber wireless integration system". *Optics Express* 21.19 (2013), p. 22885 (cit. on p. 7).

[41] David T. Leisawitz, William C. Danchi, Michael J. DiPirro, Lee D. Feinberg, Daniel Y. Gezari, Mike Hagopian, William D Langer, John C Mather, Samuel H. Moseley, Jr., Michael Shao, Robert F. Silverberg, Johannes G. Staguhn, Mark R Swain, Harold W Yorke, and Xiaolei Zhang. "Scientific motivation and technology requirements for the SPIRIT and SPECS far-infraredisubmillimeter space interferometers". *UV, Optical, and IR Space Telescopes and Instruments* 4013 (2000), pp. 36–46 (cit. on p. 7).

[42] B. B. Hu and M. C. Nuss. "Imaging with terahertz waves". *Optics Letters* 20.16 (1995), p. 1716 (cit. on p. 7).

[43] N. Rothbart, H. Richter, M. Wienold, L. Schrottke, H. T. Grahn, and H. W. Hübers. "Fast terahertz computed-tomography imaging with a quantum-cascade laser and a scanning mirror". *International Conference on Infrared, Millimeter, and Terahertz Waves, IRMMW-THz* 3.5 (2013), pp. 617–624 (cit. on p. 7).

[44] Hani Sherry, Janusz Grzyb, Yan Zhao, Richard Al Hadi, Andreia Cathelin, Andreas Kaiser, and Ullrich Pfeiffer. "A 1kpixel CMOS camera chip for 25fps real-time terahertz imaging applications". *Digest of Technical Papers - IEEE International Solid-State Circuits Conference* 55.March 2011 (2012), pp. 252–253 (cit. on p. 7).

[45] Daniela Pinna, Monica Galeotti, and Rocco Mazzeo. *Scientific examination for the investigation of paintings: a handbook for conservator-restorers*. Centro Di, 2009 (cit. on p. 7).

[46] Kaori Fukunaga, Iwao Hosako, Marcello Picollo, and Yohsei Kohdzuma. "Application of THz sensing to analysis of works of art for conservation". *Proceedings - 2010 IEEE International Topical Meeting on Microwave Photonics, MWP 2010* 2 (2010), pp. 147–150 (cit. on pp. 7, 17).

[47] Bianca J. Jackson, Marie R. Mourou, John F. Whitaker, Irl N. Duling III, Steve L. Williamson, Michel Menu, and Gerard Mourou. "Terahertz time-domain reflectometry applied to the investigation of hidden mural paintings". In: Optical Society of America. 2008 (cit. on p. 7).

[48] P.R. Smith, D.H. Auston, and M.C. Nuss. "Subpicosecond photoconducting dipole antennas". *IEEE Journal of Quantum Electronics* 24.2 (1988), pp. 255–260 (cit. on p. 8).

[49] N Katzenellenbogen and D Grischkowsky. "Efficient generation of 380 fs pulses of THz radiation by ultrafast laser pulse excitation of a biased metal-semiconductor interface". *Applied Physics Letters* 58.3 (1991), p. 222 (cit. on p. 8).

[50] Jie Shan and Tony F Heinz. *Terahertz Radiation from Semiconductors*. Vol. 59. 2004, pp. 1–56 (cit. on pp. 8, 13).

[51] Colin Baker. "Development of Semiconductor Materials for Terahertz Photoconductive Antennas". *PhD Thesis, University of Cambridge* (2004) (cit. on pp. 8, 30).

[52] Abhishek Singh, Nilesh Awari, S. S. Prabhu, and a. S. Vengurlekar. "THz from photoconductive antennas using circular and cylindrical microlens arrays". In: *2011 International Conference on Infrared, Millimeter, and Terahertz Waves*. IEEE, 2011, pp. 1–2 (cit. on p. 9).

[53] Stephan Winnerl. "Scalable Microstructured Photoconductive Terahertz Emitters". *Journal of Infrared, Millimeter, and Terahertz Waves* 33.4 (2011), pp. 431–454 (cit. on pp. 9, 39, 52, 82).

[54] C.W. Berry, N Wang, M.R. Hashemi, M Unlu, and M Jarrahi. "Significant performance enhancement in photoconductive terahertz optoelectronics by incorporating plasmonic contact electrodes". *Nature Communications* 4.1 (2013), p. 1622 (cit. on p. 9).

[55] Jerome Faist, Federico Capasso, Deborah L Sivco, Carlo Sirtori, A. L. Hutchinson, and A. Y. Cho. "Quantum Cascade Laser". *Science* 264.5158 (1994), pp. 553–556 (cit. on p. 9).

[56] G. Scalari, C. Walther, M. Fischer, R. Terazzi, H. Beere, D. Ritchie, and J. Faist. "THz and sub-THz quantum cascade lasers". *Laser & Photonics Review* 3.1-2 (2009), pp. 45–66 (cit. on p. 9).

[57] Hyunyong Choi, Laurent Diehl, Zong-Kwei Wu, Marcella Giovannini, Jérôme Faist, Federico Capasso, and Theodore Norris. "Gain Recovery Dynamics and Photon-Driven Transport in Quantum Cascade Lasers". *Physical Review Letters* 100.16 (2008), p. 167401 (cit. on p. 9).

[58] Christine Y. Wang, L. Diehl, A. Gordon, C. Jirauschek, F. X. Kärtner, A. Belyanin, D. Bour, S. Corzine, G. Höfler, M. Troccoli, J. Faist, and F. Capasso. “Coherent instabilities in a semiconductor laser with fast gain recovery”. *Physical Review A* 75.3 (2007), p. 031802 (cit. on p. 9).

[59] Benjamin S. Williams, Sushil Kumar, Hans Callebaut, Qing Hu, and John L. Reno. “Terahertz quantum-cascade laser operating up to 137 K”. *Applied Physics Letters* 83.25 (2003), p. 5142 (cit. on p. 10).

[60] Nanfang Yu, Qi Jie Wang, Mikhail A. Kats, Jonathan A. Fan, Suraj P. Khanna, Lianhe Li, Giles A. Davies, Edmund H. Linfield, and F. Capasso. “Designer spoof surface plasmon structures collimate terahertz laser beams”. *Nature Materials* 9.9 (2010), pp. 730–735 (cit. on pp. 10, 76, 87).

[61] R. Wallis, R. Degl’Innocenti, D. S. Jessop, Y. Ren, A. Klimont, Y. D. Shah, O. Mitrofanov, C. M. Bledt, J. E. Melzer, J. A. Harrington, H. E. Beere, and D. A. Ritchie. “Efficient coupling of double-metal terahertz quantum cascade lasers to flexible dielectric-lined hollow metallic waveguides”. *Optics Express* 23.20 (2015), p. 26276 (cit. on pp. 10, 76).

[62] A. Valavanis, Jingxuan Zhu, J. Freeman, Lianhe Li, Li Chen, A.G. Davies, E.H. Linfield, and P. Dean. “Terahertz quantum cascade lasers with >1 W output powers”. *Electronics Letters* 50.4 (2014), pp. 309–311 (cit. on p. 10).

[63] J. Maysonnave, N. Jukam, M. S. M. Ibrahim, K. Maussang, J. Madéo, P. Cavalié, P. Dean, S. P. Khanna, D. P. Steenson, E. H. Linfield, A. G. Davies, J. Tignon, and S. S. Dhillon. “Integrated injection seeded terahertz source and amplifier for time-domain spectroscopy”. *Optics Letters* 37.4 (2012), p. 731 (cit. on pp. 10, 87).

[64] Dominic Bachmann, Norbert Leder, Markus Rösch, Giacomo Scalari, Mattias Beck, Holger Arthaber, Jérôme Faist, Karl Unterrainer, and Juraj Darmo. “Broadband terahertz amplification in a heterogeneous quantum cascade laser”. *Optics Express* 23.3 (2015), p. 3117 (cit. on pp. 10, 87).

[65] L. Xu, X. C. Zhang, and D. H. Auston. “Terahertz beam generation by femtosecond optical pulses in electro-optic materials”. *Applied Physics Letters* 61.15 (1992), pp. 1784–1786 (cit. on p. 11).

[66] Gopakumar Ramakrishnan and Paul C. M. Planken. “Percolation-enhanced generation of terahertz pulses by optical rectification on ultrathin gold films”. *Optics Letters* 36.13 (2011), p. 2572 (cit. on p. 11).

[67] E. R. Brown, F. W. Smith, and K. A. McIntosh. “Coherent millimeter-wave generation by heterodyne conversion in low-temperature-grown GaAs photoconductors”. *Journal of Applied Physics* 73.3 (1993), p. 1480 (cit. on p. 11).

[68] E. R. Brown, K. A. McIntosh, F. W. Smith, M. J. Manfra, and C. L. Dennis. “Measurements of optical-heterodyne conversion in low-temperature-grown GaAs”. *Applied Physics Letters* 62.1993 (1993), pp. 1206–1208 (cit. on p. 11).

[69] Masahiko Tani, Osamu Morikawa, Shuji Matsuura, and Masanori Hangyo. “Generation of terahertz radiation by photomixing with dual- and multiple-mode lasers”. *Semiconductor Science and Technology* 20.7 (2005), S151–S163 (cit. on pp. 11, 87).

[70] S.-H. Yang, R. Watts, X. Li, N. Wang, V. Cojocaru, J. O’Gorman, L. P. Barry, and M. Jarrahi. “Tunable terahertz wave generation through a bimodal laser diode and plasmonic photomixer”. *Optics Express* 23.24 (2015), p. 31206 (cit. on pp. 11, 87).

[71] Mikhail A. Belkin, Federico Capasso, Alexey Belyanin, Deborah L. Sivco, Alfred Y. Cho, Douglas C. Oakley, Christopher J. Vineis, and George W. Turner. “Terahertz quantum-cascade-laser source based on intracavity difference-frequency generation”. *Nature Photonics* 1.5 (2007), pp. 288–292 (cit. on p. 11).

[72] M. B. Johnston, D. M. Whittaker, A. Corchia, A. G. Davies, and E. H. Linfield. “Simulation of terahertz generation at semiconductor surfaces”. *Physical Review B* 65.16 (2002), p. 165301 (cit. on pp. 12, 13).

[73] Vitalij L. Malevich, Ramunas Adomavičius, and Arunas Krotkus. “THz emission from semiconductor surfaces”. *Comptes Rendus Physique* 9.2 (2008), pp. 130–141 (cit. on p. 12).

[74] X.-C. Zhang, B. B. Hu, J. T. Darrow, and D. H. Auston. “Generation of femtosecond electromagnetic pulses from semiconductor surfaces”. *Applied Physics Letters* 56.11 (1990), p. 1011 (cit. on pp. 12, 55, 64).

[75] J. N. Heyman, N. Coates, a. Reinhardt, and G. Strasser. “Diffusion and drift in terahertz emission at GaAs surfaces”. *Applied Physics Letters* 83.26 (2003), p. 5476 (cit. on p. 12).

[76] Antanas Reklaitis. “Crossover between surface field and photo-Dember effect induced terahertz emission”. *Journal of Applied Physics* 109.8 (2011), pp. 8–12 (cit. on p. 12).

[77] H. Dember. “Uber eine photoelektronische Kraft in Kupferoxydul-Kristallen”. *Z. Phys* 32 (1931), p. 554 (cit. on p. 12).

[78] T Dekorsy, T Pfeifer, W Kütt, and H Kurz. “Subpicosecond carrier transport in GaAs surface-space-charge fields”. *Physical Review B* 47.7 (1993), pp. 3842–3849 (cit. on pp. 12, 29, 30).

[79] G. Klatt, D. Stephan, M. Beck, J. Demsar, and T. Dekorsy. “Large-area laser-driven terahertz emitters”. *Electronics Letters* 46.26 (2010), S24 (cit. on pp. 12, 19, 39, 40, 85).

[80] Yu. A. Goldberg and N. M. Schmidt. “Handbook series on semiconductor parameters”. *vol* 1 (1999), pp. 191–213 (cit. on p. 12).

[81] J. S. Blakemore. “Semiconducting and other major properties of gallium arsenide”. *Journal of Applied Physics* 53.10 (1982), R123 (cit. on p. 13).

[82] Kai Liu, Jingzhou Xu, Tao Yuan, and X. C. Zhang. “Terahertz radiation from InAs induced by carrier diffusion and drift”. *Physical Review B - Condensed Matter and Materials Physics* 73.15 (2006), pp. 1–6 (cit. on pp. 13, 29, 30).

[83] Ping Gu, Masahiko Tani, Shunsuke Kono, Kiyomi Sakai, and X. C. Zhang. “Study of terahertz radiation from InAs and InSb”. *Journal of Applied Physics* 91.9 (2002), pp. 5533–5537 (cit. on p. 13).

[84] Kotaro Kajikawa, Yusuke Nagai, Yuichi Uchiho, Gopakumar Ramakrishnan, Nishant Kumar, Gopika K. P. Ramanandan, and Paul C. M. Planken. “Terahertz emission from surface-immobilized gold nanospheres”. *Optics Letters* 37.19 (2012), p. 4053 (cit. on p. 13).

[85] E. Beaurepaire, G. M. Turner, S. M. Harrel, M. C. Beard, J.-Y. Bigot, and C. A. Schmuttenmaer. “Coherent terahertz emission from ferromagnetic films excited by femtosecond laser pulses”. *Applied Physics Letters* 84.18 (2004), p. 3465 (cit. on pp. 13, 70).

[86] H. Ahn, Y. P. Ku, Y. C. Wang, C. H. Chuang, S. Gwo, and Ci Ling Pan. “Terahertz emission from vertically aligned InN nanorod arrays”. *Applied Physics Letters* 91.13 (2007), pp. 1–4 (cit. on pp. 13, 70).

[87] Ch. Fattinger and D. Grischkowsky. “Point source terahertz optics”. *Applied Physics Letters* 53.16 (1988), p. 1480 (cit. on p. 14).

[88] J. Valdmanis and G. Mourou. “Subpicosecond electrooptic sampling: Principles and applications”. *IEEE Journal of Quantum Electronics* 22.January (1986), pp. 69–78 (cit. on p. 15).

[89] Paul A. Elzinga, Ronald J. Kneisler, Fred E. Lytle, Yanan Jiang, Galen B. King, and Normand M. Laurendeau. “Pump/probe method for fast analysis of visible spectral signatures utilizing asynchronous optical sampling”. *Applied Optics* 26.19 (1987), p. 4303 (cit. on pp. 15, 16).

[90] Y. Nakagawa and H. Yoshinaga. “Characteristics of High-Sensitivity Ge Bolometer”. *Japanese Journal of Applied Physics* 9.4 (1970), 427B–427B (cit. on p. 15).

[91] M. J. Malachowski and J. Zmija. “Organic field-effect transistors”. *Opto-Electronics Review* 18.2 (2010), pp. 121–136 (cit. on p. 15).

[92] Kevin C. Liddiard. “The active microbolometer: a new concept in infrared detection”. *Proceedings of SPIE* 5274 (2004), pp. 227–238 (cit. on p. 15).

[93] Marcel J. E. Golay. “Theoretical Consideration in Heat and Infra-Red Detection, with Particular Reference to the Pneumatic Detector”. *Review of Scientific Instruments* 18.5 (1947), p. 347 (cit. on p. 16).

[94] J. R. Hickey. “Modified Optical System for the Golay Detector”. *Review of Scientific Instruments* 40.5 (1969), p. 732 (cit. on p. 16).

[95] A. Bartels, R. Cerna, C. Kistner, A. Thoma, F. Hudert, C. Janke, and T. Dekorsy. "Ultrafast time-domain spectroscopy based on high-speed asynchronous optical sampling". *Review of Scientific Instruments* 78.3 (2007), p. 035107 (cit. on p. 16).

[96] Hai-Bo Liu, Yunqing Chen, Glenn J. Bastiaans, and X-C Zhang. "Detection and identification of explosive RDX by THz diffuse reflection spectroscopy". *Optics Express* 14.1 (2006), p. 415 (cit. on p. 17).

[97] Aaron L. Chung. "Material parameter extraction in terahertz time domain spectroscopy". *PhD thesis. University of Southampton* (2012) (cit. on p. 17).

[98] Callum J. Docherty, Patrick Parkinson, Hannah J. Joyce, Ming-Hui Chiu, Chang-Hsiao Chen, Ming-Yang Lee, Lain-Jong Li, Laura M Herz, and Michael B. Johnston. "Ultrafast Transient Terahertz Conductivity of Monolayer MoS_2 and WSe_2 Grown by Chemical Vapor Deposition". *ACS nano* 8.11 (2014), pp. 11147–11153 (cit. on p. 17).

[99] Hannah J. Joyce, Patrick Parkinson, Nian Jiang, Callum J. Docherty, Qiang Gao, H. Hoe Tan, Chennupati Jagadish, Laura M. Herz, and Michael B. Johnston. "Electron Mobilities Approaching Bulk Limits in Surface-Free GaAs Nanowires". *Nano letters* 14.10 (2014), pp. 5989–5994 (cit. on p. 17).

[100] Qingli Zhou, Yulei Shi, Tong Li, Bin Jin, Dongmei Zhao, and Cunlin Zhang. "Carrier dynamics and terahertz photoconductivity of doped silicon measured by femtosecond pump-terahertz probe spectroscopy". *Science in China, Series G: Physics, Mechanics and Astronomy* 52.12 (2009), pp. 1944–1948 (cit. on p. 17).

[101] Andrew Jameson, Joseph Tomaino, and Yun-Shik Lee. "Transient optical response of quantum well excitons to intense narrowband terahertz pulses". In: *APS Meeting Abstracts*. Vol. 1. 2010, p. 25004 (cit. on p. 17).

[102] H. P. Porte, P. Uhd Jepsen, N. Daghestani, E. U. Rafailov, and D. Turchinovich. "Ultrafast release and capture of carriers in InGaAs/GaAs quantum dots observed by time-resolved terahertz spectroscopy". *Applied Physics Letters* 94.26 (2009), pp. 2007–2010 (cit. on p. 17).

[103] Matthew C. Beard, Gordon M. Turner, and Charles A. Schmuttenmaer. "Size-Dependent Photoconductivity in CdSe Nanoparticles as Measured by Time-Resolved Terahertz Spectroscopy". *Nano Letters* 2.9 (2002), pp. 983–987 (cit. on p. 17).

[104] Syed B. Qadri, Dong H. Wu, Benjamin D. Graber, Nadeemullah A. Mahadik, and Anthony Garzarella. "Failure mechanism of THz GaAs photoconductive antenna". *Applied Physics Letters* 101.1 (2012), p. 011910 (cit. on pp. 18, 46).

[105] G. Klatt, F. Hilser, W. Qiao, M. Beck, R. Gebs, A. Bartels, K. Huska, U. Lemmer, G. Bastian, M.B. Johnston, M. Fischer, J. Faist, and T. Dekorsy. "Terahertz emission from lateral photo-Dember currents". *Optics Express* 18.5 (2010), p. 4939 (cit. on pp. 19, 27, 85).

[106] G. Klatt, B. Surrer, D. Stephan, O. Schubert, M. Fischer, J. Faist, A. Leitenstorfer, R. Huber, and T. Dekorsy. "Photo-Dember terahertz emitter excited with an Er:fiber laser". *Applied Physics Letters* 98.2 (2011), p. 021114 (cit. on pp. 19, 40, 52, 53, 85).

[107] W. Qiao, D. Stephan, M. Hasselbeck, Q. Liang, and T. Dekorsy. "Low-temperature THz time domain waveguide spectrometer with butt-coupled emitter and detector crystal". *Optics Express* 20.18 (2012), p. 19769 (cit. on pp. 20, 87).

[108] Duncan McBryde, Mark E. Barnes, Geoff J. Daniell, Aaron L. Chung, Zakaria Mihoubi, Adrian H. Quarterman, Keith G. Wilcox, Anne C. Tropper, and Vasilis Apostolopoulos. "Simulation of metallic nanostructures for emission of THz radiation using the lateral photo-Dember effect". *Proceedings of the 36th International Conference on Infrared, Milimeter and Terahertz Waves (IRMMW-THz), Houston, USA* (2011), pp. 1–2 (cit. on pp. 20, 40).

[109] M. E. Barnes, D. McBryde, G. J. Daniell, G. Whitworth, A. L. Chung, A. H. Quarterman, K. G. Wilcox, A. Brewer, H. E. Beere, D. A. Ritchie, and V. Apostolopoulos. "Terahertz emission by diffusion of carriers and metal-mask dipole inhibition of radiation". *Optics Express* 20.8 (2012), p. 8898 (cit. on pp. 20, 28, 29, 52).

[110] M. E. Barnes, S. A. Berry, P. Gow, D. McBryde, G. J. Daniell, H. E. Beere, D. A. Ritchie, and V. Apostolopoulos. "Investigation of the role of the lateral photo-Dember effect in the generation of terahertz radiation using a metallic mask on a semiconductor". *Optics Express* 21.14 (2013), p. 16263 (cit. on pp. 21, 23, 25, 27, 49, 52).

[111] Mark A. Ordal, Robert J. Bell, Ralph W. Alexander, Larry L. Long, and Marvin R. Querry. "Optical properties of Au, Ni, and Pb at submillimeter wavelengths". *Applied Optics* 26.4 (1987), p. 744 (cit. on p. 23).

[112] KH Drexhage. "Influence of a dielectric interface on fluorescence decay time". *Journal of Luminescence* 1 (1970), pp. 693–701 (cit. on p. 23).

[113] Mark E. Barnes, Geoff J. Daniell, Paul Gow, and Vasilis Apostolopoulos. "Simulation of Terahertz Generation from Lateral Diffusion Currents in Semiconductor Devices". *Journal of Infrared, Millimeter, and Terahertz Waves* 35.12 (2014), pp. 1030–1044 (cit. on pp. 23, 25, 27, 34, 52).

[114] P. Gow, S. A. Berry, D. McBryde, M. E. Barnes, H. E. Beere, D. A. Ritchie, and V. Apostolopoulos. "Multiple lateral photo-Dember terahertz emitters illuminated by a cylindrical micro-lens array". *Applied Physics Letters* 103.25 (2013), p. 252101 (cit. on pp. 24, 25, 39).

[115] D. McBryde, M. E. Barnes, S. A. Berry, P. Gow, H. E. Beere, D. A. Ritchie, and V. Apostolopoulos. “Fluence and polarisation dependence of GaAs based Lateral Photo-Dember terahertz emitters”. *Optics Express* 22.3 (2014), p. 3234 (cit. on pp. 25, 45, 49, 55, 59, 60, 68).

[116] D. McBryde, P. Gow, S. A. Berry, M. E. Barnes, A. Aghajani, and V. Apostolopoulos. “Multiple double-metal bias-free terahertz emitters”. *Applied Physics Letters* 104.20 (2014), p. 201108 (cit. on pp. 25, 51, 64).

[117] P. C. Gow, D. McBryde, S. A. Berry, M. E. Barnes, and V. Apostolopoulos. “Characterisation of THz emission from double-metal-patterned galliumarsenide multiple emitters”. *Electronics Letters* 50.25 (2014), pp. 1966–1968 (cit. on pp. 25, 26, 51).

[118] I. S. Gregory, W. R. Tribe, C. Baker, B. E. Cole, M. J. Evans, L. Spencer, M. Pepper, and M. Missous. “Continuous-wave terahertz system with a 60 dB dynamic range”. *Applied Physics Letters* 86.20 (2005), p. 204104 (cit. on p. 30).

[119] Ian S. Gregory. “The development of a continuous-wave terahertz imaging system”. *PhD Thesis, University of Cambridge* December (2004) (cit. on p. 30).

[120] G. Rodriguez, S. R. Caceres, and A. J. Taylor. “Modeling of terahertz radiation from biased photoconductors: transient velocity effects”. *Optics Letters* 19.23 (1994), p. 1994 (cit. on p. 32).

[121] Tomonori Nishimura, Koji Kita, and Akira Toriumi. “A Significant Shift of Schottky Barrier Heights at Strongly Pinned Metal/Germanium Interface by Inserting an Ultra-Thin Insulating Film”. *Applied Physics Express* 1 (2008), p. 051406 (cit. on pp. 38, 57, 69).

[122] A. Dreyhaupt, S. Winnerl, T. Dekorsy, and M. Helm. “High-intensity terahertz radiation from a microstructured large-area photoconductor”. *Applied Physics Letters* 86.12 (2005), p. 121114 (cit. on pp. 39, 51, 82).

[123] Duncan McBryde, Mark E. Barnes, Paul C. Gow, Sam A. Berry, Geoff J. Daniell, Harvey E. Beere, David A. Ritchie, and Vasilis Apostolopoulos. “Characterisation of low temperature and semi-insulating GaAs lateral photo-dember THz emitters”. In: *2013 38th International Conference on Infrared, Millimeter, and Terahertz Waves (IRMMW-THz)*. Mainz, Germany: IEEE, 2013, pp. 1–2 (cit. on p. 45).

[124] P. G. Huggard, C. J. Shaw, J. A. Cluff, and S. R. Andrews. “Polarization-dependent efficiency of photoconducting THz transmitters and receivers”. *Applied Physics Letters* 72.17 (1998), p. 2069 (cit. on p. 45).

[125] Elmer S. Estacio, Masakazu Hibi, Katsuya Saito, Christopher T. Que, Takashi Furuya, Fumiaki Miyamaru, Seizi Nishizawa, Kohji Yamamoto, and Masahiko Tani. “Saturation and Polarization Characteristics of 1.56 μm Optical Probe Pulses in a LTG-GaAs Photoconductive Antenna Terahertz Detector”. *Proceedings of*

the 38th International Conference on Infrared, Milimeter and Terahertz Waves (IRMMW-THz), Mainz, Germany Mainz, Germany (2013) (cit. on p. 45).

[126] André Vander Vorst, Arye Rosen, and Youji Kotsuka. *RF/microwave interaction with biological tissues.* Vol. 181. John Wiley & Sons, 2006, p. 255 (cit. on p. 54).

[127] Ranjan Singh, Evgenya Smirnova, Antoinette J. Taylor, John F. O'Hara, and Weili Zhang. "Optically thin terahertz metamaterials". *Optics Express* 16.9 (2008), p. 6537 (cit. on pp. 55, 64, 65).

[128] Yulei Shi, Yuping Yang, Xinlong Xu, Shihua Ma, Wei Yan, and Li Wang. "Ultrafast carrier dynamics in Au/GaAs interfaces studied by terahertz emission spectroscopy". *Applied Physics Letters* 88.16 (2006), p. 161109 (cit. on pp. 55, 60).

[129] W. G. Spitzer and C. A. Mead. "Barrier height studies on metal-semiconductor systems". *Journal of Applied Physics* 34.10 (1963), pp. 3061–3069 (cit. on p. 56).

[130] C. A. Mead and W. G. Spitzer. "Fermi Level Position at Metal-Semiconductor Interfaces". *Physical Review* 134.3A (1964), A713–A716 (cit. on p. 56).

[131] J. R. Waldrop. "Schottky-barrier height of ideal metal contacts to GaAs". *Applied Physics Letters* 44.10 (1984), pp. 1002–1004 (cit. on p. 56).

[132] John Bardeen. "Surface States and Rectification at a Metal Semi-Conductor Contact". *Physical Review* 71.10 (1947), pp. 717–727 (cit. on pp. 56, 65).

[133] Gopakumar Ramakrishnan, Nishant Kumar, Gopika K P Ramanandan, Aurèle J L Adam, Ruud W A Hendrikx, and Paul C M Planken. "Plasmon-enhanced terahertz emission from a semiconductor/metal interface". *Applied Physics Letters* 104.7 (2014), p. 071104 (cit. on p. 56).

[134] Afshin Jooshesh, Levi Smith, Mostafa Masnadi-Shirazi, Vahid Bahrami-Yekta, Thomas Tiedje, Thomas E. Darcie, and Reuven Gordon. "Nanoplasmonics enhanced terahertz sources". *Optics Express* 22.23 (2014), p. 27992 (cit. on pp. 56, 87).

[135] C. M. Wolfe. "Electron Mobility in High-Purity GaAs". *Journal of Applied Physics* 41.7 (1970), p. 3088 (cit. on p. 64).

[136] M. K. Hudait, P. Venkateswarlu, and S. B. Krupanidhi. "Electrical transport characteristics of Au/n-GaAs Schottky diodes on n-Ge at low temperatures". *Solid-State Electronics* 45.1 (2001), pp. 133–141 (cit. on p. 64).

[137] J. Lloyd-Hughes, S. K. E. Merchant, L. Fu, H. H. Tan, C. Jagadish, E. Castro-Camus, and M. B. Johnston. "Influence of surface passivation on ultrafast carrier dynamics and terahertz radiation generation in GaAs". *Applied Physics Letters* 89.23 (2006), p. 232102 (cit. on p. 65).

[138] M. Nakajima, M. Hangyo, M. Ohta, and H. Miyazaki. "Polarity reversal of terahertz waves radiated from semi-insulating InP surfaces induced by temperature". *Physical Review B* 67.19 (2003), p. 195308 (cit. on p. 69).

[139] P. Hoyer, M. Theuer, R. Beigang, and E. B. Kley. “Terahertz emission from black silicon”. *Applied Physics Letters* 93.9 (2008), pp. 1–4 (cit. on p. 70).

[140] M. Nagel, A. Michalski, T. Botzem, and H. Kurz. “Near-field investigation of THz surface-wave emission from optically excited graphite flakes”. *Optics Express* 19.5 (2011), p. 4667 (cit. on p. 70).

[141] Gopakumar Ramakrishnan, Reshmi Chakkittakandy, and Paul C. M. Planken. “THz generation from graphite”. In: *2009 34th International Conference on Infrared, Millimeter, and Terahertz Waves*. Vol. 17. 18. IEEE, 2009, pp. 1–2 (cit. on p. 70).

[142] Xu Du, Ivan Skachko, Anthony Barker, and Eva Y. Andrei. “Approaching ballistic transport in suspended graphene”. *Nature Nanotechnology* 3.8 (2008), pp. 491–495 (cit. on p. 70).

[143] Phaedon Avouris. “Graphene: Electronic and photonic properties and devices”. *Nano Letters* 10.11 (2010), pp. 4285–4294 (cit. on p. 70).

[144] Callum J. Docherty and Michael B. Johnston. “Terahertz Properties of Graphene”. *Journal of Infrared, Millimeter, and Terahertz Waves* 33.8 (2012), pp. 797–815 (cit. on p. 70).

[145] Hugen Yan, Zhiqiang Li, Xuesong Li, Wenjuan Zhu, Phaedon Avouris, and Fengnian Xia. “Infrared spectroscopy of tunable Dirac terahertz magneto-plasmons in graphene.” *Nano letters* 12.7 (2012), pp. 3766–71 (cit. on p. 70).

[146] Rasoul Alaee, Mohamed Farhat, Carsten Rockstuhl, and Falk Lederer. “A perfect absorber made of a graphene micro-ribbon metamaterial”. *Optics Express* 20.27 (2012), p. 28017 (cit. on p. 70).

[147] Fengnian Xia, Thomas Mueller, Yu-Ming Lin, Alberto Valdes-Garcia, and Phaedon Avouris. “Ultrafast graphene photodetector”. *Nature Nanotechnology* 4.12 (2009), pp. 839–843 (cit. on p. 70).

[148] Bing-Zheng Xu, Chang-Qing Gu, Zhuo Li, and Zhen-Yi Niu. “A novel structure for tunable terahertz absorber based on graphene”. *Optics Express* 21.20 (2013), p. 23803 (cit. on p. 70).

[149] Andrei Andryieuski and Andrei V. Lavrinenko. “Graphene metamaterials based tunable terahertz absorber: effective surface conductivity approach”. *Optics Express* 21.7 (2013), p. 9144 (cit. on pp. 70, 76).

[150] Tony Low and Phaedon Avouris. “Graphene plasmonics for terahertz to mid-infrared applications.” *ACS nano* 8.2 (2014), pp. 1086–101 (cit. on p. 70).

[151] Long Ju, Baisong Geng, Jason Horng, Caglar Girit, Michael Martin, Zhao Hao, Hans a Bechtel, Xiaogan Liang, Alex Zettl, Y Ron Shen, and Feng Wang. “Graphene plasmonics for tunable terahertz metamaterials”. *Nature Nanotechnology* 6.10 (2011), pp. 630–634 (cit. on p. 70).

[152] M. V. Entin, L. I. Magarill, and D. L. Shepelyansky. “Theory of resonant photon drag in monolayer graphene”. *Physical Review B - Condensed Matter and Materials Physics* 81.16 (2010), pp. 1–5. arXiv: `1002.0679` (cit. on p. 71).

[153] Young-mi Bahk, Gopakumar Ramakrishnan, Jongho Choi, Hyelynn Song, Geunchang Choi, Yong Hyup Kim, Kwang Jun Ahn, Dai-Sik Kim, and Paul C. M. Planken. “Plasmon Enhanced Terahertz Emission from Single Layer Graphene”. *ACS Nano* 8.9 (2014), pp. 9089–9096 (cit. on p. 71).

[154] Alexander N. Obraztsov, Dmitry A. Lyashenko, Shaoli Fang, Ray H. Baughman, Petr A. Obraztsov, Sergei V. Garnov, and Yuri P. Svirko. “Photon drag effect in carbon nanotube yarns”. *Applied Physics Letters* 94.23 (2009), p. 231112 (cit. on p. 71).

[155] Thomas Mueller, Fengnian Xia, and Phaedon Avouris. “Graphene photodetectors for high-speed optical communications”. *Nature Photonics* 4.5 (2010), pp. 297–301 (cit. on p. 71).

[156] Ernest V. Loewenstein, Donald R. Smith, and Robert L. Morgan. “Optical Constants of Far Infrared Materials 2: Crystalline Solids”. *Applied Optics* 12.2 (1973), p. 398 (cit. on p. 71).

[157] R. R. Nair, P. Blake, A. N. Grigorenko, K. S. Novoselov, T. J. Booth, T. Stauber, N. M. R. Peres, and A. K. Geim. “Fine Structure Constant Defines Visual Transparency of Graphene”. *Science* 320.5881 (2008), pp. 1308–1308. arXiv: `0803.3718v1` (cit. on p. 71).

[158] Kin Fai Mak, Matthew Y. Sfeir, Yang Wu, Chun Hung Lui, James A. Misewich, and Tony F. Heinz. “Measurement of the Optical Conductivity of Graphene”. *Physical Review Letters* 101.19 (2008), p. 196405 (cit. on p. 71).

[159] Kosuke Nagashio, Tomonori Nishimura, Koji Kita, and Akira Toriumi. “Mobility variations in mono- and multi-layer graphene films”. *Applied Physics Express* 2.2 (2009), pp. 1–4. arXiv: `0812.2107` (cit. on p. 72).

[160] H. R. Philipp and H. Ehrenreich. “Optical Properties of Semiconductors”. *Physical Review* 129.4 (1963), pp. 1550–1560 (cit. on p. 72).

[161] K.I. Bolotin, K.J. Sikes, Z. Jiang, M. Klima, G. Fudenberg, J. Hone, P. Kim, and H.L. Stormer. “Ultrahigh electron mobility in suspended graphene”. *Solid State Communications* 146.9-10 (2008), pp. 351–355 (cit. on p. 72).

[162] Agnieszka Siemion, Andrzej Siemion, Michał Makowski, Jarosław Suszek, Jarosław Bomba, Adam Czerwiński, Frédéric Garet, Jean-Louis Coutaz, and Maciej Sypek. “Diffractive paper lens for terahertz optics”. *Optics Letters* 37.20 (2012), p. 4320 (cit. on p. 75).

[163] Takumi Yatooshi, Atsushi Ishikawa, and Kenji Tsuruta. “Terahertz wavefront control by tunable metasurface made of graphene ribbons”. *Applied Physics Letters* 107.5 (2015), p. 053105 (cit. on p. 75).

[164] Hua Cao and Ajay Nahata. “Coupling of terahertz pulses onto a single metal wire waveguide using milled grooves”. *Optics Express* 13.18 (2005), p. 7028 (cit. on pp. 75, 81).

[165] Jason A. Deibel, Kanglin Wang, Matthew D. Escarra, and Daniel Mittleman. “Enhanced coupling of terahertz radiation to cylindrical wire waveguides”. *Optics Express* 14.1 (2006), p. 279 (cit. on pp. 75, 81, 82).

[166] Manoj Kumar Mridha, Anna Mazhorova, Matteo Clerici, Ibraheem Al-Naib, Maxime Daneau, Xavier Ropagnol, Marco Peccianti, Christian Reimer, Marcello Ferrera, Luca Razzari, François Vidal, and Roberto Morandotti. “Active terahertz two-wire waveguides”. *Optics Express* 22.19 (2014), p. 22340 (cit. on pp. 75, 81).

[167] M. Ibanescu. “An All-Dielectric Coaxial Waveguide”. *Science* 289.5478 (2000), pp. 415–419 (cit. on p. 76).

[168] Alexey V. Krasavin and Anatoly V. Zayats. “Guiding light at the nanoscale: numerical optimization of ultrasubwavelength metallic wire plasmonic waveguides”. *Optics Letters* 36.16 (2011), p. 3127 (cit. on p. 76).

[169] Xiewen Wen and Junrong Zheng. “Broadband THz reflective polarization rotator by multiple plasmon resonances”. *Optics Express* 22.23 (2014), p. 28292 (cit. on p. 76).

[170] B. B. Hu, J. T. Darrow, X.-C. Zhang, D. H. Auston, and P. R. Smith. “Optically steerable photoconducting antennas”. *Applied Physics Letters* 56.10 (1990), p. 886 (cit. on p. 76).

[171] M. Beck, H. Schäfer, G. Klatt, J. Demsar, S. Winnerl, M. Helm, and T. Dekorsy. “Impulsive terahertz radiation with high electric fields from an amplifier-driven large-area photoconductive antenna”. *Optics Express* 18.9 (2010), p. 9251 (cit. on pp. 76, 81).

[172] Maik Scheller, Stefan F. Dürrschmidt, Matthias Stecher, and Martin Koch. “Terahertz quasi-time-domain spectroscopy imaging”. *Applied Optics* 50.13 (2011), p. 1884 (cit. on p. 77).

[173] Thorsten Probst, Arno Rehn, and Martin Koch. “Compact and low-cost THz QTDS system”. *Optics Express* 23.17 (2015), p. 21972 (cit. on pp. 77, 87).

[174] K. Wang and D. M. Mittleman. “Metal wires for terahertz wave guiding”. *Nature* 432.November (2004) (cit. on p. 81).

[175] Kanglin Wang and Daniel M. Mittleman. “Guided propagation of terahertz pulses on metal wires”. *Journal of the Optical Society of America B* 22.9 (2005), p. 2001 (cit. on p. 81).

[176] Hamid Pahlevaninezhad, Thomas E. Darcie, and Barmak Heshmat. “Two-wire waveguide for terahertz”. *Optics Express* 18.7 (2010), p. 7415 (cit. on p. 81).

[177] Aurele Joseph Louis Adam. “Review of Near-Field Terahertz Measurement Methods and Their Applications”. *Journal of Infrared, Millimeter, and Terahertz Waves* 32.8-9 (2011), pp. 976–1019 (cit. on p. 81).

[178] Hongkyu Park, Edward P. J. Parrott, Fan Fan, Meehyun Lim, Haewook Han, Vladimir G. Chigrinov, and Emma Pickwell-MacPherson. “Evaluating liquid crystal properties for use in terahertz devices”. *Optics Express* 20.11 (2012), p. 11899 (cit. on p. 87).

[179] Yang Wu, Xuezhong Ruan, Chih-Hsin Chen, Young Jun Shin, Youngbin Lee, Jing Niu, Jingbo Liu, Yuanfu Chen, Kun-Lin Yang, Xinhai Zhang, Jong-Hyun Ahn, and Hyunsoo Yang. “Graphene/liquid crystal based terahertz phase shifters”. *Optics Express* 21.18 (2013), p. 21395. arXiv: `1309.1595` (cit. on p. 87).

[180] Lei Wang, Xiao-Wen Lin, Wei Hu, Guang-Hao Shao, Peng Chen, Lan-Ju Liang, Biao-Bing Jin, Pei-Heng Wu, Hao Qian, Yi-Nong Lu, Xiao Liang, Zhi-Gang Zheng, and Yan-Qing Lu. “Broadband tunable liquid crystal terahertz waveplates driven with porous graphene electrodes”. *Light: Science & Applications* 4.2 (2015), e253 (cit. on p. 87).

[181] Christian Jansen, Ibraheem A. I. Al-Naib, Norman Born, and Martin Koch. “Terahertz metasurfaces with high Q-factors”. *Applied Physics Letters* 98.5 (2011), p. 051109 (cit. on p. 87).

[182] Mohammad Javad Mohammad-Zamani, Mohammad Kazem Moravvej-Farshi, and Mohammad Neshat. “Unbiased continuous wave terahertz photomixer emitters with dis-similar Schottky barriers”. *Optics Express* 23.15 (2015), p. 19129 (cit. on p. 87).

[183] Matthias Wichmann, Markus Stein, Arash Rahimi-Iman, Stephan W. Koch, and Martin Koch. “Interferometric characterization of a semiconductor disk laser driven terahertz source”. *Journal of Infrared, Millimeter, and Terahertz Waves* 35.6-7 (2014), pp. 503–508 (cit. on p. 88).

[184] Maik Scheller, Justin R. Paul, Alexandre Laurain, Abram Young, Stephan W. Koch, and Jerome V. Moloney. “Terahertz generation by difference frequency conversion of two single-frequency VECSELs in an external resonance cavity”. *SPIE Photonics West 2014-LASE: Lasers and Sources* 8966 (2014), 89660E (cit. on p. 88).